

Comparing Theory and Measurements of Woodwind-Like Instrument Acoustic Radiation

Shi Yong



Music Technology Area, Department of Music Research
Schulich School of Music
McGill University
Montreal, Quebec, Canada

January 2009

A thesis submitted to McGill University in partial fulfillment of the requirements for
the degree of Master of Arts in Music Technology.

© 2009 Shi Yong

Abstract

This thesis provides a review of a computational modeling technique for woodwind-like musical instruments with arbitrarily shaped bore and finger holes. The model of a simple acoustic structure implemented in Matlab is verified through experimental measurements in terms of radiation directivity.

The methods of calculating the acoustical impedance at the input end and the internal sound pressure at any position along the principle axis of the bore are presented. The procedure for calculating the radiation pressure is detailed in an example featuring a main bore with two open holes. The far-field and near-field formulas of radiation distances and angles are given.

A modified pulse reflectometry system is used to measure the radiation directivity of the sample woodwind-like instrument. The measurement and data processing are simulated using a digital waveguide model to test the validity of the measurement system. The final measurements are performed with five fingerings for the measured object. The measurement results are compared with the theoretically predicted values to evaluate the fitness of the model. Suggestions for further improvement of both the measurement and the model are given.

Sommaire

Cette thèse propose une analyse des techniques de modélisation informatique des instruments de musique de la famille des bois à perce et trous arbitraires. Le modèle d'une structure acoustique simple implémenté avec Matlab est vérifié par des mesures expérimentales de la directivité du rayonnement.

Les méthodes de calcul de l'impédance acoustique à l'entrée ainsi que de la pression acoustique à n'importe quelle position le long de l'instrument sont présentées. La procédure de calcul de la pression de radiation est détaillée pour le cas d'un tuyau cylindrique ouvert avec deux trous latéraux. Les formules de calcul du rayonnement en champ lointain et en champ proche sont données.

Un système de mesure de la réponse impulsionnelle est utilisé pour mesurer la directivité de la radiation sur un prototype d'instrument ayant les caractéristiques de la famille des bois. La mesure et le traitement des données sont simulés en utilisant un modèle de guide d'ondes numérique pour tester la validité du système de mesure. Les mesures finales sont effectuées pour les cinq doigts de l'objet mesuré. Les résultats sont comparés aux valeurs théoriques pour évaluer la qualité du modèle. Des suggestions pour l'amélioration de la mesure et du modèle sont données.

Acknowledgments

I would like to sincerely thank my supervisor Dr. Gary Scavone for encouraging me to apply to the music technology program in McGill University; helping me to select this field of thesis study, and; for spending considerable amounts of time giving guidance, advice, and feedback for all aspects of my studies, research, experiments and thesis writing.

I am deeply indebted to Antoine Lefebvre. Without his help the measurements might never have been started, let alone finished. His invaluable advice and useful suggestions are highly appreciated.

Thank you to all of the members of the McGill Music Technology Area and particularly the members of the CAML lab for providing a wonderful environment in which to pursue my research. Thanks Mark Zadel, Andrey da Silva, Mark Marshall, Li Beinan, Moonseok Kim, Jung Suk Lee, Darryl Cameron and others for their advice and assistance throughout my graduate studies. A special thanks goes to Avrum Hollinger for kindly providing proof reading. Thank you to Dr. William Martens for graciously providing the use of the facilities and services in CIRMMT during the measurement stages of this work.

Thanks to Wang Yujuan for her great support and encouragement. Thank you to my dear buddy Pierre Demers, who helped me enjoy the life in this beautiful city Montreal, encourages me all the time and always reminds me that life is more than work.

Finally, the greatest thanks go to my parents and my sister Shi Qin in Hunan province, China, for their moral support in my most difficult times.

Contents

1	Introduction	1
1.1	Motivation	1
1.2	Outline	2
2	Wave Propagation Inside Air Column	5
2.1	Infinite Cylindrical Bore	5
2.2	Finite Cylindrical Bore	7
2.3	Conical Bore	9
2.4	Transmission Matrices	12
2.5	Thermal and Viscous Losses	15
3	Sound Radiation and Directivity	21
3.1	Radiation Impedance	21
3.2	Tonehole Model	25
3.3	Refinement of Tonehole Model	28
3.4	Radiation Model of a Main Bore with Toneholes	33
3.4.1	Bore Segment	33
3.4.2	Tonehole Segment	34
3.4.3	An Example of a Main Bore with Two Toneholes	36
3.5	Directivity	37
3.5.1	Power Gain Directivity	37
3.5.2	Pressure Directivity	39
3.5.3	Radiation Distance and Angle	41

4	Reflectometry Measurement Technique	43
4.1	History of Pulse Reflectometry Technique	44
4.2	Reflectometry Technique for Input Impedance Measurement	45
4.3	Impulse Reflectometry for Radiation Measurement	48
4.3.1	Setup	48
4.3.2	Theory	49
4.3.3	Simulation and Verification	50
5	Comparison of the Theoretical and Measurement Results	57
5.1	Measured Objects	57
5.2	Theoretical Model	58
5.3	Measurement Setup	59
5.4	Preliminary Measurements	60
5.5	Model Refinements	61
5.5.1	Outside Radius	61
5.5.2	Refined Open Hole Model	62
5.5.3	Near-field Correction	62
5.6	Final Measurements	63
6	Conclusions and Future Work	69
6.1	Conclusions	69
6.2	Future Work	70
A	Results of Final Measurements	73
A.1	Fingering H1	74
A.2	Fingering H1H3	76
A.3	Fingering H1H2H3	78
A.4	Fingering H2H3	80
A.5	Fingering H3	82

List of Symbols

α	attenuation coefficient
η	shear viscosity coefficient
Γ	complex wavenumber
κ	thermal conductivity
Ω	continuous-time frequency variable
ω	discrete-time frequency variable ($-\pi \leq \omega \leq \pi$)
ρ	density of air
ξ_e	specific resistance of open tonehole
a	bore radius
b	tonehole radius
c	speed of sound in air
C_p	specific heat of air at constant pressure
f	frequency variable
f_s	discrete-time sampling frequency
j	imaginary unit ($j = \sqrt{-1}$)
k	wavenumber ($k = \Omega/c$)
p or P	sound pressure

R	frequency-dependent reflectance
r_c	curvature radius
r_t	ratio of thermal boundary layer thickness to bore radius
r_v	ratio of viscous boundary layer thickness to bore radius
S	surface area
t	continuous time variable
t_a	equivalent length of tonehole series
t_{eh}	effective height of tonehole
t_e	effective length of open tonehole
t_i	inner length correction of tonehole
t_m	equivalent matching length of tonehole
t_r	length correction associated with radiation impedance
u or U	volume velocity within an acoustic structure
v_p	phase velocity
Y_0	characteristic acoustic admittance of main bore
Z_0	characteristic acoustic impedance of main bore
Z_a	series impedance
Z_{ch}	characteristic acoustic impedance of tonehole
Z_c	frequency-dependent complex characteristic acoustic impedance
Z_{in}	input acoustic impedance
Z_L	load impedance
Z_r	radiation impedance
Z_s	shunt impedance

List of Figures

2.1	Cylindrical polar coordinates.	6
2.2	Input impedance of a lossless cylindrical pipe model. The length is $L = 0.148$ meters, the radius is $a = 0.00775$ meters. The load impedance at the open end is approximated by Levine and Schwinger's solution.	9
2.3	Conical spherical coordinates.	10
2.4	Divergent conical frusta.	11
2.5	A bore consisting of three sections, modeled by a transmission network. .	13
2.6	Input impedance of a lossy cylindrical pipe. The length is $L = 0.148$ meters, the radius is $a = 0.00775$ meters. The load impedance at the open end is approximated by Levine and Schwinger's solution.	17
2.7	Input impedance of a lossy conical pipe. The length of the truncated cone is $L = 0.148$ meters, the radii of the input end and the output end are $a_{in} = 0.00775$ and $a_{out} = 0.009$ meters, respectively. The load impedance at the open end is approximated by Levine and Schwinger's solution. . . .	18
2.8	The input impedance of a multi-section bore. The load impedance at the open end is approximated by Levine and Schwinger's solution.	19
3.1	Geometric length vs. equivalent acoustical length.	22
3.2	Reflectance magnitude $ R $ and length correction (l/a) for flanged and unflanged circular pipes.	24
3.3	Geometry of a tonehole in the middle of a main bore.	25
3.4	T-section.	26
3.5	L-section.	28
3.6	Equivalent circuit of the basic tonehole model and the refined tonehole model.	29

3.7	A tonehole in the middle of a main pipe, the matching volume area is colored in black.	30
3.8	The Keefe tonehole model vs. the refined open hole model in (Dalmont et al., 2002).	32
3.9	The transmission line model of a cylindrical bore.	33
3.10	The transmission line model of a tonehole.	35
3.11	The transmission line model of a main bore with two toneholes.	36
3.12	Radiation sound pressure measured at angle θ and distance r from the pipe end.	37
3.13	Radiation pressure directivity factor.	39
3.14	Radiation pressure directivity factor in polar plots.	40
3.15	Calculation of radiation distances and angles.	41
3.16	Calculation of radiation distances and angles (with a reference point underneath the pipe).	42
4.1	Reflectometry setup for input impedance measurement.	45
4.2	The signals were calculated from a digital waveguide model simulating the pulse reflectometry system, where the source reflectance was approximated by a constant coefficient 1. Top: $y_1(t)$ is the recorded complicated signal of calibration. Bottom: $y_2(t)$ is the recorded complicated signal of object reflection.	46
4.3	Reflectometry setup for radiation pressure directivity measurement.	48
4.4	Digital waveguide model of the impulse reflectometry.	50
4.5	Frequency response and phase angle of the boundary layer filter $H_b(Z)$	51
4.6	Frequency response and phase angle of the reflectance filter R_L	51
4.7	Impulse reflectometry model stimulated by unit impulse signal. Top: the ideal unit impulse. Middle: the impulse response sampled at the closed end of the main pipe. Bottom: the impulse response sampled at the open end of the main pipe ($\theta = 0$).	52
4.8	Impulse response truncated by rectangular window. Top: the first pulse of the impulse response sampled at the closed end. Bottom: the first pulse of the impulse response sampled at the open end. (system stimulated by unit impulse)	53

4.9	Impulse reflectometry model stimulated by swept sine signal. Top: the swept sine signal. Middle: the response sampled at the closed end of the main pipe. Bottom: the response sampled at the open end of the main pipe ($\theta = 0$).	54
4.10	Top: the calculated impulse response series at the closed end of the main pipe. Bottom: the calculated impulse response series at the open end of the main pipe. (system stimulated by swept sine)	55
4.11	Impulse response truncated by rectangular window. Top: the first pulse of the impulse response sampled at the closed end. Bottom: the first pulse of the impulse response sampled at the open end. (system stimulated by swept sine)	55
4.12	Comparison of the radiation pressure transfer function calculated by using different stimulus: unit impulse vs. swept sine.	56
5.1	Impulse reflectometry setup for radiation directivity measurement.	58
5.2	Comparison of the measurement results using source signals of different lengths: $N = 2^{18}$ and $N = 2^{21}$. Left: fingering H1 at 0 degrees. Right: fingering H1H3 at 180 degrees.	60
5.3	Model using inside radius vs. outside radius. Left: fingering H1 at 90 degrees. Right: fingering H1H2H3 at 90 degrees.	61
5.4	Keefe tonehole model vs. Dalmont tonehole model. Left: fingering H3 at 270 degrees. Right: fingering H1H2H3 at 270 degrees.	62
5.5	Far-field model vs. near-field model. Left: fingering H1H2H3 at 270 degrees. Right: fingering H1H3 at 270 degrees.	63
5.6	Model vs. measurement. Left: fingering H1H2H3, 30 degrees. Right: fingering H1H3, 30 degrees.	64
5.7	Model vs. measurement. Left: fingering H1, 150 degrees. Right: fingering H3, 150 degrees.	65
5.8	Model vs. measurement. Left: fingering H1H2H3, 240 degrees. Right: fingering H1H3, 90 degrees.	65
5.9	Model vs. measurement. Left: fingering H2H3, 240 degrees. Right: fingering H2H3, 210 degrees.	66
6.1	The 64-channel Radiation Directivity Measurement System.	71

Chapter 1

Introduction

1.1 Motivation

This thesis focuses on the sound radiation properties of wind-blown musical instruments with finger holes, such as flutes, clarinets, oboes, and saxophones.

A woodwind instrument consists of an excitation mechanism, a resonator, and a radiating element. The sound is generated by air vibrations within an air column of roughly cylindrical or conical shape. Since the 1960s, various theories and mathematical models have been developed to describe and simulate the behavior of woodwind instruments, but many questions still remain unanswered.

The wave propagation within the air column can be analyzed by using the associated Helmholtz equation, a mathematical representation of steady-state vibrations of air, and applying appropriate boundary conditions. Open side holes will acoustically shorten the vibrating air column in the bore and, consequently, cause the resonance frequencies to increase. Closed side holes behave as compliances and lower the resonance frequencies. The tuning of a woodwind instrument can be predicted from the geometry of its bore and side holes with reasonable accuracy. Alternately, the hole positions can be calculated for specified resonance frequencies. This can be useful for designing a new instrument or improving an existing one.

At the open ends of the main bore and finger holes, sound energy propagates into the surrounding environment. It is of interest to know the transfer function between the spectrum of sound energy within the bore and the sound energy at an external pickup point.

This research aims to create a computational model of arbitrarily shaped woodwind instrument air columns to compute input impedances and external sound radiation. The measured data is compared with the results computed from mathematical models to find discrepancies. This work will help inform the quality of our current models and suggest where further correction or refinement is necessary.

1.2 Outline

Chapter 2 is a review of the theory of arbitrarily shaped air columns. The discussion starts from the idealized cylindrical and conical air column characterized by the associated Helmholtz wave propagation equation. The acoustic impedance, defined as the ratio of the sound pressure and volume velocity, is found from the solution of the wave equation by applying boundary conditions. The input impedance of the air column can then be calculated either from the load impedance at the output end or from the reflectance measured at the input end. The latter approach makes it possible to measure the input impedance of a real instrument using a measurement technique called impulse reflectometry.

Chapter 3 discusses the radiation and directivity model. The tonehole discontinuity is represented by a lumped circuit element consisting of series and shunt impedances. For greater accuracy, geometry changes and wall losses corresponding to holes are taken into account by applying various length corrections and using a complex wave number, respectively. The entire model of the main bore with toneholes is constructed by incorporating the transmission elements of toneholes into the transmission network of the main bore. The radiation impedance and the directivity factor are calculated at the output end of the open holes and the main bore using the radiation model of unflanged cylindrical pipes of Levine and Schwinger. The procedure of calculating the radiation pressure is detailed via an example of a main bore with two open holes. The far-field and near-field formulas of radiation distances and angles are given.

Chapter 4 discusses the impulse reflectometry technique. A historical review of its application for the measurement of input impedance is given. This technique is modified to suit the radiation directivity measurement. The setup, the theory and the data processing are presented. A digital waveguide simulation is performed to test the validity of the measurement technique discussed.

Chapter 5 presents object measurements using the pulse reflectometry setup. In preliminary measurements, responses corresponding to source signals of two different durations were tested. The measurement results were found to be reliable in the frequency range of about 200-7000 Hz. Discrepancies between the model and the preliminary measurement results are discussed and several model refinements were attempted. The final measurements were performed for five fingers of the measured object. The measurement results were compared with the theoretically predicted values to evaluate the fitness of the model.

Chapter 6 summarizes the theoretical model and the measurement presented in previous chapters. Suggestions for further improvements to both the measurement and the model are given.

Chapter 2

Wave Propagation Inside Air Column

The basic bore shape of almost all real woodwind instruments are fairly close to either cylinders or cones. For example, the bore of all members of the clarinet family is cylindrical. For saxophones, the bore shape is primarily conical. Therefore, our study in this chapter concentrates on the computational air column model of these two basic shapes.

The sounds radiated from woodwind instruments result from sound wave motion of the air column shaped by the bore. The wave propagation in the bore can be expressed as a sum of the excitations of numerous normal modes of the bore. Wave motion along the length of the air column is our main interest, because it is the fundamental mode of vibration in real wind instruments.

The air column model of both cylindrical and conical bores are presented in this chapter, which is the foundation for the discussion of the subsequent chapters. The information covered here is mainly based on the work of (Scavone, 1997), while a recent refinement of the conical bore model is amended.

2.1 Infinite Cylindrical Bore

The wave propagation in the air column of an infinite cylindrical bore is characterized by its associated Helmholtz equation in cylindrical polar coordinates system (r, ϕ, x) (see Fig. 2.1):

$$\frac{1}{r} \frac{\partial}{\partial r} \left(r \frac{\partial p}{\partial r} \right) + \frac{1}{r^2} \frac{\partial^2 p}{\partial \phi^2} + \frac{\partial^2 p}{\partial x^2} = \frac{1}{c^2} \frac{\partial^2 p}{\partial t^2}. \quad (2.1)$$

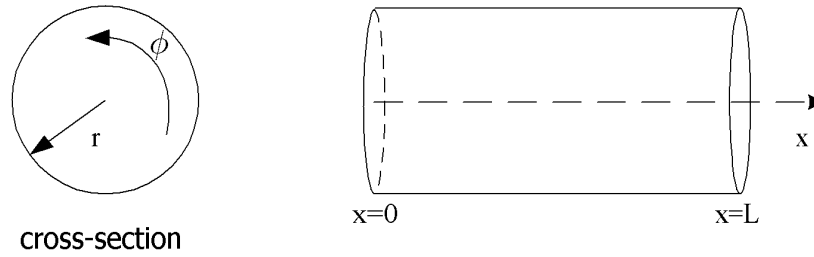


Figure 2.1 Cylindrical polar coordinates.

Here we are mainly concerned with the fundamental mode corresponding to the plane wave propagating along the longitudinal axis. In this mode, the pressure on any plane perpendicular to the principal axis x is constant. If the transverse dimension of the instrument bore is much less than the longitudinal propagation dimension, it is convenient to use transmission line theory to model the bore. For frequencies below the cut-off frequency¹, the pressure is simply a function of x and time t . The three-dimensional wave equation of Eq. (2.1) reduces to the one-dimensional plane-wave equation:

$$\frac{\partial^2 p}{\partial x^2} = \frac{1}{c^2} \frac{\partial^2 p}{\partial t^2}, \quad (2.2)$$

where p is the sound pressure and $c \approx 343\text{m/s}$ is the speed of sound.

The general solution for Eq. (2.2) for a wave component traveling in the positive x direction with sinusoidal time dependence is:

$$P(x, t) = C e^{j(\Omega t - kx)}, \quad (2.3)$$

where C is a potentially complex constant, k is the wave number defined as $k = \Omega/c$ and Ω is the continuous radian frequency.

Newton's second law for one-dimensional plane waves is expressed as:

$$\frac{\partial p}{\partial x} = -\frac{\rho}{S} \frac{\partial U}{\partial t}, \quad (2.4)$$

where $\rho = 1.21\text{kgm}^{-3}$ is the equilibrium density of air, S is the cross-sectional area of the pipe and U is the volume velocity (in m^3/sec).

¹which is given by $f = \frac{1.84c}{2\pi a}$, where a is the radius of the cylindrical bore.

Then from (2.3) and (2.4), the volume velocity is found to be:

$$U(x, t) = \left(\frac{S}{\rho c}\right) C e^{j(\Omega t - kx)}. \quad (2.5)$$

The characteristic acoustic impedance of the infinite cylindrical pipe is defined as the ratio of pressure and volume velocity:

$$Z_0(x) = \frac{P(x)}{U(x)} = \frac{\rho c}{S}. \quad (2.6)$$

From a similar analysis, the wave impedance for a wave component traveling in the negative x direction is given by $-Z_0$.

2.2 Finite Cylindrical Bore

The pipe lengths of real musical instruments are of course not infinite. When a plane wave component propagating in the right-going direction along the principle axis of a pipe encounters a discontinuity, such as an open pipe termination, part of the wave component is reflected back as a left-going traveling wave, and part is transmitted through the discontinuity as a right-going traveling wave.

The sinusoidal pressure in the pipe at position x is the superposition of the pressure contributed by left- and right-going traveling waves and has the form:

$$P(x, t) = [Ae^{-jkx} + Be^{jkx}]e^{j\Omega t}, \quad (2.7)$$

where A and B are the complex amplitudes of left- and right-going traveling waves, respectively.

Similarly, the volume flow can be calculated from (2.7) and (2.4) as:

$$U(x, t) = \left(\frac{1}{Z_0}\right) [Ae^{-jkx} - Be^{jkx}]e^{j\Omega t}, \quad (2.8)$$

where $Z_0 = \frac{\rho c}{S}$ is the characteristic acoustic impedance.

For a cylindrical pipe of length L terminated at $x = L$ by the load impedance Z_L , the ratio of complex amplitudes B/A , which is referred to as the pressure wave reflectance,

is given as:

$$\frac{B}{A} = e^{-2jkL} \left[\frac{Z_L - Z_0}{Z_L + Z_0} \right]. \quad (2.9)$$

The power reflectance is defined as the ratio of reflected power to incident power:

$$\left| \frac{B}{A} \right|^2 = \left| \frac{Z_L - Z_0}{Z_L + Z_0} \right|^2. \quad (2.10)$$

For the infinite cylindrical pipe, the load impedance is the same as the characteristic impedance, so there is no reflection and then $Z_L = Z_0$. For the cylindrical pipe of finite length, the reflectance depends on the termination condition of the pipe end. In the low frequency approximation, where $Z_L = 0$ for an open end and $Z_L = \infty$ for a rigidly closed end, traveling-wave components experience complete reflection (with and without a 180 degrees phase change).

A very useful quantity is called the input impedance Z_{in} , which is frequency dependent, defined as the ratio of pressure to volume flow at the input end ($x = 0$) of the pipe:

$$Z_{in} = \frac{P(0, t)}{U(0, t)} = Z_0 \left[\frac{Z_L \cos(kL) + jZ_0 \sin(kL)}{jZ_L \sin(kL) + Z_0 \cos(kL)} \right]. \quad (2.11)$$

If we note the wave pressure reflectance at the input end of the bore as $R = B/A$, then the input impedance Z_{in} of a finite cylindrical bore can also be calculated from R :

$$Z_{in} = Z_0 \left(\frac{1 + R}{1 - R} \right). \quad (2.12)$$

The relation between Z_{in} and the reflectance R is very useful. As we will see in Chpt. 4, the reflectance at the input end of a finite cylindrical waveguide can be measured by a technique referred to as *impulse reflectometry*. Thus, from this measurement we are also able to calculate the input impedance of an acoustic structure.

The input impedance provides very useful information about the acoustic behavior of an instrument in the frequency domain. For woodwind-like instruments, it gives the sound pressure amplitude at the input end that results from an injected sinusoidal volume velocity excitation signal. The intonation and response can be inferred from the input impedance. For example, sharper and stronger peaks indicate frequencies that are easiest to play.

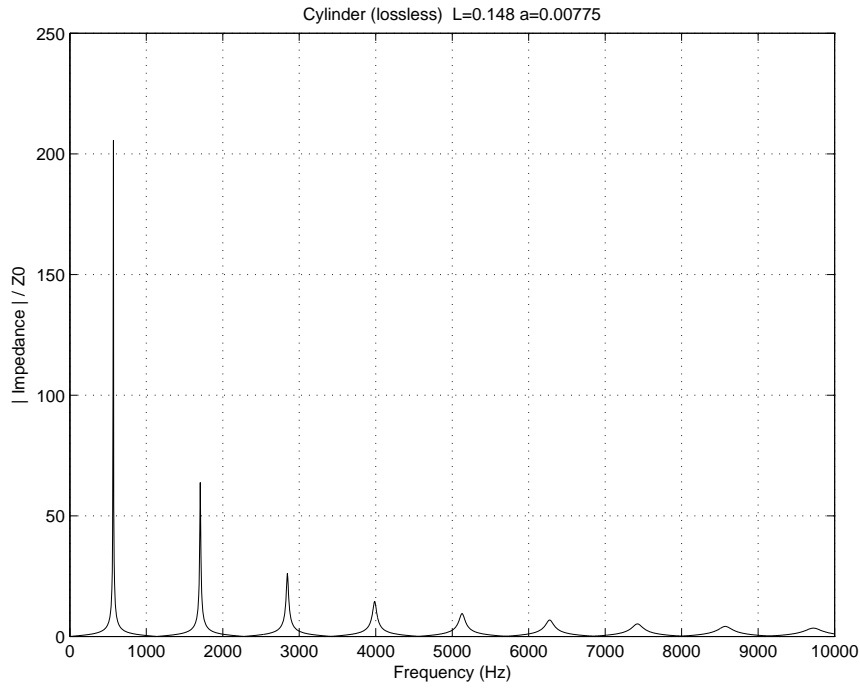


Figure 2.2 Input impedance of a lossless cylindrical pipe model. The length is $L = 0.148$ meters, the radius is $a = 0.00775$ meters. The load impedance at the open end is approximated by Levine and Schwinger's solution.

The theoretical input impedance of a lossless cylindrical pipe of length $L = 0.148$ meters and radius $a = 0.00775$ meters is illustrated in Fig. 2.2. Note the theoretical result is only valid for frequencies below the cut-off frequency 12.83 kHz. The load impedance at the open end is approximated by Levine and Schwinger's solution discussed in Sec. 3.1.

2.3 Conical Bore

The spherical wave propagation in the air column of an infinite conical bore can be characterized by its associated Helmholtz equation in spherical coordinates system (x, ϕ, θ) (see Fig. 2.3):

$$\frac{1}{x^2} \frac{\partial}{\partial x} \left(x^2 \frac{\partial p}{\partial x} \right) + \frac{1}{x^2 \sin \theta} \frac{\partial}{\partial \theta} \left(\sin \theta \frac{\partial p}{\partial \theta} \right) + \frac{1}{x^2 \sin^2 \theta} \frac{\partial^2 p}{\partial \phi^2} = \frac{1}{c^2} \frac{\partial^2 p}{\partial t^2}. \quad (2.13)$$

For the same reason mentioned previously, here we are only interested in the wave

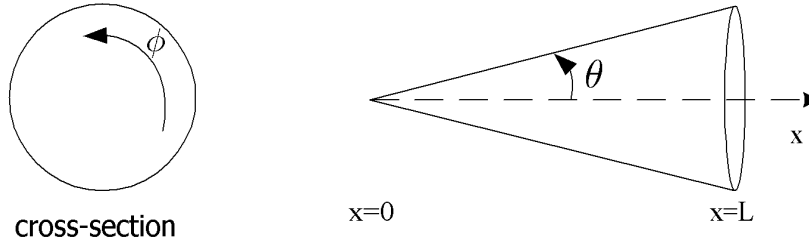


Figure 2.3 Conical spherical coordinates.

propagation along the longitudinal axis. The corresponding one-dimensional wave equation is separated from the three-dimensional Helmholtz equation as:

$$\frac{d^2(xX)}{dx^2} + \left(k^2 - \frac{\beta^2}{x^2}\right)(xX) = 0, \quad (2.14)$$

where β is the separation constant and X has the form:

$$X(x) = (kx)^{-\frac{1}{2}} J_{n+\frac{1}{2}}(kx),$$

where $J_{n+\frac{1}{2}}(kx)$ is a Bessel function.

The corresponding general solution for a wave component traveling in the positive x direction with sinusoidal time dependence is:

$$P(x) = \frac{C}{x} e^{-jkx}, \quad (2.15)$$

where C is a potentially complex constant and k is the wave number.

The length of the conical bore of any real musical instrument is always finite. Therefore, as in the case of the finite cylindrical pipe model, the effect of discontinuity at the end of a finite conical tube can be expressed in terms of superposed left- and right-going traveling-waves. The sinusoidal pressure in the conical pipe at position x has the form:

$$P(x, t) = \left[\frac{A}{x} e^{-jkx} + \frac{B}{x} e^{jkx} \right] e^{j\Omega t}. \quad (2.16)$$

Newton's second law for one-dimensional spherical waves is expressed in terms of

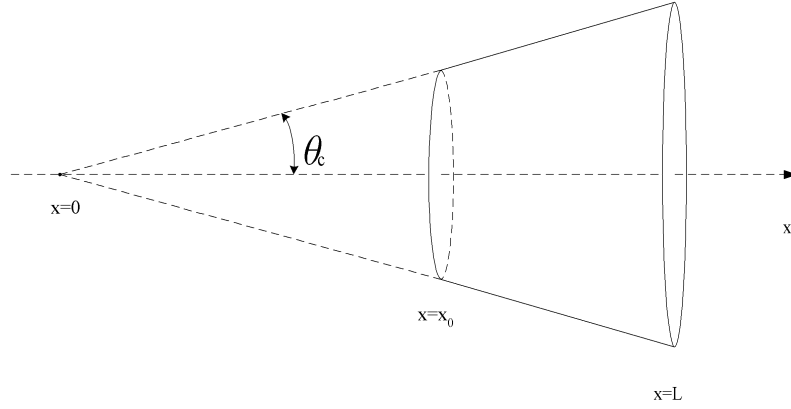


Figure 2.4 Divergent conical frusta.

volume flow velocity as:

$$\frac{\partial p}{\partial x} = -\frac{\rho}{S(x)} \frac{\partial U}{\partial t}, \quad (2.17)$$

where $S(x)$ is the surface area of a spherical wavefront in the conical bore at position x and ρ is the density of air.

The volume velocity is then found from Eq. (2.16) and Eq. (2.17) as:

$$U(x, t) = \frac{1}{x} \left[\frac{A}{Z_0(x)} e^{-jkx} - \frac{B}{Z_0^*(x)} e^{jkx} \right] e^{j\Omega t}, \quad (2.18)$$

where $Z_0(x)$ is the characteristic acoustic impedance for the positive x-direction spherical traveling-wave:

$$Z_0(x) = \frac{1}{\frac{S(x)}{\rho c} + \frac{S(x)}{j\Omega \rho x}}. \quad (2.19)$$

The characteristic acoustic impedance for the negative x-direction spherical traveling-wave is noted as $Z_0^*(x)$, which is the complex conjugate of $Z_0(x)$.

For a divergent conical frustum truncated at $x = x_0$ and with an open end at $x = L$, as illustrated in Fig. 2.4, the spherical pressure wave reflectance in the frequency domain is given by:

$$\frac{B}{A} = e^{-2jkL} \left[\frac{Z_L Z_0^*(L) - Z_0(L) Z_0^*(L)}{Z_L Z_0(L) + Z_0(L) Z_0^*(L)} \right], \quad (2.20)$$

where Z_L is the load impedance at the end ($x = L$).

The input admittance $Y_{in}(x)$ ² of a truncated conical bore is related to the reflectance:

$$Y_{in}(x) = \frac{S(x)}{\rho c} \left\{ \left[\frac{e^{-jkx} - \frac{B}{A}e^{jkx}}{e^{-jkx} + \frac{B}{A}e^{jkx}} \right] + \frac{1}{jkx} \right\}, \quad (2.21)$$

where x is the position from where the input admittance is seen. A positive or negative value of x indicates a divergent or convergent conical section, respectively.

For a truncated cone extending from the small end ($x = x_0$) to the open mouth ($x = L$), we assume that at low frequencies the load impedance is approximated by $Z_L = 0$. Thus, the input admittance reduces to:

$$Y_{IN}(x_0) = \frac{S(L)}{j\rho c} \left[\cot(kl) - \frac{1}{kx_0} \right], \quad (2.22)$$

where $l = L - x_0$ is the length of the truncated cone.

Similarly, as in the case of a finite cylindrical bore, the input impedance Z_{in} of a divergent conical tube can be completely defined by the wave pressure reflectance at the input end $R = B/A$:

$$Z_{in} = Z_0 \left[\frac{Z_0 Z_0^* (1 + R)}{Z_0^* - Z_0 R} \right]. \quad (2.23)$$

This allows for the measurement of the input impedance of the conical bore of a real instrument.

2.4 Transmission Matrices

Thus far we have discussed the method of calculating the input impedance of ideal cylindrical or conical bores from the load impedance. However, real woodwind instruments are not idealized geometries. For an arbitrarily shaped acoustic pipe structure, it is possible to use cascaded cylindrical and conical sections to approximate the bore. Each section can be modeled by a two-port network of sound pressure p and volume flow U at both the input and output. The entire bore is modeled by a transmission network.

²For conical bore, the input admittance Y_{in} is expressed more simply than the input impedance Z_{in} , where $Y_{in} = \frac{1}{Z_{in}}$.

A simple example is illustrated in Fig. 2.5, where an arbitrary bore is approximated by cascaded cylindrical and conical sections.

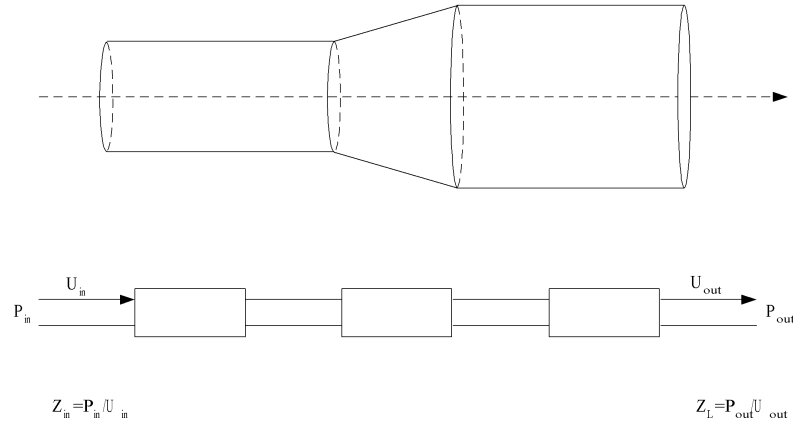


Figure 2.5 A bore consisting of three sections, modeled by a transmission network.

The input impedance of the entire instrument bore can be obtained by using the method described below. Given the load impedance Z_L at the output end of the bore, the input impedance of the last section can be calculated by using Eq. (2.11) for cylindrical sections or (2.22) for truncated cone sections. The input impedance of the last section is the load impedance of the adjacent second-last section. The input impedance of the second-last section is calculated in the same way. This computation is iterated until the input impedance of the entire bore is obtained.

For each individual cylindrical or divergent conical section (input at the small end), the pressure P_1 and volume velocity U_1 at the input end and P_2 and U_2 at the output end are related by the associated transmission matrix, as:

$$\begin{bmatrix} P_1 \\ U_1 \end{bmatrix} = \begin{bmatrix} A & B \\ C & D \end{bmatrix} \begin{bmatrix} P_2 \\ U_2 \end{bmatrix}. \quad (2.24)$$

For a convergent conical section (input at the big end), the inverse conjugate matrix of (2.24) is used:

$$\begin{bmatrix} P_1 \\ U_1 \end{bmatrix} = \begin{bmatrix} D & B \\ C & A \end{bmatrix} \begin{bmatrix} P_2 \\ U_2 \end{bmatrix}. \quad (2.25)$$

The transmission-matrix coefficients for a lossless cylindrical section are given by:

$$\begin{cases} A = \cos(kL) \\ B = jZ_0 \sin(kL) \\ C = \frac{j}{Z_0} \sin(kL) \\ D = \cos(kL), \end{cases} \quad (2.26)$$

where L is the length.

The transmission-matrix coefficients for a lossless truncated conical section are given by:

$$\begin{cases} A = \frac{\rho c}{S(x_0)R_L} \left[\frac{x_0}{L} \cos(kl) - \frac{x_0}{kL^2} \sin(kl) \right] \\ B = \frac{x_0}{L} jZ_0 \sin(kl) \\ C = \frac{j}{R_L} \left\{ \left[\frac{x_0}{L} + \left(\frac{1}{kL} \right)^2 \right] \sin(kl) - \frac{l}{kL^2} \cos(kl) \right\} \\ D = \frac{x_0}{L} \left[\cos(kl) + \frac{1}{kx_0} \sin(kl) \right], \end{cases} \quad (2.27)$$

where $S(x_0) = 2\pi x_0^2(1 - \cos\theta)$ is the surface area of the spherical wavefront at the input end ($x = x_0$), $l = L - x_0$ is the length of the frustum and θ is the half angle of the frustum.

The input impedance of an individual bore section can then be calculated from the load impedance and the associated transmission-matrix coefficients by:

$$Z_{in} = \frac{B + AZ_L}{D + CZ_L}. \quad (2.28)$$

For a transmission network consisting of n sections, we first calculate the transmission matrix of each section, noted as:

$$\begin{bmatrix} A_i & B_i \\ C_i & D_i \end{bmatrix}.$$

The input impedance of the entire system is then obtained by:

$$\mathbf{Z}_{in} = \frac{\mathbf{B} + \mathbf{A}Z_L}{\mathbf{D} + \mathbf{C}Z_L}, \quad (2.29)$$

where

$$\begin{bmatrix} \mathbf{A} & \mathbf{B} \\ \mathbf{C} & \mathbf{D} \end{bmatrix} = \prod_{i=1}^n \begin{bmatrix} A_i & B_i \\ C_i & D_i \end{bmatrix}.$$

2.5 Thermal and Viscous Losses

The air column model discussed thus far is based on the assumption of a lossless pipe. In real cases, the wave propagation is influenced by viscous drag and thermal exchange effects, which are measured by the thickness of the viscous boundary layer and the thermal boundary layer. Practically, the ratio of the boundary layer thickness to the bore radius is more convenient to use, which is given by (Keefe, 1984):

$$\begin{aligned} r_v &= a(\rho\Omega/\eta)^{1/2} \\ r_t &= \nu r_v \end{aligned}, \quad (2.30)$$

where a is the bore radius in meters, ρ is the density of air, η is the shear viscosity coefficient, $\nu = (\eta C_p / \kappa)^{1/2}$ is the square root of the Prandtl number, C_p is the specific heat of air at constant pressure and κ is the thermal conductivity.

The wall losses causes attenuation and phase delay to the wave propagation inside the bore. Consequently, the characteristic impedance Z_0 becomes a frequency-dependent complex quantity Z_c , and the wave number k becomes a complex quantity as well: $\Gamma = \alpha + j(\Omega/v_p)$, where the real part α is an attenuation coefficient per unit length and the imaginary part v_p is the phase velocity.

Based on the isothermal tube wall assumption, Z_c and Γ are approximated for both small- r (i.e. small r_v or r_t) and large- r (Keefe, 1984), but the results are rather complex. Practically, in the case of air at 300 K and $r_v > 2$, the following simplified results can be used in engineering applications:

$$\Re(Z_c) = Z_0(1 + 0.369r_v^{-1}) \quad (2.31)$$

$$-\Im(Z_c) = Z_0(0.369r_v^{-1} + 1.149r_v^{-2} + 0.303r_v^{-3}) \quad (2.32)$$

$$\alpha = (\Omega/c)(1.045r_v^{-1} + 1.080r_v^{-2} + 0.750r_v^{-3}) \quad (2.33)$$

$$v_p^{-1} = c^{-1}(1 + 1.045r_v^{-1}). \quad (2.34)$$

The transmission-matrix coefficients for lossy waveguide bore models are then ob-

tained by replacing the wave number k and characteristic acoustic impedance Z_0 in Eq. (2.26) and (2.27) with the complex counterparts Γ and Z_c , as given in the following:

- Transmission-matrix coefficients for lossy cylindrical bore:

$$\begin{cases} A = \cosh(\Gamma L) \\ B = Z_c \sinh(\Gamma L) \\ C = \frac{1}{Z_c} \sinh(\Gamma L) \\ D = \cosh(\Gamma L). \end{cases} \quad (2.35)$$

- Transmission-matrix coefficients for lossy conical bore:

$$\begin{cases} A = \left(\frac{L}{x_0}\right) \left[\cosh(\Gamma l) - \left(\frac{1}{\Gamma L}\right) \sinh(\Gamma l) \right] \\ B = \left(\frac{x_0}{L}\right) Z_c \sinh(\Gamma l) \\ C = \left(\frac{1}{Z_c}\right) \left\{ \left[\left(\frac{L}{x_0}\right) - \left(\frac{1}{\Gamma x_0}\right)^2 \right] \sinh(\Gamma l) + \left(\frac{l}{\Gamma x_0^2}\right) \cosh(\Gamma l) \right\} \\ D = \left(\frac{x_0}{L}\right) \left[\cosh(\Gamma l) + \left(\frac{1}{\Gamma x_0}\right) \sinh(\Gamma l) \right]. \end{cases} \quad (2.36)$$

The input impedance of the same cylindrical bore illustrated in Fig. 2.2 is recalculated by using the lossy transmission matrix given in Eq. (2.35), as shown in Fig. 2.6. The input impedance of a conical pipe is calculated using both the lossless transmission matrix given in Eq. (2.27) and the lossy transmission matrix given in Eq. (2.36), as illustrated in Fig. 2.7.

The input impedance of an arbitrarily shaped bore approximated by a 5-section transmission network is illustrated in Fig. 2.8. The first and last sections are cylinders, while the other 3 sections are truncated cones. The dimensions are defined by two vectors:

- The lengths vector of the segments is $L = [0.2 \ 0.2 \ 0.5 \ 0.3 \ 0.4 \ 0.2]$ meters.
- The radii vector of the segments is $a = [0.02 \ 0.02 \ 0.03 \ 0.02 \ 0.03 \ 0.03]$ meters.

Note that Eq. (2.36) for conical transmission-matrix coefficients is based on several approximations:

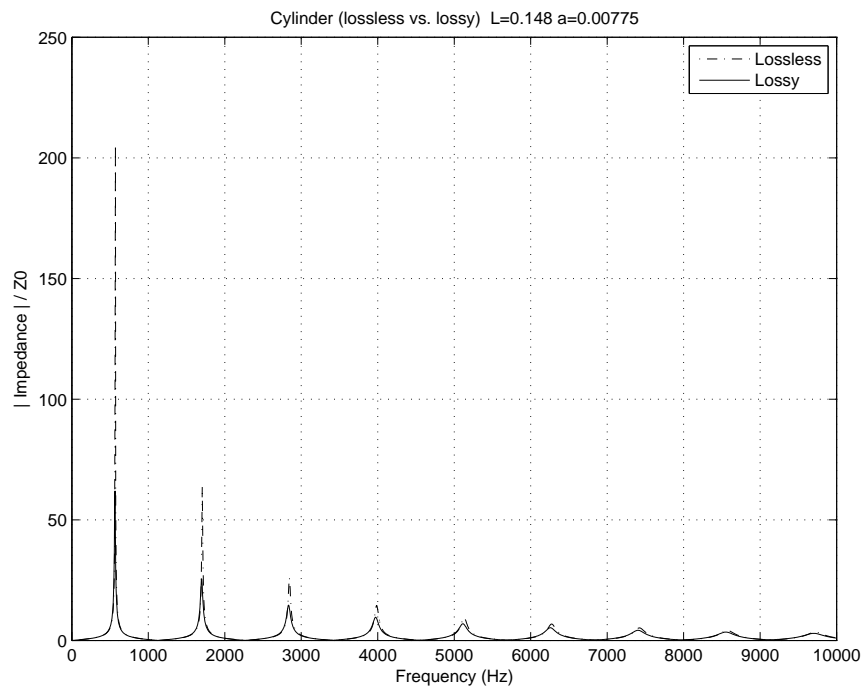


Figure 2.6 Input impedance of a lossy cylindrical pipe. The length is $L = 0.148$ meters, the radius is $a = 0.00775$ meters. The load impedance at the open end is approximated by Levine and Schwinger's solution.

- The spherical wavefronts in conical sections are approximated by plane wavefronts.
- The term r_v that determines the complex wave number is defined by a “mean” conical section radius (essentially, the conical section losses are approximated as in a cylindrical section).
- The characteristic impedance is calculated using the cross-sectional area at the input end.

Since the thermal and viscous wall losses are influenced by the bore radius, in other words the losses increase as the radius decreases in a convergent conical section, the wave number k is in fact a function of the bore radius. Therefore, k should be calculated explicitly, rather than being approximated by the “average” value of the radii of both ends. Taking this fact into account, Kulik (2007) presents an analytical solution to increase the accuracy of the conical section model. The refined transmission matrix coefficients associated with the truncated conical bore (see Fig. 2.4) are given by:

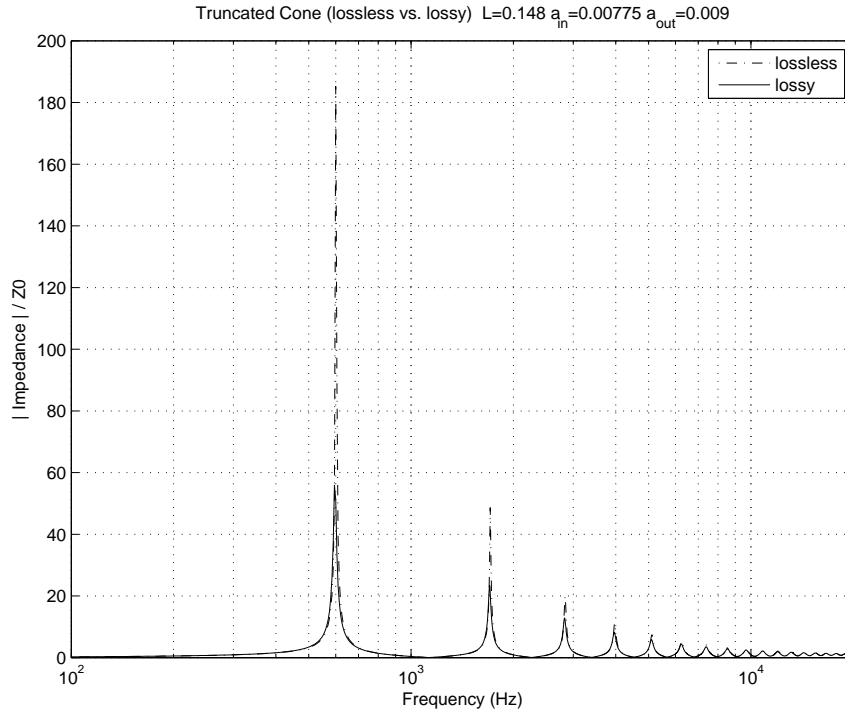


Figure 2.7 Input impedance of a lossy conical pipe. The length of the truncated cone is $L = 0.148$ meters, the radii of the input end and the output end are $a_{in} = 0.00775$ and $a_{out} = 0.009$ meters, respectively. The load impedance at the open end is approximated by Levine and Schwinger's solution.

$$\begin{bmatrix} A & B \\ C & D \end{bmatrix} = \frac{L}{x_0} \begin{pmatrix} -t_{out} \sin(\bar{k}l - \theta_{out}) & i \sin(\bar{k}l) \\ it_{in}t_{out} \sin(\bar{k}l + \theta_{in} - \theta_{out}) & t_{in} \sin(\bar{k}l + \theta_{in}) \end{pmatrix}, \quad (2.37)$$

where $l = L - x_0$ is the length of the finite conical waveguide and \bar{k} is the effective wave number of the finite conical waveguide. The $\bar{k}l$ term is given by:

$$\bar{k}l = \int_{x_0}^L k(x) dx = \frac{2\pi f}{c} \left\{ l + \frac{\delta}{\tan(\theta_c) f^{1/2}} \ln \left(\frac{L - \frac{\delta}{\tan(\theta_c) f^{1/2}}}{x_0 - \frac{\delta}{\tan(\theta_c) f^{1/2}}} \right) \right\} - i \frac{\varepsilon f^{1/2}}{\tan(\theta_c)} \ln \left(\frac{L}{x_0} \right), \quad (2.38)$$

where f is frequency in Hz, θ_c is the half angle of the cone, $\delta = 1.65 \times 10^{-3} mHz^{1/2}$ and $\varepsilon = 3 \times 10^{-5} s^{1/2}$. The parameters characterizing the two ends of the conical section are

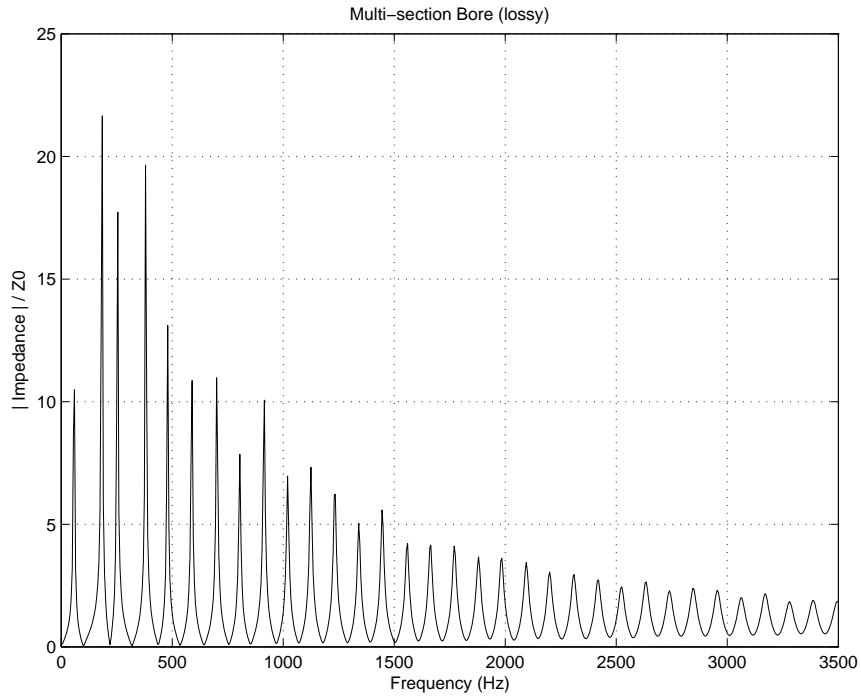


Figure 2.8 The input impedance of a multi-section bore. The load impedance at the open end is approximated by Levine and Schwinger's solution.

defined as:

$$\begin{cases} t_{in} &= 1/\sin(\theta_{in}) \\ t_{out} &= 1/\sin(\theta_{out}) \\ \theta_{in} &= \arctan(k_{in}x_0) \\ \theta_{out} &= \arctan(k_{out}L), \end{cases} \quad (2.39)$$

The k_{in} and k_{out} terms are calculated by the expression of the wave number k , which is a function of frequency and position in x-axis:

$$k(x, f) = \frac{2\pi f}{c} \left(1 + \frac{\lambda}{x - \lambda} \right) - i \frac{\varepsilon f^{1/2}}{\tan(\theta_c)} \frac{1}{x}, \quad (2.40)$$

where $\lambda = \delta / \tan(\theta_c) f^{1/2}$.

Chapter 3

Sound Radiation and Directivity

3.1 Radiation Impedance

In previous discussions, the load impedance Z_L for the open end of a cylindrical pipe was simply approximated by zero. In this section, we discuss how to obtain a more precise radiation impedance at the open end of either flanged or unflanged pipe.

The radiation impedance $Z_r(\Omega)$ cannot be measured directly. It is related to the input impedance $Z_{in}(\Omega)$ for a pipe of length L , according to (Dalmont, 2001):

$$Z_{in}(\Omega) = jZ_c(\Omega) \tan \left[kL + \arctan \left(\frac{Z_r(\Omega)}{jZ_c(\Omega)} \right) \right]. \quad (3.1)$$

where $Z_c(\Omega)$ is the characteristic acoustic impedance and k is the wave number.

Since $Z_{in}(\Omega)$ is measurable, $Z_r(\Omega)$ can be deduced from $Z_{in}(\Omega)$ by re-writing Eq. (3.1) as:

$$Z_r(\Omega) = jZ_c(\Omega) \tan \left[\arctan \left(\frac{Z_{in}(\Omega)}{jZ_c(\Omega)} \right) - kL \right]. \quad (3.2)$$

Due to the sound radiation at the output end, the resonance frequencies of the cylindrical pipe are lowered, as if the pipe is lengthened by a certain amount (refer to Fig. 3.1), or the length correction $l(\Omega)$. This can be explained by re-writing Eq. (3.1) as:

$$Z_{in}(\Omega) = jZ_c(\Omega) \tan \{k[L + l(\Omega)]\}, \quad (3.3)$$

where the term $l(\Omega) = k^{-1} \arctan \left(\frac{Z_r(\Omega)}{jZ_c(\Omega)} \right)$ is defined as the length correction and $L + l(\Omega)$

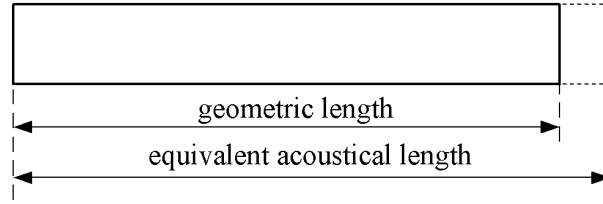


Figure 3.1 Geometric length vs. equivalent acoustical length.

is the equivalent acoustical length of the tube, as shown in Fig. 3.1. The length correction $l(\Omega)$ is complex and frequency-dependent, but for convenience it will be simply noted as l .

In real cases, the output end of a woodwind instrument is open and the sound wave propagating to the output end will be partly transmitted into the external space and partly reflected back into the bore. This phenomenon is characterized by the reflectance at the output end of the pipe, which is defined as the ratio of the reflected wave pressure p^- to the incident wave pressure p^+ measured at the output end ($x = L$):

$$R(\Omega) \triangleq \frac{p^-(L)}{p^+(L)}. \quad (3.4)$$

The radiation impedance is related to the reflectance at the output end as:

$$Z_r(\Omega) = Z_c(\Omega) \left(\frac{1 + R(\Omega)}{1 - R(\Omega)} \right), \quad (3.5)$$

Note both the radiation impedance $Z_r(\Omega)$ and the reflectance $R(\Omega)$ are complex and frequency-dependent, but for convenience they will be simply noted as Z_r and R .

The reflectance can be calculated by:

$$R = -|R|e^{-2jkl}, \quad (3.6)$$

where $|R|$ is the modulus, k is the wave number and l is the length correction. Methods of approximating $|R|$ for the open end of both flanged and unflanged pipes are discussed later.

The radiation impedance Z_r at the end of a pipe with an infinite flange is relatively easy to calculate. The following theoretical results for an open pipe of radius a set in an

infinite plane baffle were obtained by Rayleigh and Strutt (1896) and Olson (1957) and cited by Fletcher and Rossing (1991), as the following:

$$Z_r = A + jB, \quad (3.7)$$

where the acoustic resistance A and acoustic reactance B in terms of dimensionless quantity ka are given by:

$$A = Z_0 \left[\frac{(ka)^2}{2} - \frac{(ka)^4}{2^2 \cdot 3} + \frac{(ka)^6}{2^2 \cdot 3^2 \cdot 4} - \dots \right] \quad (3.8)$$

and

$$B = \frac{Z_0}{\pi k^2 a^2} \left[\frac{(2ka)^3}{3} - \frac{(2ka)^5}{3^2 \cdot 5} + \frac{(2ka)^7}{3^2 \cdot 5^2 \cdot 7} - \dots \right]. \quad (3.9)$$

Alternatively, the radiation impedance Z_r of a flanged pipe can be calculated from the reflectance R by Eq. (3.5). A rational function to approximate the modulus $|R|$ and length correction l of flanged pipe over the frequency range ($0 < ka < 3.8$) is given by Norris and Sheng (1989) as:

$$|R| = \frac{1 + 0.323ka - 0.077(ka)^2}{1 + 0.323ka + 0.923(ka)^2} \quad (3.10)$$

and

$$l/a = \frac{0.82159 - 0.49(ka)^2}{1 - 0.46(ka)^3}, \quad (3.11)$$

respectively.

For the case of an unflanged pipe (pipe with zero thickness), an analytical sound radiation model was given by Levine and Schwinger (1948), which was obtained from the solution of an integral equation based on the Wiener-Hopf technique. This model was used by Ando (1968, 1969) in the case of a tube with a finite wall thickness. The following equations are the results that are given by Levine and Schwinger (1948) and corrected by Ando (1968).

The modulus of the reflectance at the open end is given by:

$$|R| = \exp \left\{ -\frac{2ka}{\pi} \int_0^{ka} \frac{\tan^{-1}(-J_1(x)/N_1(x))}{x[(ka)^2 - x^2]^{0.5}} dx \right\}. \quad (3.12)$$

The length correction l is given by:

$$l/a = \frac{1}{\pi} \int_0^{ka} \frac{\log \pi J_1(x) [(J_1(x))^2 + (N_1(x))^2]^{1/2}}{x[(ka)^2 - x^2]^{1/2}} dx + \frac{1}{\pi} \int_0^{\infty} \frac{\log[1/(2I_1(x)K_1(x))]}{x[x^2 + (ka)^2]^{1/2}} dx. \quad (3.13)$$

Practically, the modulus $|R|$ and length correction l of unflanged pipe can be approximated by simple rational functions over the frequency range ($0 < ka < 3.8$) (Norris and Sheng, 1989):

$$|R| = \frac{1 + 0.2ka - 0.084(ka)^2}{1 + 0.2ka + 0.416(ka)^2} \quad (3.14)$$

and

$$l/a = \frac{0.6133 + 0.027(ka)^2}{1 + 0.19(ka)^2}. \quad (3.15)$$

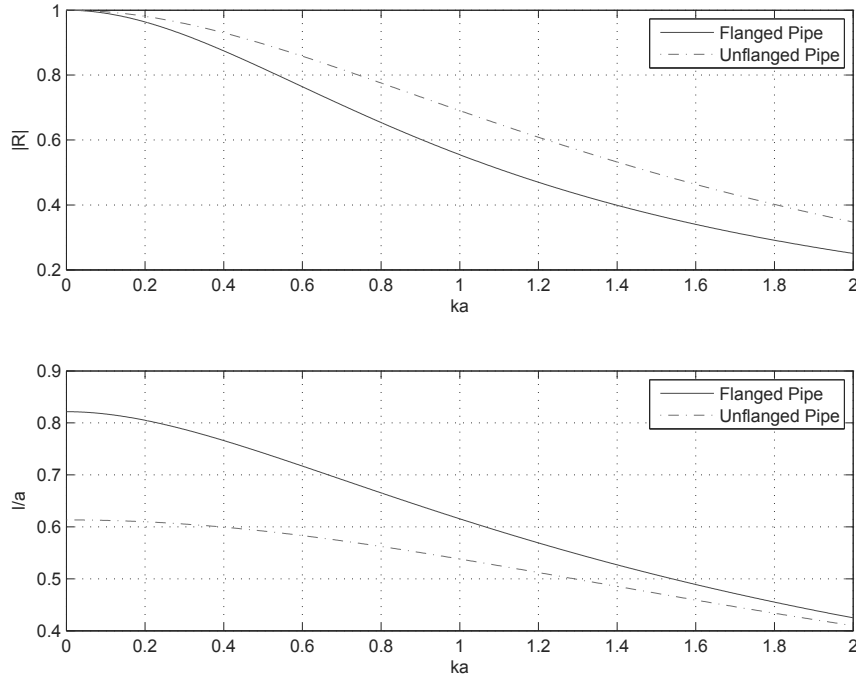


Figure 3.2 Reflectance magnitude $|R|$ and length correction (l/a) for flanged and unflanged circular pipes.

The reflectance and length correction for both flanged and unflanged pipes are calculated by using the method given by Norris and Sheng (1989) and illustrated in Fig. 3.2.

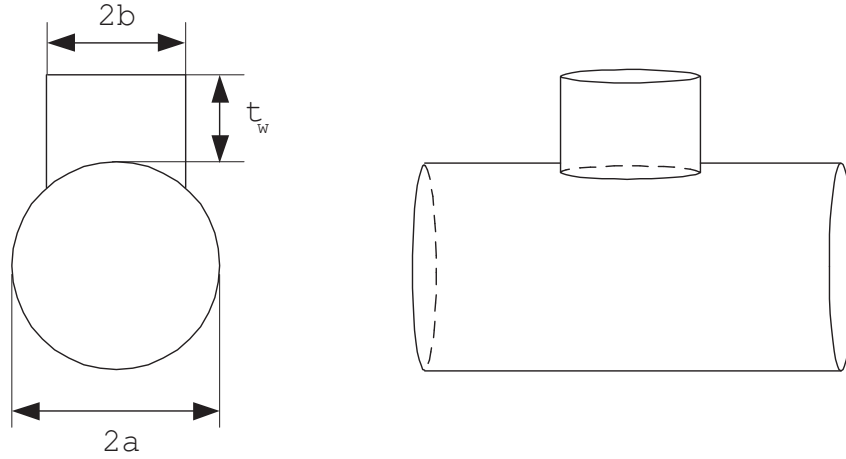


Figure 3.3 Geometry of a tonehole in the middle of a main bore.

3.2 Tonehole Model

The role of toneholes in woodwind instruments is not only to change the effective length of the main bore and consequently change the resonance frequencies, but also to allow for sound radiation. The fundamental tonehole theory is based on the work of Keefe (1981). A single tonehole modeled by a T-section transmission-line element can be incorporated into the transmission network of the main bore. A series of toneholes can be modeled in the same way and be linearly superposed.

The geometry of a single tonehole is shown in Fig. 3.3. In Keefe's theory, a single tonehole is modeled by a symmetric T-section, as shown in Fig. 3.4. The terms Z_a and Z_s are series and shunt impedances, respectively. The input/output wave pressure and volume velocity of the T-section are related by the tonehole transmission matrix TM_{th} :

$$\text{TM}_{th} = \begin{bmatrix} 1 & Z_a/2 \\ 0 & 1 \end{bmatrix} \begin{bmatrix} 1 & 0 \\ Z_s^{-1} & 1 \end{bmatrix} \begin{bmatrix} 1 & Z_a/2 \\ 0 & 1 \end{bmatrix} = \begin{bmatrix} 1 + \frac{Z_a}{2Z_s} & Z_a \left(1 + \frac{Z_a}{4Z_s} \right) \\ Z_s^{-1} & 1 + \frac{Z_a}{2Z_s} \end{bmatrix}. \quad (3.16)$$

The series and shunt impedances Z_a and Z_s corresponding to open (o) and close (c)

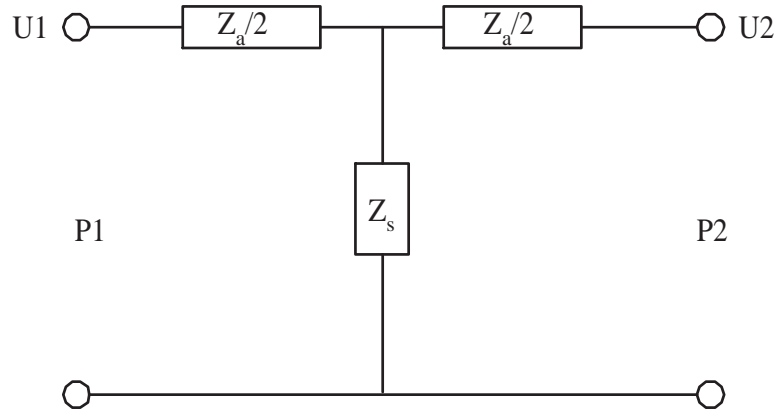


Figure 3.4 T-section.

cylindrical toneholes are given by Keefe (1990) as:

$$\begin{cases} Z_s^{(o)} = Z_0(a/b)^2(jkt_e + \xi_e) \\ Z_s^{(c)} = -jZ_0(a/b)^2 \cot(kt_{eh}) \\ Z_a^{(o)} = -jZ_0(a/b)^2 kt_a^{(o)} \\ Z_a^{(c)} = -jZ_0(a/b)^2 kt_a^{(c)}, \end{cases} \quad (3.17)$$

where $Z_0 = \rho c / \pi a^2$ is the characteristic impedance of the main bore, $k = \Omega / c$ is the wave number, a is the bore radius, b is the tonehole radius, t_{eh} is the effective height of tonehole, t_e is the effective length of open tonehole, ξ_e is the specific resistance of the open tonehole and t_a is the open and closed tonehole series equivalent lengths.

The effective height t_{eh} is defined by:

$$t_{eh} = V_h / (\pi b^2), \quad (3.18)$$

where V_h is the geometric volume of the tonehole.

Since t_{eh} cannot be measured directly, it is approximated by the easily measured wall thickness t_w (refer to Fig. 3.3) as:

$$t_{eh} = t_w + 0.125b \left(\frac{b}{a} \right) \left[1 + 0.172 \left(\frac{b}{a} \right)^2 \right]. \quad (3.19)$$

The effective length of the open tonehole t_e differs depending on whether there is a

pad present above the hole or not. In the case that no pad is present,

$$t_e = \frac{k^{-1} \tan(kt_{eh}) + b[1.40 - 0.58(b/a)^2]}{1 - 0.61kb \tan(kt_{eh})}. \quad (3.20)$$

In the case that a pad of diameter D_p is placed an average height h above the tonehole,

$$t_e = \frac{(1/k) \tan(kt_{eh}) + b\{0.61(D_p/2b)^{0.18}(b/h)^{0.39} + (\pi/4)[1 - 0.74(b/a)^2]\}}{1 - 0.61(D_p/2b)^{0.18}(b/h)^{0.39}kb \tan(kt_{eh})}. \quad (3.21)$$

The specific resistance ξ_e accounts for thermoviscous losses along the tonehole walls and the radiation at the open end:

$$\xi_e = 0.25(kb)^2 + \alpha t_{eh} + (1/4)kd_v \ln(2b/r_c), \quad (3.22)$$

where r_c is the radius of curvature of the internal and external ends of the tonehole, $d_v = \sqrt{2\eta/(\rho\Omega)}$ is the viscous boundary layer thickness given in terms of the shear viscosity of air (η) and α is the real part of the complex wave number.

The open- and closed-tonehole series equivalent lengths t_a are given by:

$$\begin{cases} t_a^{(o)} = \frac{0.47b(b/a)^4}{\tanh(1.84t_{eh}/b) + 0.62(b/a)^2 + 0.64(b/a)} \\ t_a^{(c)} = \frac{0.47b(b/a)^4}{\coth(1.84t_{eh}/b) + 0.62(b/a)^2 + 0.64(b/a)}. \end{cases} \quad (3.23)$$

For a combined main bore and tonehole system shown in Fig. 3.3, where the tonehole is exactly centered on the main bore, the pressure P_1 and volume flow U_1 (at the input end) are related with the pressure P_2 and volume flow U_2 (at the output end) by series cascaded transmission matrices:

$$\begin{bmatrix} P_1 \\ U_1 \end{bmatrix} = \begin{bmatrix} TM_l \\ TM_r \end{bmatrix} \begin{bmatrix} TM_{th} \end{bmatrix} \begin{bmatrix} P_2 \\ U_2 \end{bmatrix}, \quad (3.24)$$

where TM_l and TM_r stand for the transmission matrices associated with the main bore on the left and right side of the tonehole, respectively.

The T-section shown in Fig. 3.4 can be further simplified to an L-section, as shown in

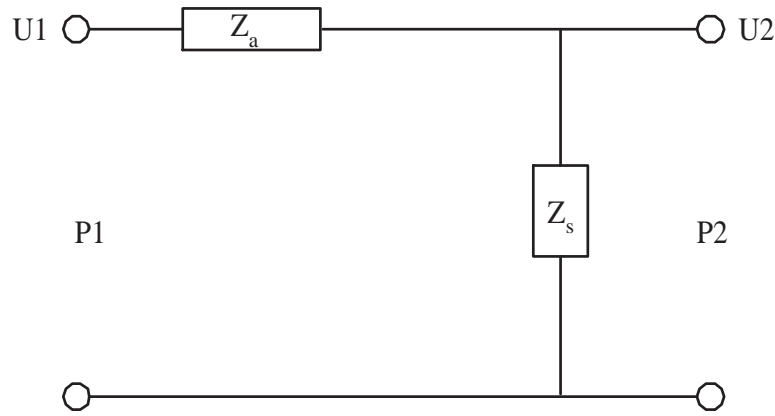


Figure 3.5 L-section.

Fig. 3.5. The TM_{th} becomes:

$$TM_{th} = \begin{bmatrix} 1 & Z_a \\ 0 & 1 \end{bmatrix} \begin{bmatrix} 1 & 0 \\ Z_s^{-1} & 1 \end{bmatrix} = \begin{bmatrix} 1 + \frac{Z_a}{Z_s} & Z_a \\ Z_s^{-1} & 1 \end{bmatrix}. \quad (3.25)$$

In the limit $|Z_a/Z_s| \ll 1$, the transmission matrix TM_{th} of both T-section and L-section reduces to:

$$TM_{th} = \begin{bmatrix} 1 & Z_a \\ Z_s^{-1} & 1 \end{bmatrix}. \quad (3.26)$$

3.3 Refinement of Tonehole Model

In Keefe's T-section tonehole model, the tonehole section in the transmission network is characterized by series impedances Z_a and shunt impedances Z_s that are given by Eq. (3.17). The purely imaginary series impedance Z_a is a negative acoustic inertance, accounting for the acoustic mass reduction due to the influence of the side hole. It can be interpreted as a negative length correction to the main bore. The shunt impedance Z_s of a closed hole is an acoustic compliance that accounts for the closed hole volume. The shunt impedance of an open hole is an acoustic inertance that accounts for both inner and outer length corrections and the tonehole chimney height. The real part of Z_s accounts for the thermoviscous and radiative dissipation.

The basic T-section model was refined in (Nederveen et al., 1998) and (Dubos et al.,

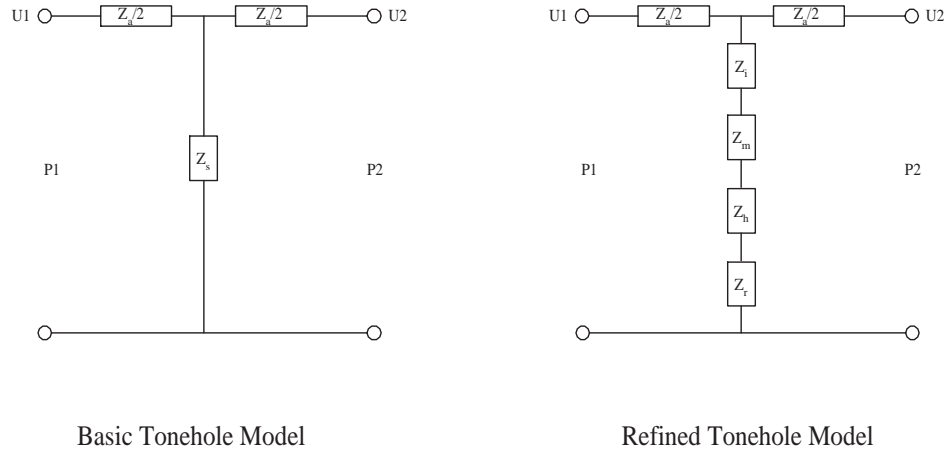


Figure 3.6 Equivalent circuit of the basic tonehole model and the refined tonehole model.

1999), where extra compliance and inertance changes were taken into account by additional correction elements. The refined model is shown in Fig. 3.6. The combined shunt impedance Z_s consists of four parts in series. The transitional impedance Z_i corresponds to the transitional effect due to the flow splitting. The matching volume impedance Z_m takes the extra volume between the main tube and the hole into account. The hole impedance Z_h corresponds to the cylindrical part of the hole. Z_r is the radiation impedance at the open end of the hole. These impedance elements are represented by length corrections, which are determined by the hole geometry dimensions.

The series impedance of the open hole is given by:

$$Z_a^{(o)} = jkZ_0t_a^{(o)}. \quad (3.27)$$

The series length correction t_a is given by (Nederveen et al., 1998):

$$t_a^{(o)} = -0.28b\delta^2, \quad (3.28)$$

where $\delta = b/a$ with b representing the hole radius and a being the main bore radius while Z_0 is the characteristic impedance of main bore.

The shunt impedance of the open hole is given by:

$$Z_s^{(o)} = jkZ_{ch}t_i + jZ_{ch} \tan[k(t_w + t_r + t_m)], \quad (3.29)$$

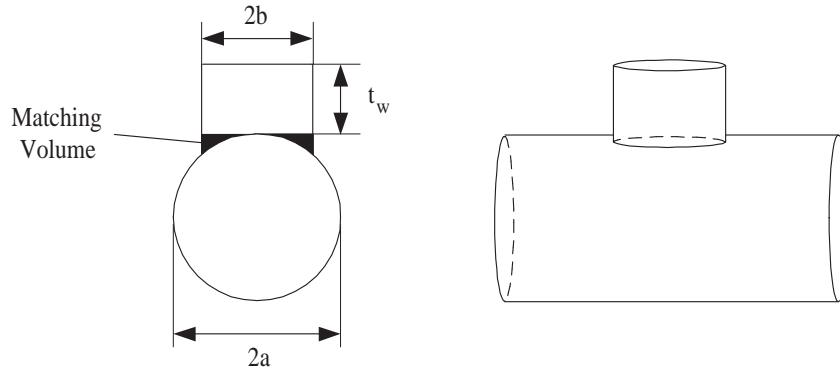


Figure 3.7 A tonehole in the middle of a main pipe, the matching volume area is colored in black.

where $Z_{ch} \simeq \rho c / S_h$ is the characteristic impedance of the side hole with the hole cross sectional area $S_h = \pi b^2$, t_i is the inner length correction, t_w is the hole height, t_r is the length correction associated with the radiation impedance Z_r as $t_r = \Im\{\arctan[Z_r / (jZ_{ch})]\} / k$ and $t_m = V_m / S_h$ is the equivalent length accounting for the matching volume V_m (see Fig. 3.7).

For low frequencies where $k(t_w + t_r + t_m) \ll 1$, Eq. (3.29) reduces to:

$$Z_s^{(o)} = jkZ_{ch}(t_i + t_w + t_r + t_m). \quad (3.30)$$

The inner length correction t_i is given by Nederveen et al. (1998) as:

$$t_i = (0.82 - 1.4\delta^2 + 0.75\delta^{2.7})b. \quad (3.31)$$

The equivalent matching length t_m is:

$$t_m = \frac{b\delta}{8}(1 + 0.207\delta^3). \quad (3.32)$$

The length correction t_r associated with the radiation impedance of the open hole is

given as follows (Dalmont et al., 2002; Dalmont, 2001):

$$t_r = \begin{cases} (0.82 - 0.15\epsilon - 0.06\epsilon^6)b & \text{for tube of finite thickness (circular flange)} \\ 0.82b - 0.47\delta^{0.8} & \text{for tube of cylindrical flange} \\ 0.82b \left[1 + \frac{(0.77kb)^2}{1 + 0.77kb} \right]^{-1} & \text{for tube of infinite flange} \end{cases} \quad (3.33)$$

where b is the internal radius of the open hole, $\epsilon = b/d$ is the ratio of internal radius and the external radius ($d = b + \text{tube wall thickness}$).

More accurate result can be obtained by taking the losses of the toneholes into account. In (Dalmont et al., 2002), both linear losses (including thermoviscous losses and radiation losses) for the case of small amplitude and low frequencies as well as non-linear losses in the case of large amplitude and high frequencies are discussed.

The linear thermoviscous losses in a cylindrical tonehole is taken into account by using the complex wave number:

$$\Gamma = \Omega/c + (1 - j)\alpha, \quad (3.34)$$

where $\alpha = 2.96 \times 10^{-5} \sqrt{f}/b$, f is the frequency in Hz and b is the radius of the tonehole in meters.

For low frequencies ($ka \ll 1$), the linear radiation losses are taken into account by introducing a real part of the radiation impedance Z_r :

$$\Re\{Z_r\} = \begin{cases} (ka)^2/4, & \text{for unflanged tube} \\ (ka)^2/2, & \text{for infinitely flanged tube.} \end{cases} \quad (3.35)$$

Figure 3.8 shows the input impedance of a cylindrical bore with an open hole in the middle (refer to Fig. 3.7). The length and the radius of the main bore are 0.1 meters and 0.01 meters, respectively. The hole radius is 0.007 meters, the hole height is 0.0101 meters. The main bore is modeled by a transmission network. The open hole is modeled alternatively by Keefe's model and the refined open hole mode with the low amplitude assumption.

The refined open hole model is only accurate for small amplitudes. For large amplitudes, it was found through experimentation (Dalmont et al., 2002) that both the series

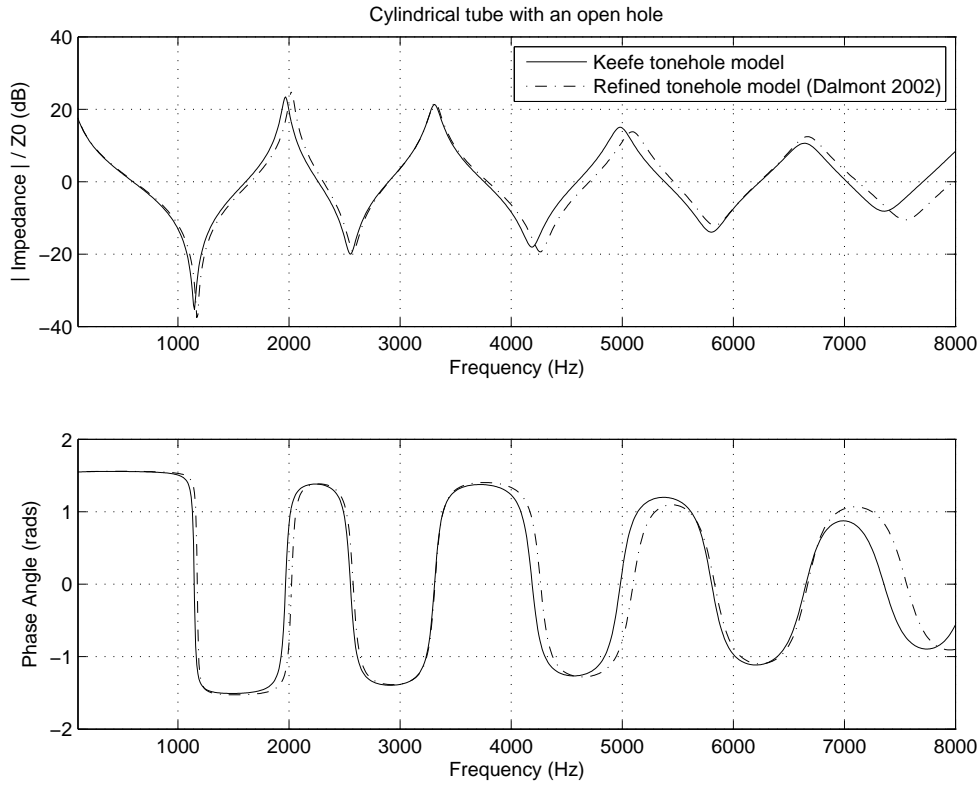


Figure 3.8 The Keefe tonehole model vs. the refined open hole model in (Dalmont et al., 2002).

and shunt impedances should be corrected by a non-linear resistive term, which is a function of the velocity in the tone hole and the edge sharpness. Although no analytical solution is available yet for this non-linear resistive term, some parametric empirical models are given in (Dalmont et al., 2002).

The correction term for the series impedance is:

$$\Re\{Z_a^{(o)}\} = K_a M_h Z_c, \quad (3.36)$$

where K_a is $0.4 \pm 0.05/\delta^2$ for holes with sharp edges and slightly smaller for rounded edges, $M_h = v_h/c$ is the Mach number with the average velocity over the cross section of the side hole and Z_c is the characteristic acoustic impedance of main bore.

The correction term for the shunt impedance is:

$$\Re\{Z_s^{(o)} - Z_{rlin}\} = K_h M_h Z_{ch}, \quad (3.37)$$

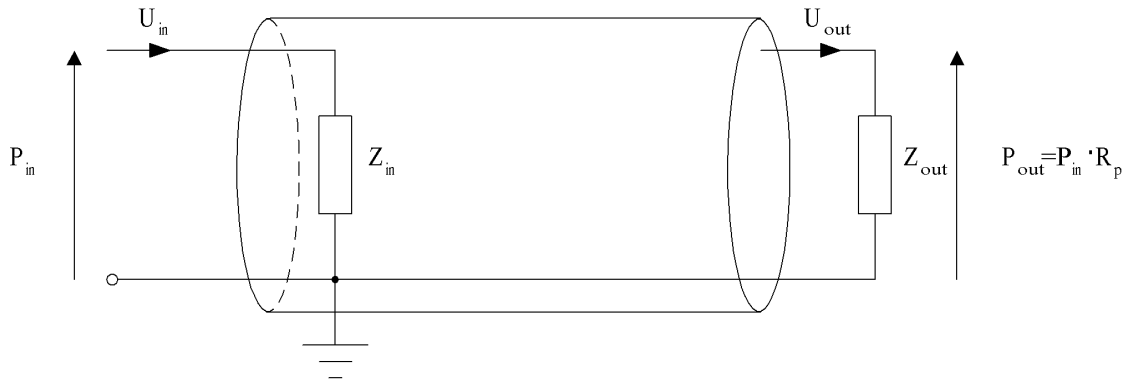


Figure 3.9 The transmission line model of a cylindrical bore.

where K_h is 0.6 ± 0.1 for 7mm radius hole, 0.5 ± 0.1 for 5mm radius with sharp edges, and 0.3 ± 0.1 for hole with rounded corner and Z_{ch} is the characteristic acoustic impedance of side hole.

3.4 Radiation Model of a Main Bore with Toneholes

As discussed so far, a woodwind instrument bore can be approximated as a cascade of cylindrical or conical segments. The main bore and the toneholes are represented by a transmission network. The radiation at the end of the open holes and the pipe end can be modeled by the results of Levine and Schwinger (1948). In this section, we discuss the radiation model of a main bore with toneholes, which is mainly based on the work of Rousseau (1996).

3.4.1 Bore Segment

The bore segment modeled by a transmission line is illustrated in Fig. 3.9. The pressure P_{in} , volume velocity U_{in} at the input end, the pressure P_{out} and volume velocity U_{out} at the output end are related by the associated transmission matrix represented by Eq. (2.24). We restate it here for convenience:

$$\begin{bmatrix} P_{in} \\ U_{in} \end{bmatrix} = \begin{bmatrix} A & B \\ C & D \end{bmatrix} \begin{bmatrix} P_{out} \\ U_{out} \end{bmatrix}. \quad (3.38)$$

Equation (3.38) can be re-written as:

$$\frac{P_{in}}{P_{out}} \begin{bmatrix} 1 \\ Z_{in}^{-1} \end{bmatrix} = \begin{bmatrix} A & B \\ C & D \end{bmatrix} \cdot \begin{bmatrix} 1 \\ Z_{out}^{-1} \end{bmatrix} = \begin{bmatrix} \alpha_b \\ \beta_b \end{bmatrix}, \quad (3.39)$$

where $Z_{in} = P_{in}/U_{in}$ is the impedance seen from the input end and $Z_{out} = P_{out}/U_{out} = Z_L$ is the load impedance at the output end.

The bore segment with a given load impedance and transmission matrix can be fully represented by the terms α_b and β_b . We can calculate the input impedance and the transfer function of input/output pressure from α_b and β_b :

$$Z_{in} \triangleq \frac{P_{in}}{U_{in}} = \frac{\alpha_b}{\beta_b} \quad (3.40)$$

and

$$R_p \triangleq \frac{P_{out}}{P_{in}} = \frac{1}{\alpha_b}, \quad (3.41)$$

where

$$\begin{cases} \alpha_b = A + B/Z_{out} \\ \beta_b = C + D/Z_{out}. \end{cases} \quad (3.42)$$

3.4.2 Tonehole Segment

The tonehole segment modeled by the transmission network is illustrated in Fig. 3.10. Given the assumption $|Z_a/Z_s| \ll 1$, the hole segment is represented by the simplified transmission matrix TM_{th} given in Eq. (3.26), as:

$$TM_{th} = \begin{bmatrix} A_{th} & B_{th} \\ C_{th} & D_{th} \end{bmatrix} = \begin{bmatrix} 1 & Z_a \\ Z_s^{-1} & 1 \end{bmatrix}. \quad (3.43)$$

Likewise, the pressure P_{in} , volume velocity U_{in} at the input end, the pressure P_{out} and volume velocity U_{out} at the output end are related by the associated transmission matrix as:

$$\begin{bmatrix} P_{in} \\ U_{in} \end{bmatrix} = \begin{bmatrix} A_{th} & B_{th} \\ C_{th} & D_{th} \end{bmatrix} \begin{bmatrix} P_{out} \\ U_{out} \end{bmatrix}. \quad (3.44)$$

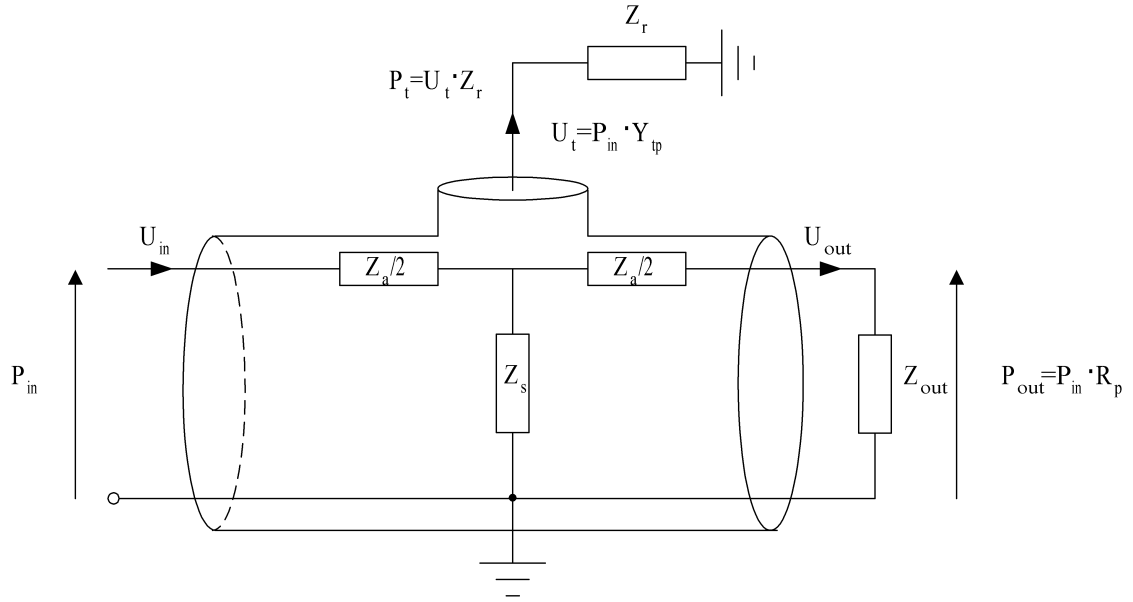


Figure 3.10 The transmission line model of a tonehole.

Given

$$\begin{cases} \alpha_{th} = A_{th} + B_{th}/Z_{out} \\ \beta_{th} = C_{th} + D_{th}/Z_{out}, \end{cases} \quad (3.45)$$

we can calculate the input impedance

$$Z_{in} = \frac{\alpha_{th}}{\beta_{th}} \quad (3.46)$$

and the transfer function of input/output pressure

$$R_p = \frac{1}{\alpha_{th}}. \quad (3.47)$$

Given the assumption $|Z_a/Z_s| \ll 1$ and $Z_r \approx 0$, the exit velocity U_t at the open hole end is related to the input pressure P_{in} by the radiation admittance Y_{tp} :

$$\begin{aligned} Y_{tp} &\triangleq \frac{U_t}{P_{in}} \\ &= \frac{Z_{out} + Z_a/2}{(Z_{out} + Z_a) \cdot Z_s}. \end{aligned} \quad (3.48)$$

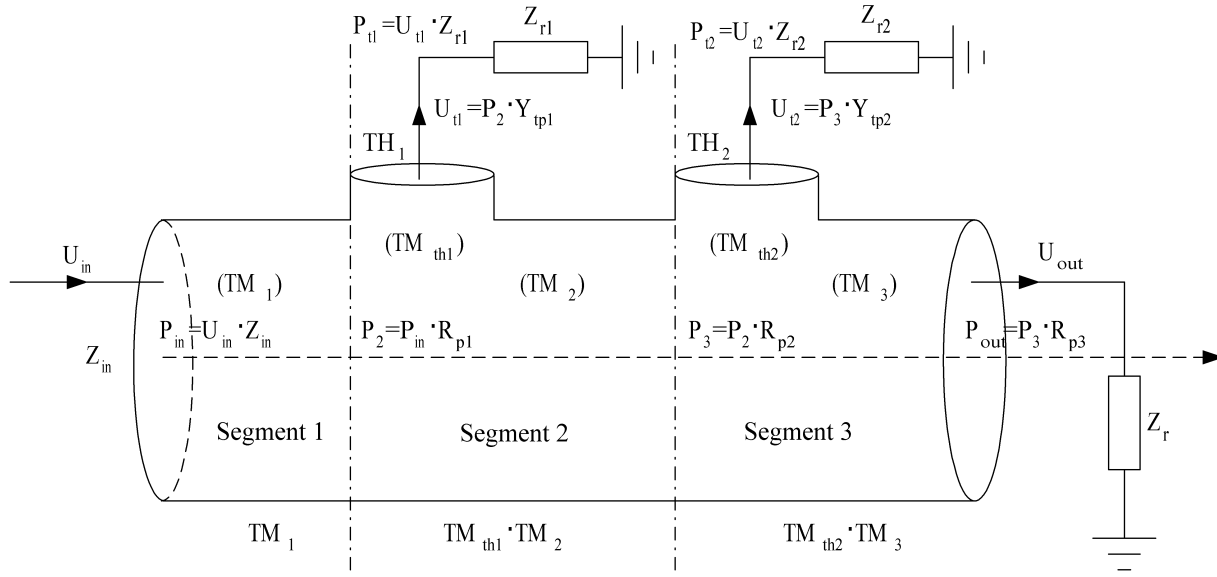


Figure 3.11 The transmission line model of a main bore with two toneholes.

3.4.3 An Example of a Main Bore with Two Toneholes

Figure 3.11 illustrates the transmission line model of a cylindrical bore with two open side holes. The main bore is divided into three segments, characterized by transmission matrices TM_1 , TM_2 and TM_3 , respectively. The two toneholes TH_1 and TH_2 are characterized by TM_{th1} and TM_{th2} accordingly.

For engineering convenience, the hole models are integrated into the bore models, such that the transmission matrices of segment 2 and 3 become $TM_2^* = TM_{th1} \cdot TM_2$ and $TM_3^* = TM_{th2} \cdot TM_3$, respectively.

The radiation impedance Z_r at the bore output end, and Z_{r1} and Z_{r2} at the hole output ends, are evaluated by the radiation model for an unflanged cylindrical pipe (Levine and Schwinger, 1948). Then starting from the last segment at the bore output end, the input impedance Z_{in} of each segment is calculated from the load impedance and the associated transmission matrix by using Eq. (3.40) iteratively, until the input impedance of the entire system is obtained. The internal pressure transfer function R_p of each segment is calculated by Eq. (3.41). Note that for the bore segment with a hole, the internal pressure transfer function becomes $R_p^* = R_p / \alpha_{th}$. The radiation admittance Y_{tp} associated with each tonehole element is calculated by Eq. (3.48).

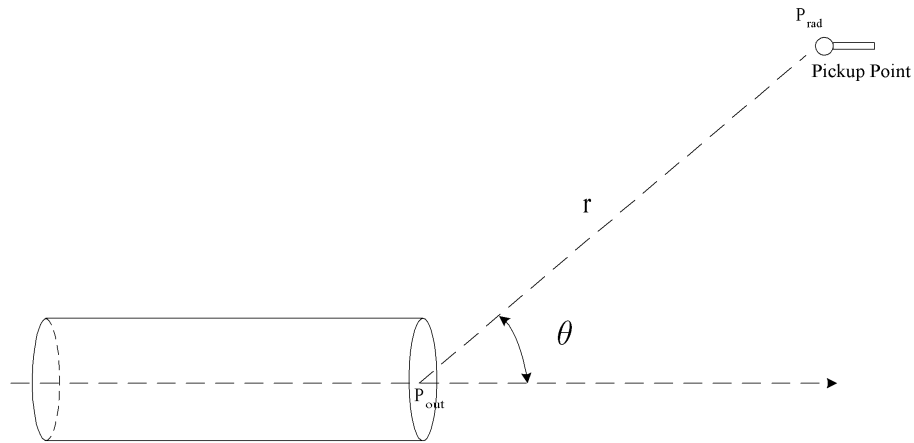


Figure 3.12 Radiation sound pressure measured at angle θ and distance r from the pipe end.

If the input velocity U_{in} or the input pressure P_{in} is known, we can calculate P_2 and P_3 , the input pressure of each tonehole, and P_{out} , the wave pressure at the bore output end. The exit velocity U_t of each open hole is calculated from the input pressure and the radiation admittance, i.e. $U_{t1} = P_2 \cdot Y_{tp1}$, $U_{t2} = P_3 \cdot Y_{tp2}$. The output pressure at each open hole end is then obtained by the product of exit velocity and radiation impedance, i.e. $P_{t1} = U_{t1} \cdot Z_{r1}$, $P_{t2} = U_{t2} \cdot Z_{r2}$.

3.5 Directivity

The acoustic model we discussed so far mainly concerns the internal sound field. The overall output sound pressure can be approximated by simply summing up the output sound pressure at the output end of all open holes and the main bore. This model can be improved by taking the directivity factor into account, which is a function of radiation distance and angle.

3.5.1 Power Gain Directivity

For cylindrical pipe with an infinite flanged end, the radiated intensity is given by (Fletcher and Rossing, 1991):

$$\left[\frac{2J_1(ka \sin \theta)}{ka \sin \theta} \right]^2,$$

where $\theta \in [-90^\circ, 90^\circ]$ is the angle measured from the axis of the pipe, as shown in Fig. 3.12.

For most woodwind-like instruments, the unflanged pipe model would be more appropriate. The angular distribution of the sound radiated from the unflanged pipe end is given by a power-gain directivity function (Levine and Schwinger, 1948)¹:

$$G(\theta) = \frac{4}{\pi \sin^2 \theta} \frac{J_1(ka \sin \theta)}{[(J_1(ka \sin \theta))^2 + (N_1(ka \sin \theta))^2]^{1/2}} \frac{|R|}{1 - |R|^2} \times \exp \left[\frac{2ka \cos \theta}{\pi} P \int_0^{ka} \frac{x \tan^{-1}(-J_1(x)/N_1(x)) dx}{[x^2 - (ka \sin \theta)^2][(ka)^2 - x^2]^{1/2}} \right], \quad (3.49)$$

where the angle $\theta \in [0^\circ, 360^\circ]$, R is the reflectance, a is the pipe radius, k is the wave number, $J_1(x)$ is the first-order Bessel function of the first kind, $N_1(x)$ is the first-order Neumann function and $I_1(x)$ and $K_1(x)$ are modified Bessel functions.

Equation (3.49) is rather complex. Practically, an approximation provided in (Levine and Schwinger, 1948) is appropriate for normal engineering applications²:

$$G(\theta) = \frac{1}{N} \left(\frac{J_1(ka \sin \theta)}{ka \sin \theta} \right)^2 \frac{1}{1 - |R|^2} [(1 + \cos \theta)^2 - 2 \sin^2 \theta \Re R + (\cos \theta - 1)^2 |R|^2], \quad (3.50)$$

where $|R|$ is the modulus of the reflectance. In (Rousseau, 1996), it was approximated by the fit formula³:

$$|R| \approx e^{\frac{-(ka)^2}{2}} \left[1 + \frac{(ka)^4}{6} \left(\log \frac{1}{ka\gamma} + \frac{19}{12} \right) \right] \quad (3.51)$$

for $ka < 1$, and

$$|R| \approx \sqrt{\pi ka} \cdot e^{-ka} \left(1 + \frac{3}{32(ka)^2} \right) \quad (3.52)$$

for $1 < ka < 3.5$, where γ is a constant here given by $\log(\gamma) = 0.5772$.

¹This equation was originally from Eq. (VI.8) in (Levine and Schwinger, 1948). The term $(ka)^2 + x^2$ at the denominator of the integral was corrected to $(ka)^2 - x^2$ in (Ando, 1968).

²This equation was originally from Eq. (VII.5) in (Levine and Schwinger, 1948), which was then corrected in (Ando, 1968). Note that a term "ka" is missed in Eq. (A.2) of (Ando, 1968).

³It can also be approximated by Eq. (3.14).

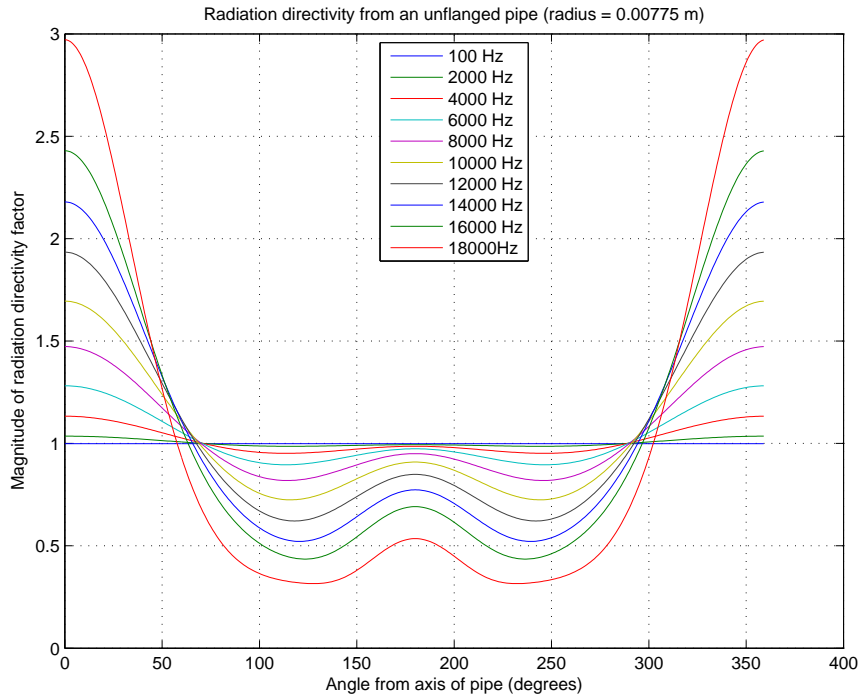


Figure 3.13 Radiation pressure directivity factor.

3.5.2 Pressure Directivity

For practical convenience, the power gain directivity $G(\theta)$ is divided by a normalization constant N such that $\int_0^{2\pi} \frac{G(\theta)}{N} \sin \theta d\theta = 1$. The normalized sound pressure directivity factor can be obtained from the square root of $G(\theta)$ as $P(\theta) = \sqrt{G(\theta)/N}$. The phase delay corresponding to the distance r is represented by a frequency-dependent term e^{-jrk} . Taking these factors into account, the radiation pressure directivity factor corresponding to an external pickup point is given by:

$$\text{Factor}(\theta, r) = e^{-jrk} \cdot P(\theta). \quad (3.53)$$

Figure 3.13 shows the radiation pressure directivity factor calculated for an unflanged cylindrical pipe of 7.75 mm radius using Eq. (3.53). The directivity patterns of the same pipe for several frequencies (500, 5000, 7000, 11000, 13000, 17000 Hz) in polar plots are illustrated in Fig. 3.14.

The radiation sound pressure P_{rad} is obtained by multiplying the output sound pres-

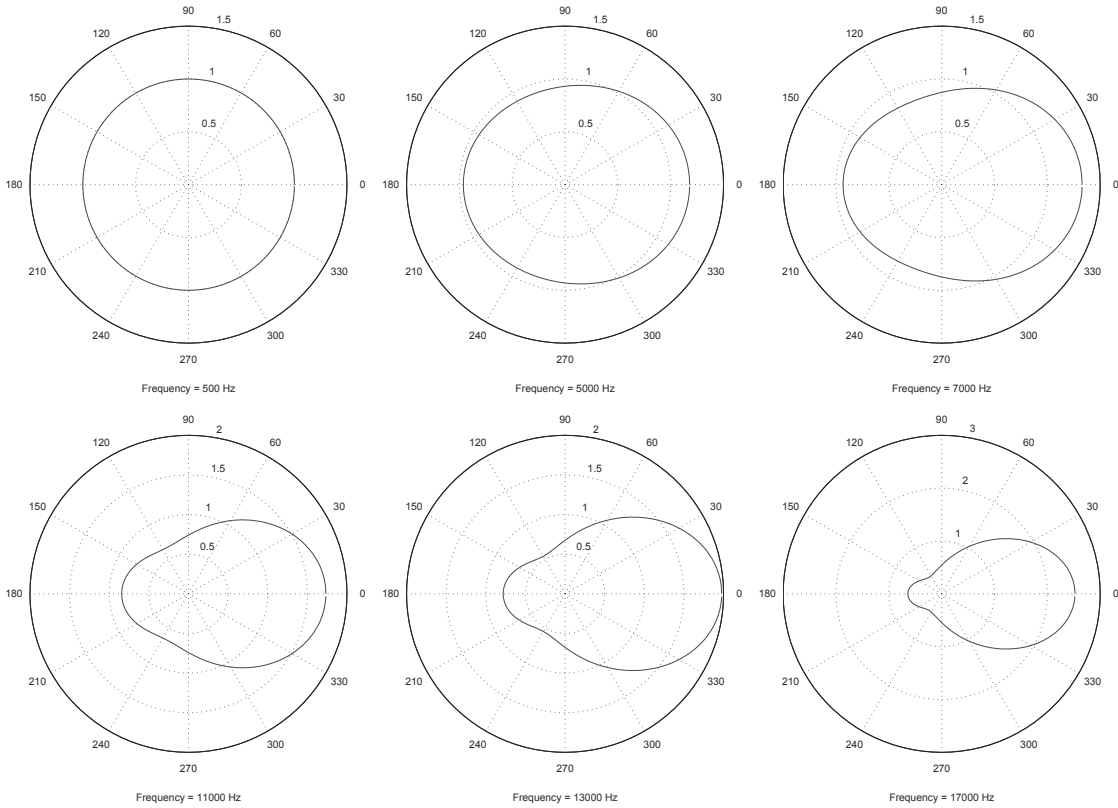


Figure 3.14 Radiation pressure directivity factor in polar plots.

sure P_{out} by the pressure directivity factor:

$$P_{rad}(\theta, r) = P_{out} \cdot \text{Factor}(\theta, r). \quad (3.54)$$

The overall radiation pressure of a woodwind instrument consisting of multiple radiation sources can be calculated by summing up the radiation components from each individual radiation source:

$$P_{rad}(\theta, r) = \sum_{i=1}^M P_{out(i)} \cdot \text{Factor}(\theta_i, r_i), \quad (3.55)$$

where i is the index of individual holes and M is the total number of open holes.

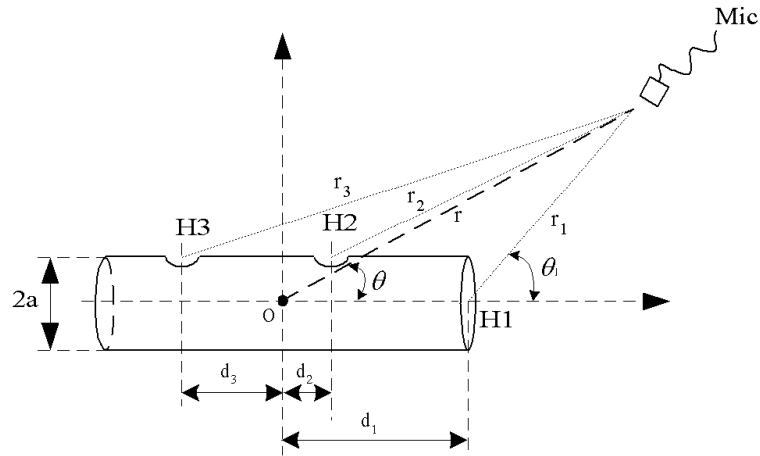


Figure 3.15 Calculation of radiation distances and angles.

3.5.3 Radiation Distance and Angle

For the pipe illustrated in Fig. 3.15, if the distance from the pipe to the pickup point is long enough compared to the geometry dimension of the pipe end ($r \gg d_i, r \gg a$), the radiation distances and angles can be approximated by far-field formulas:

$$r_i \approx r - d_i \cos(\theta) \quad (3.56)$$

$$\theta_i \approx \begin{cases} \theta & \text{for pipe end,} \\ \theta - \pi/2 & \text{for side holes.} \end{cases} \quad (3.57)$$

where d_i is the horizontal distance measured from the reference point O to the hole H_i .

If the pickup point is not far away from the pipe, the far-field assumption is no longer valid. For this case, the near-field formulas are used:

$$r_i = \sqrt{r^2 - 2rd_i \cos(\theta) + d_i^2} \quad (3.58)$$

$$\theta_i = \begin{cases} \arccos\left(\frac{r \cos(\theta) - d_i}{r_i}\right) & \text{for pipe end,} \\ \arccos\left(\frac{r \cos(\theta) - d_i}{r_i}\right) - \pi/2 & \text{for side holes.} \end{cases} \quad (3.59)$$

In some cases, it is more convenient to set the reference point on the surface of the pipe. Figure 3.16 gives such an example, where the pickup point is underneath the pipe.

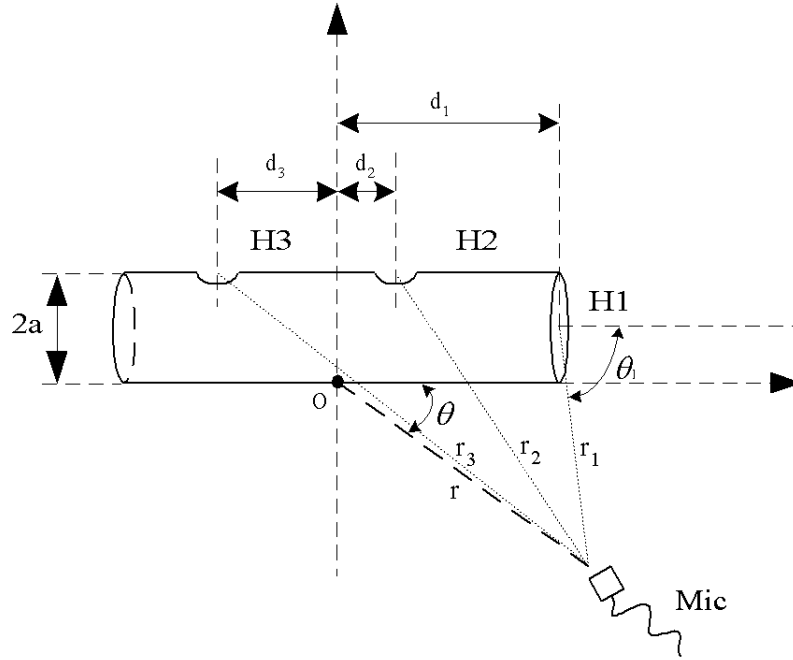


Figure 3.16 Calculation of radiation distances and angles (with a reference point underneath the pipe).

In the near-field situation, the pipe radius should be taken into account. The formulas of radiation distances and angles for such configuration are given by:

$$r_i = \begin{cases} \sqrt{r^2 - 2rd_i \cos(\theta) + d_i^2 + a^2 + 2ar \sin(\theta)} & \text{for pipe end,} \\ \sqrt{r^2 - 2rd_i \cos(\theta) + d_i^2 + 4a^2 + 4ar \sin(\theta)} & \text{for side holes.} \end{cases} \quad (3.60)$$

$$\theta_i = \begin{cases} \arccos\left(\frac{r \cos \theta - d_i}{r_i}\right) & \text{for pipe end,} \\ \arccos\left(\frac{r \cos \theta - d_i}{r_i}\right) - \pi/2 & \text{for side holes.} \end{cases} \quad (3.61)$$

Chapter 4

Reflectometry Measurement Technique

The computational woodwind radiation directivity model can be verified by experimental measurement. The radiation directivity pattern can be visualized either by polar plots, as shown in Fig. 3.14, or by the radiation pressure transfer function, which is defined as the complex ratio of the sound radiation pressure to the internal sound pressure.

Intuitively, the radiation directivity can be measured in the frequency domain. An experimental measurement was presented in (Ando, 1968). The radiation directivity pattern of a circular pipe of finite length was compared to an unflanged cylindrical pipe radiation model (Levine and Schwinger, 1948). The pressure responses were measured continuously at angles from 0-180 degrees. The system was stimulated by both continuous and pulsed sinusoidal signals, and similar results were obtained. The measurement results were found to resemble the theoretical results, particularly when $ka \leq 1.90$. It was reported that better theoretical estimation was obtained when the outside radius of the pipe was used rather than the inside one.

Rousseau (1996) measured the radiation directivity of the oboe and the flute using a similar method. The instrument was excited by a sinusoidal signal of various frequencies sent from a miniature loudspeaker. The radiation signal captured by a microphone was filtered to remove the broad band noise and then sent to a B&K polar tracer to produce the polar plot over a full 360 degrees.

In this thesis, the time domain pulse reflectometry technique was employed to measure the radiation directivity of a cylindrical pipe with toneholes. An obvious advantage of this technique is that the radiation directivity over a continuous range of frequencies

at a certain angle can be measured in a one-shot measurement. Also, good signal-to-noise ratio can be obtained by using long-duration source signals, such that it is possible to perform the measurement in a damped room rather than in an anechoic chamber.

4.1 History of Pulse Reflectometry Technique

The history of the pulse reflectometry technique is briefly introduced here. A comprehensive review can be found in (Sharp, 1996). This measurement technique was originally developed to study the stratifications in the earth's crust in the oil exploration industry (Ware and Aki, 1969). In the nineteen seventies and eighties, it was used to measure airway dimensions: the animals' and human's vocal tracts and lungs were modeled as a series of cylindrical segments with equal lengths but different cross-sectional areas. Benade and Smith (1981) first attempted to use this technique for musical wind instrument measurements, where a spark discharge was fed into the mouthpiece of tubas and the impedance function was obtained from the FFT of a reflectogram. As the deconvolution technique was developed successfully in late eighties (Deane, 1986), the broadband source signals can be generated more conveniently and consistently by loudspeakers where better signal-to-noise ratios could be achieved.

Sharp (1996) developed a practical acoustic pulse reflectometry apparatus and presented a method to measure the input impulse response, bore profile and input impedance of musical wind instruments, as well as leak detection and localization.

Kemp (2002) studied the sound propagation in acoustic cylindrical and rectangular ducts using multimodal propagation theory, where the resonance frequencies and radiation were characterized by a multimodal input impedance and a multimodal radiation impedance, respectively. To verify the model, stepped tubes and trumpet bell sections were measured using the acoustic pulse reflectometry technique.

Lefebvre et al. (2007) presented a novel variant of pulse reflectometry using a long-duration source signal. The input impedance of an alto saxophone neck and fabricated conical objects were measured using both a two-microphone transfer function method and the pulse reflectometry method. Good agreement was shown between the two methods.

Recently, Buckiewicz-Smith (2008) measured the input impedance of several wind instrument bodies and mouthpieces using both the two-microphone transfer function

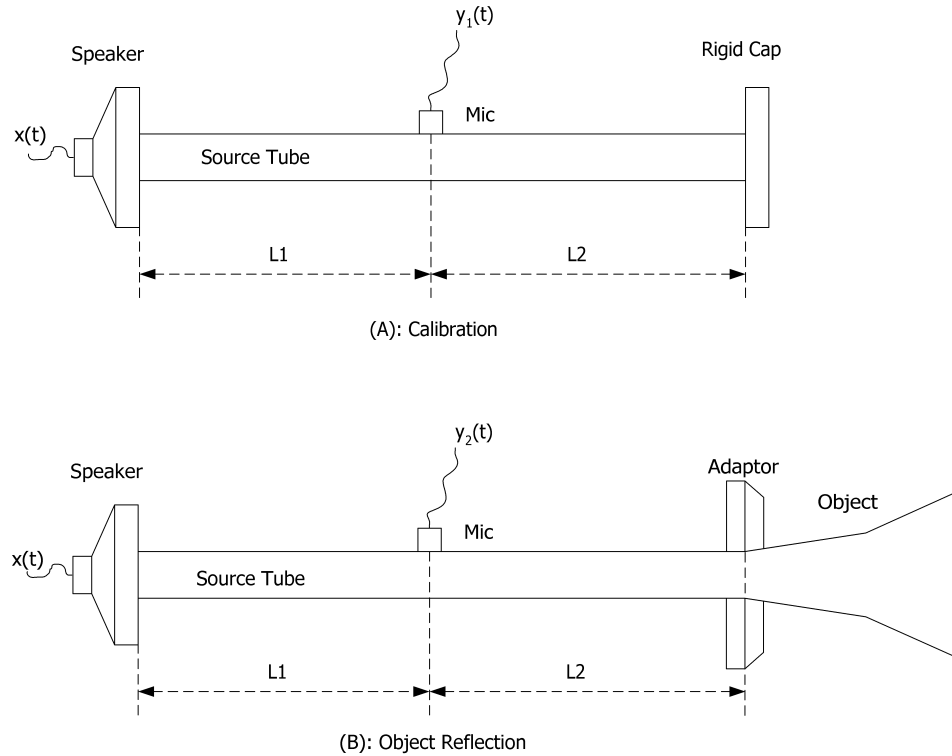


Figure 4.1 Reflectometry setup for input impedance measurement.

method and the pulse reflectometry method. He also compared several types of source signals and discussed the corresponding construction and deconvolution methods.

4.2 Reflectometry Technique for Input Impedance Measurement

Figure 4.1 shows the schematic diagram of the acoustic pulse reflectometer used in (Sharp, 1996; Kemp, 2002; Li, 2004), which was similar to the apparatus used by Lefebvre et al. and Buckiewicz-Smith, except that the source signals and data processing methods were different.

For analysis purposes, assume the source signal $x(t)$ is an ideal impulse emitted by the speaker. In the calibration setup shown in Fig. 4.1 (A), the output end of the source tube is terminated by a rigid cap. Theoretically, the impedance of the rigid termination is infinite, which has a constant reflection coefficient of 1 for all frequencies. The input pulse $x_{cal}(t)$ is windowed out from the complicated signal $y_1(t)$ recorded by the micro-

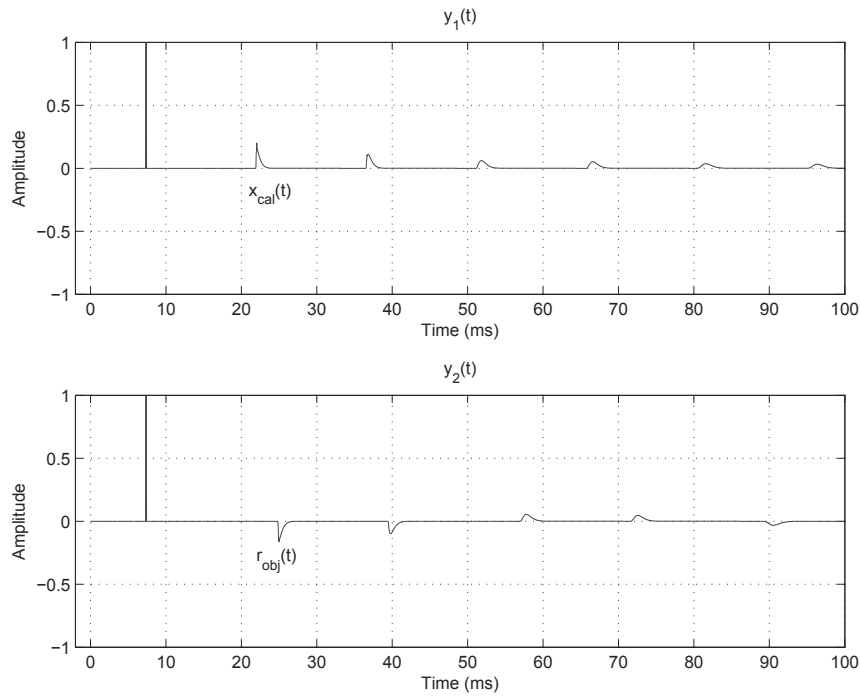


Figure 4.2 The signals were calculated from a digital waveguide model simulating the pulse reflectometry system, where the source reflectance was approximated by a constant coefficient 1. Top: $y_1(t)$ is the recorded complicated signal of calibration. Bottom: $y_2(t)$ is the recorded complicated signal of object reflection.

phone, as shown in Fig. 4.2 (top). The calibration measurement ensures that both the input pulse and the object reflection experience the same wall losses corresponding to the same length, such that the influence of the source tube is canceled out.

In the object reflection setup shown in Fig. 4.1 (B), the input end of the source tube is connected to a horn driver loudspeaker. The output end is attached to the object to be measured. The source signal $x(t)$ travels from the loudspeaker down the source tube, passes by the microphone, continues to travel forward until it reaches the entry of the object to be measured, then is partly transmitted into the object duct and partly reflected back as the object reflection. The reflected signal will continue to travel backward down the source tube until it hits the source loudspeaker and is partly reflected back, and so on and so forth. The complicated signal $y_2(t)$ passing the microphone is sampled and recorded. The first reflection from the object, $r_{obj}(t)$, can be inspected and windowed out from $y_2(t)$, as shown in Fig. 4.2 (bottom). The length L_2 is chosen to be long enough

such that the object reflection can be separated explicitly from the forward-going source signal. Likewise, the length L_1 should be long enough to make sure that the recorded reflection signal from the object is not contaminated by further reflections returning from the source speaker. Specifically, the round trip time $t = (2L_1)/c$ should be longer than the length of the first reflection from the object, where c is the speed of sound.

The reflectance at the input end of the measured object can then be calculated from the constraining deconvolution (Sharp, 1996; Kemp, 2002; Li, 2004), or the object reflection $r_{obj}(t)$ divided by the input pulse $x_{cal}(t)$ in the frequency domain:

$$R_{in}(f) = \frac{R_{obj}(f)X_{cal}^*(f)}{X_{cal}(f)X_{cal}^*(f) + q}, \quad (4.1)$$

where $R_{in}(f)$ is the input reflectance of the object to be measured, f is the physical frequency, $R_{obj}(f)$ is the Fourier Transform of the object reflection $r_{obj}(t)$, $X_{cal}(f)$ is the Fourier Transform of the input pulse $x_{cal}(t)$, $X_{cal}^*(f)$ is the complex conjugate of $X_{cal}(f)$ and q is the constraining factor preventing potential zero division, where $q = 0.00001$ in (Kemp, 2002).

The normalized input impedance of the measured object can then be obtained from the input reflectance:

$$\bar{Z}_{in} = \frac{1 + R_{in}(f)}{1 - R_{in}(f)}. \quad (4.2)$$

Lefebvre et al. (2007) refined the process by using a long-duration swept sinusoidal signal as the stimulus signal, in contrast to the short duration pulse signal used in traditional pulse reflectometry techniques. The measurement signal-to-noise ratio can be greatly increased because a lot more energy is injected into the system.

Using this new method, the impulse response of the system connected with the object is calculated by the following steps: (1) Deconvolving the measured signal $y_2(t)$ from the source signal $x(t)$, where the first reflection pulse from the measured object $r_{obj}(t)$ can then be inspected and windowed out from the full impulse response; (2) The same process is applied to the calibration signal $y_1(t)$ recorded from the system closed by the rigid cap to obtain the input pulse $x_{cal}(t)$; (3) The input reflectance of the measured object is calculated by dividing the first reflection coming from the object by the input pulse

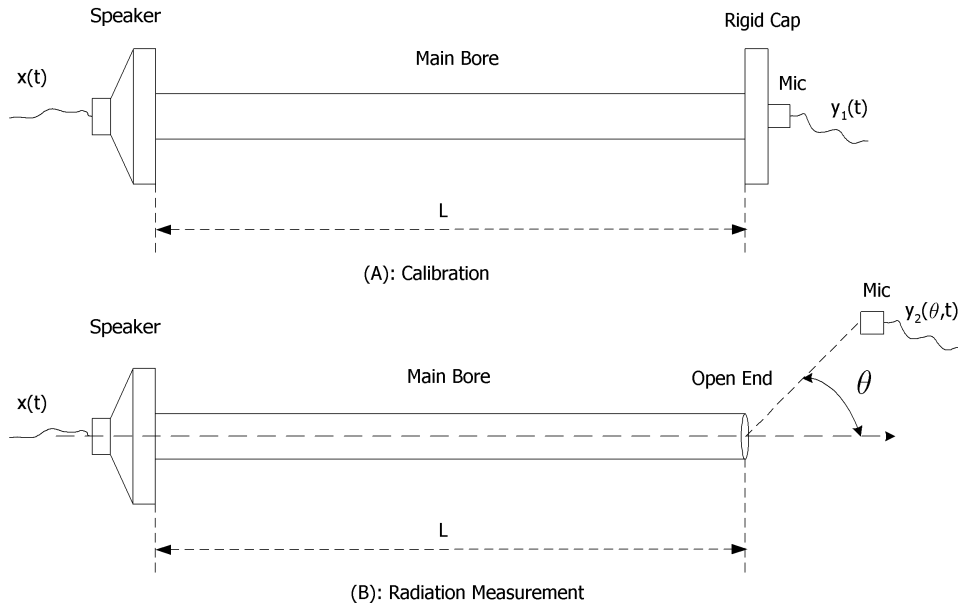


Figure 4.3 Reflectometry setup for radiation pressure directivity measurement.

signal in the frequency domain:

$$R_{in}(f) = \frac{R_{obj}(f)}{X_{cal}(f)}. \quad (4.3)$$

This refinement method was further elaborated and verified in (Buckiewicz-Smith, 2008), where different types of stimulus signals, such as periodic pulses, Maximum Length Sequences (MLSs), Golay Codes, swept sines, etc., were discussed and compared. The swept sine signal was found to be a preferred source signal for input impedance measurement in that it did a good job of handling the artifacts of non-linearity, environment noise, and DC offset.

4.3 Impulse Reflectometry for Radiation Measurement

4.3.1 Setup

To measure the radiation of a woodwind-like instrument, the pulse reflectometry setup in Fig. 4.1 is modified accordingly. The schematic diagram is illustrated in Fig. 4.3.

The calibration setup is shown in Fig. 4.3 (A). A horn driver loudspeaker is attached

to the input end of the main bore. The output end is closed by a rigid cap, which has a small hole drilled through its center. A miniature microphone is embedded in the center hole. The acoustic pressure at the rigid termination of the main bore is sampled and recorded as the calibration signal.

The radiation measurement setup is shown in Fig. 4.3 (B). The same microphone detached from the rigid cap is placed at the pickup point. The radiation signal at distance r and angle θ from the output end of the main bore is measured. To simplify the problem, the distance can be fixed as a constant for all angles.

4.3.2 Theory

Here we assume that all the interactions within the system are linear and time-invariant. If we denote the stimulus signal at the input end of the main bore as $x(t)$ and the combined dissipation effects (thermoviscous boundary layer, sound wave propagation delay, etc.) of the main bore of length L as $h_L(t)$, then the signal traveling from the input end to the output end of the pipe is $f(t) = x(t) * h_L(t)$. The calibration signal is an infinite sum of reflections:

$$y_1(t) = f(t) * \delta(t - T) + f(t) * h_L(t) * h_L(t) * \delta(t - 3T) + \dots, \quad (4.4)$$

where T is the sound wave propagation time corresponding to the pipe length L .

The radiation signal at angle θ is:

$$y_2(\theta, t) = f(t) * [1 + r(t)] * h(\theta, t) * \delta(t - T) + \\ f(t) * r(t) * h_L(t) * h_L(t) * [1 + r(t)] * h(\theta, t) * \delta(t - 3T) + \dots, \quad (4.5)$$

where $r(t)$ is the reflection function at the open end of the unflanged pipe and $h(\theta, t)$ is the directivity factor filter incorporated with the extra time delay corresponding to the radiation distance.

The impulse response series can then be obtained by deconvolving the measured

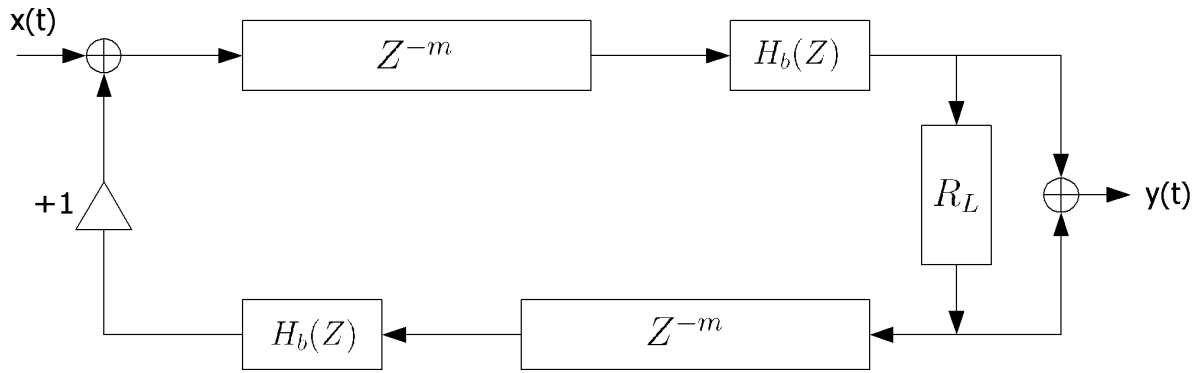


Figure 4.4 Digital waveguide model of the impulse reflectometry.

signal from the source signal $x(t)$:

$$\begin{aligned} ir_1(t) &= \Re \left\{ \text{IFFT} \left[\frac{\text{FFT}(y_1(t))}{\text{FFT}(x(t))} \right] \right\} \\ ir_2(\theta, t) &= \Re \left\{ \text{IFFT} \left[\frac{\text{FFT}(y_2(\theta, t))}{\text{FFT}(x(t))} \right] \right\}, \end{aligned} \quad (4.6)$$

where $ir_1(t)$ is the impulse response series of the calibration system (terminated with rigid cap) and $ir_2(\theta, t)$ is the impulse response series of the radiation system (open end) of angle θ . The source signal $x(t)$ should be zero-padded to the same length as $y_1(t)$ and $y_2(\theta, t)$ to make the deconvolution calculation possible. Also, the division operation in the frequency domain should be carried out only over the frequency range where the source signal has energy to prevent division by zero¹.

The first pulse of both impulse responses, $ir_{1w}(t)$ and $ir_{2w}(\theta, t)$, are inspected and windowed out at time range $[T, 3T]$. The radiation pressure transfer function can then be obtained:

$$H_{rad}(\theta, f) = \frac{\text{FFT}(ir_{2w}(\theta, t))}{\text{FFT}(ir_{1w}(t))}. \quad (4.7)$$

4.3.3 Simulation and Verification

To verify the validity of the modified impulse reflectometry technique, the measurement and data processing were simulated using a digital waveguide model illustrated in Fig.

¹In this thesis, the frequency range of 20 Hz to 10 kHz was chosen for the simulation and the measurement.

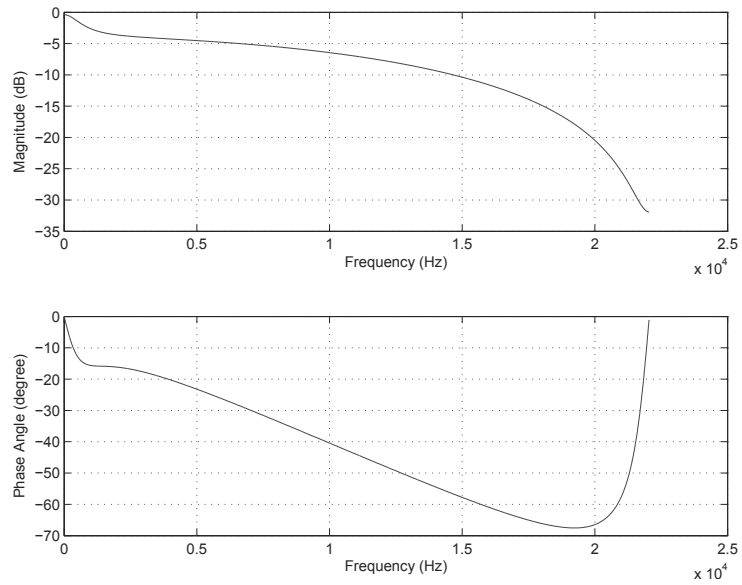


Figure 4.5 Frequency response and phase angle of the boundary layer filter $H_b(Z)$.

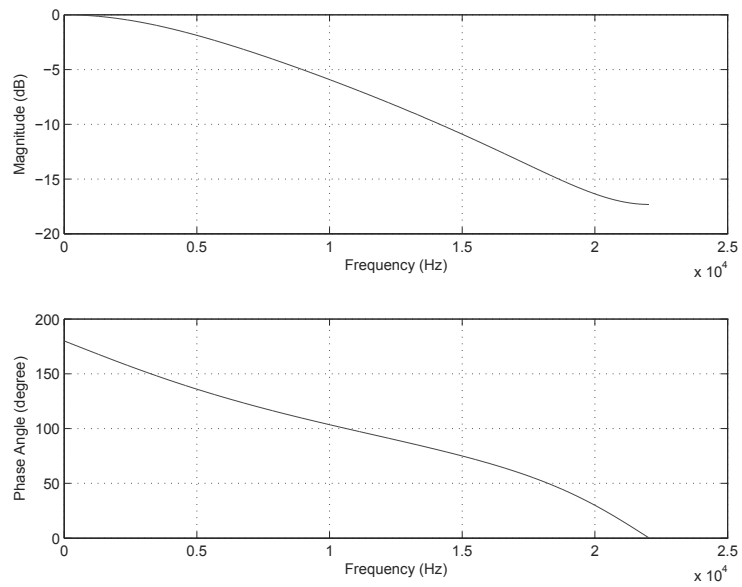


Figure 4.6 Frequency response and phase angle of the reflectance filter R_L .

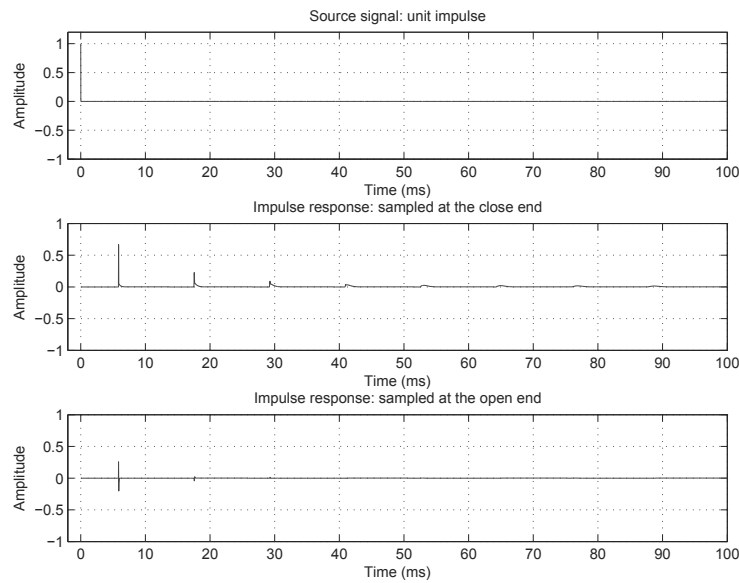


Figure 4.7 Impulse reflectometry model stimulated by unit impulse signal. Top: the ideal unit impulse. Middle: the impulse response sampled at the closed end of the main pipe. Bottom: the impulse response sampled at the open end of the main pipe ($\theta = 0$).

4.4. The main bore (length $L=2$ meters, diameter = 0.0155 meters) was modeled by a dual delay line Z^{-m} , with the delay line length $m = L \cdot f_s/c$, the sampling rate $f_s = 44100$ Hz and c being the speed of sound. The viscous and thermal losses along the wall of the main bore were modeled by a lumped filter $H_b(Z)$ designed by the Matlab function *boundary* given in (Scavone, 1997), as shown in Fig. 4.5. The reflectance at the open end of the main bore was approximated by the radiation solution of the unflanged cylinder (Levine and Schwinger, 1948). The reflectance filter R_L was shown in Fig. 4.6. The reflectance was approximated by 1 for the rigidly closed end. The reflectance of the source end was simply approximated by 1. Although the real situation is much more complicated ², this simplification is appropriate because only the first pulse of the reflection series is of concern, which is not affected by the source reflectance.

First, an ideal unit impulse signal was fed into the digital waveguide. The impulse response series was alternately sampled at the closed end (corresponding to $R_L = 1$) and the open end, as shown in Fig. 4.7. In this case, since the measured signal was exactly

²In the real situation, the source reflectance may be frequency-dependent based on the characteristics of the speaker driver.

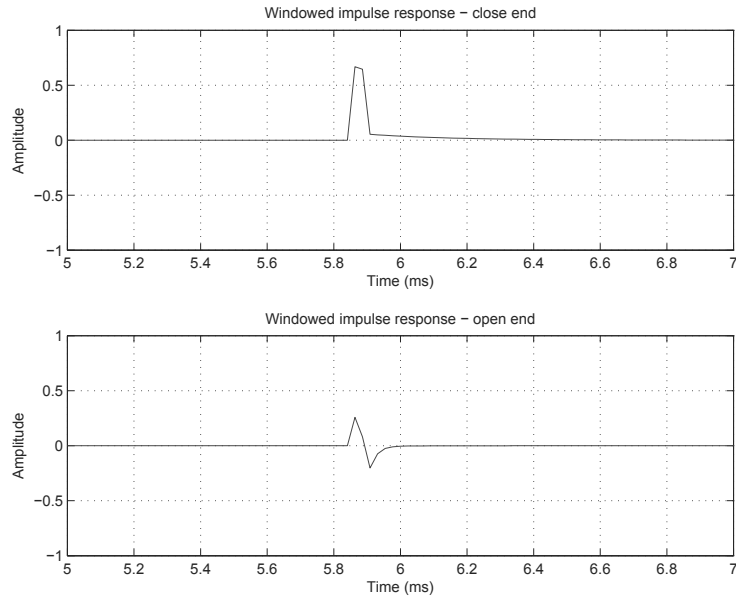


Figure 4.8 Impulse response truncated by rectangular window. Top: the first pulse of the impulse response sampled at the closed end. Bottom: the first pulse of the impulse response sampled at the open end. (system stimulated by unit impulse)

the impulse response of the system, no deconvolution calculation was needed. The first pulse of the impulse response series started at about 5.8 ms after the stimulus signal, which was exactly the time $T = L/c$ that the sound wave needed to travel from the source end to the output end. The second pulse followed the previous one at a $2T$ interval, and the third pulse followed by $2T$, etc. The first pulse of both the calibration signal and radiation signal ($ir_{1w}(t)$ and $ir_{2w}(\theta, t)$ in Eq. (4.7)) were inspected and windowed within the time interval $[0, 3T]$, as shown in Fig. 4.8.

For a second test, a swept sine was used as the stimulus signal, which had a starting frequency 20Hz, an ending frequency 10000Hz, and a duration of $T_{dur} = 2^{18}/f_s$ seconds, with the form (Farina, 2000):

$$x(t) = \sin \left[\frac{\omega_1 \cdot T_{dur}}{\ln(\omega_2/\omega_1)} \cdot \left(e^{\frac{t}{T_{dur}} \cdot \ln(\omega_2/\omega_1)} - 1 \right) \right]. \quad (4.8)$$

The calibration signal and radiation were sampled at the closed end (corresponding to $R_L = 1$) and the open end respectively, as shown in Fig. 4.9. The impulse response series was then deconvolved from the source signal using Eq. (4.6), as shown in Fig. 4.10. The

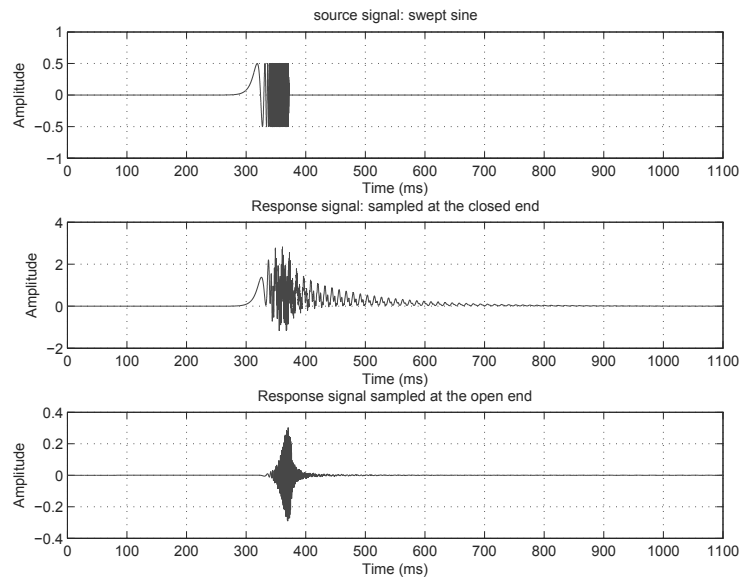


Figure 4.9 Impulse reflectometry model stimulated by swept sine signal. Top: the swept sine signal. Middle: the response sampled at the closed end of the main pipe. Bottom: the response sampled at the open end of the main pipe ($\theta = 0$).

first pulse in the time interval $[0, 3T]$ is shown in Fig. 4.11.

Finally, the radiation pressure transfer function was calculated by Eq. (4.7). Both results are compared in Fig. 4.12, plotted in both linear frequency scale (the upper part) and logarithmic frequency scale (the lower part). The frequency response obtained is that of a highpass filter. There is very good agreement between the result obtained from the swept sine stimulus and from the unit impulse stimulus.

In Fig. 4.9, the peak amplitude of the source signal is only 0.5, while the maximum amplitude of the calibration signal exceeds the normalized unity level. This build-up of energy results from the continuous application of input signal plus reflections from the closed end. For our measurements, this energy build-up can potentially lead to non-linear distortion. Care must be taken to avoid this. Likewise, the recorded signal should be long enough to prevent potential truncation due to the long decay caused by energy build-up.

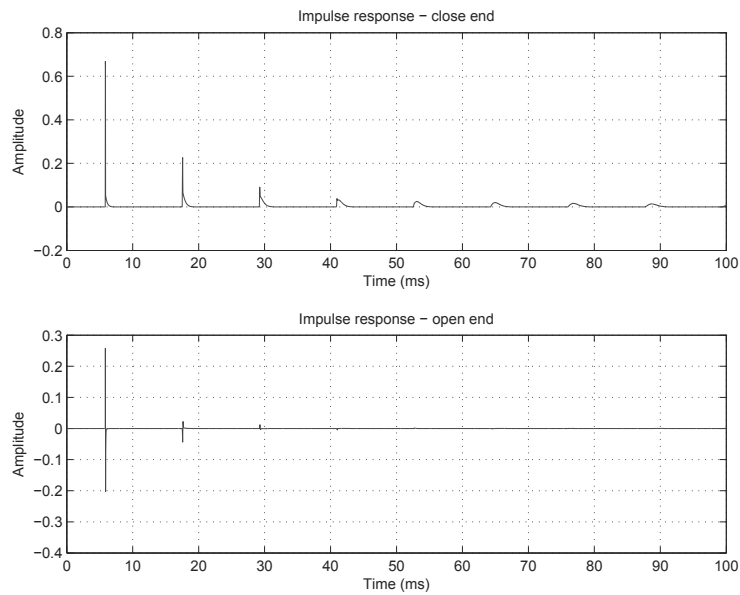


Figure 4.10 Top: the calculated impulse response series at the closed end of the main pipe. Bottom: the calculated impulse response series at the open end of the main pipe. (system stimulated by swept sine)

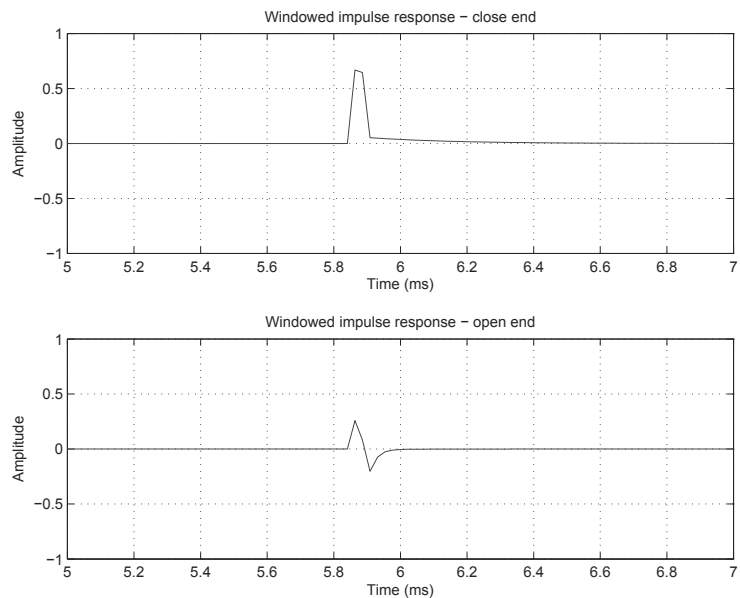


Figure 4.11 Impulse response truncated by rectangular window. Top: the first pulse of the impulse response sampled at the closed end. Bottom: the first pulse of the impulse response sampled at the open end. (system stimulated by swept sine)

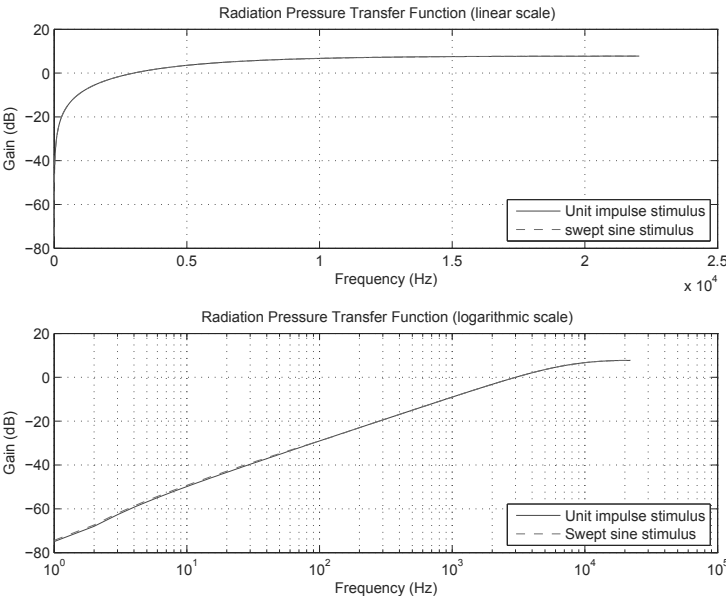


Figure 4.12 Comparison of the radiation pressure transfer function calculated by using different stimulus: unit impulse vs. swept sine.

Chapter 5

Comparison of the Theoretical and Measurement Results

5.1 Measured Objects

The validity of the computational model of radiation directivity was verified by measurement results using a simple acoustical structure. The object measured is an assembly of a long aluminum cylindrical pipe and a short aluminum cylindrical pipe (the radiation extension), as shown in Fig. 5.1. Both pipes have the same inner and outer diameters, seamlessly connected together by an aluminum adaptor. The dimensions of the long pipe are: the length of $L = 2$ meters, the inner diameter of 0.0155 meters, and the outer diameter of 0.0185 meters. The length of the short pipe is $L_1 = 0.148$ meters.

To simulate various fingerings of a real woodwind instrument, five different configurations of three radiation extensions of the same length were used. Extension A is a short cylindrical pipe with an output end (H1). Extension B is drilled with one side

Table 5.1 Fingerings made by different radiation extensions

Fingering Label	Hole H1	Hole H2	Hole H3	Using Radiation Extension
H1	open	N/A	N/A	A
H1H3	open	N/A	open	B
H1H2H3	open	open	open	C
H3	close	N/A	open	B
H2H3	close	open	open	C

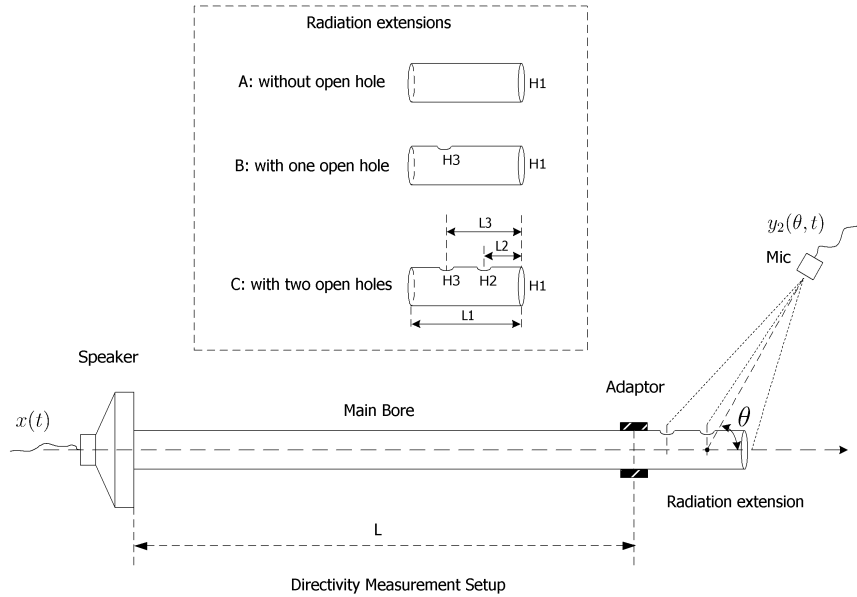


Figure 5.1 Impulse reflectometry setup for radiation directivity measurement.

hole (H3). Extension C is drilled with two side holes (H2 and H3). The distances from the side hole H2 and H3 to the output end H1 are $L_2 = 0.04725$ meters and $L_3 = 0.0945$ meters, respectively. The diameter of all side holes is 0.009 meters. Five different fingerings, labeled as H1, H1H3, H1H2H3, H3 and H2H3 (see Table 5.1), were measured in this study. The last two fingerings, the H3 and H2H3, were made by closing the output end H1 of extensions B and C with duct tape. Although these two fingerings are unusual in real performances of woodwind instruments, they are useful for the study of radiation from toneholes without the influence of the open end of the pipe.

5.2 Theoretical Model

The theoretical model of the measured object was implemented in Matlab using the transmission network technique, with viscous and thermal losses taken into account. A unit input volume velocity was fed into the lossy cylindrical air column model. The exit sound pressure P_{out} at the open end of each tonehole was calculated. The directivity factor of open holes was calculated for various angles. The radiation radius was fixed at $r = 0.12$ meters, measured from the center point between H3 and H1 to the pickup point. The radiation pressure $P_{rad}(\theta, r)$ was calculated using Eq. (3.54) for open holes.

The overall radiation pressure at the pickup point was calculated by summing together the radiation pressures of all open holes.

It should be noted that the model was based on an assumption of one-dimensional wave propagation in the planar mode. Only the fundamental mode was considered and higher-order modes were ignored. Therefore, the validity of the model is restricted to frequencies below the cut-off frequency of the first higher-order mode of the cylindrical pipe, which is given by $f = \frac{1.84c}{2\pi a}$, where c is the speed of sound, a is the cylindrical pipe radius. For the measured object in this study ($a = 0.0155/2$ m, $c \approx 342.511$ m/s at 18.5 degrees Celsius), the cut-off frequency is approximately 12.942 kHz.

5.3 Measurement Setup

The measurements were conducted at the Spatial Audio Lab, CIRMMT, McGill University. The temperature of the room was within 0.1 degrees of 18.5 degrees Celsius over the course of the measurements. The input end of the long pipe was attached to a JBL 2426H compression horn driver, which was driven directly from the line output of an RME Fireface 800 audio interface. The sampling rate was $f_s = 44100$ Hz.

The source signal was a log swept sine of the form given in Eq. (4.8). The starting frequency was $f_1 = 20$ Hz, and the ending frequency was $f_2 = 10000$ Hz.

The radiated sound signal was captured by a Sennheiser KE4-211-2 omni-directional electret microphone capsule, amplified by a Unides Microphone Preamp with the gain set at 26 dB, and then sent to the line input of the RME Fireface.

The calibration measurement was performed first. The output end of the main pipe was closed tightly by an aluminum cap. A microphone was embedded in a small hole drilled through the center of the cap. The response signal, corresponding to the calibration signal ($y_1(t)$) represented in Eq. (4.4), was captured.

Next, the cap was removed and the main pipe was attached to one of the three radiation extensions. The response signal corresponding to Eq. (4.5) was measured by the same microphone for all five fingerings listed in Table 5.1. The microphone was fastened to the center of the hole lattice (the reference point) by a string, such that the distance between the pickup point and the reference point was fixed at 0.12 meters. Measurements were taken at 30 degree intervals within the plane bisecting the side holes and the pipe end.

5.4 Preliminary Measurements

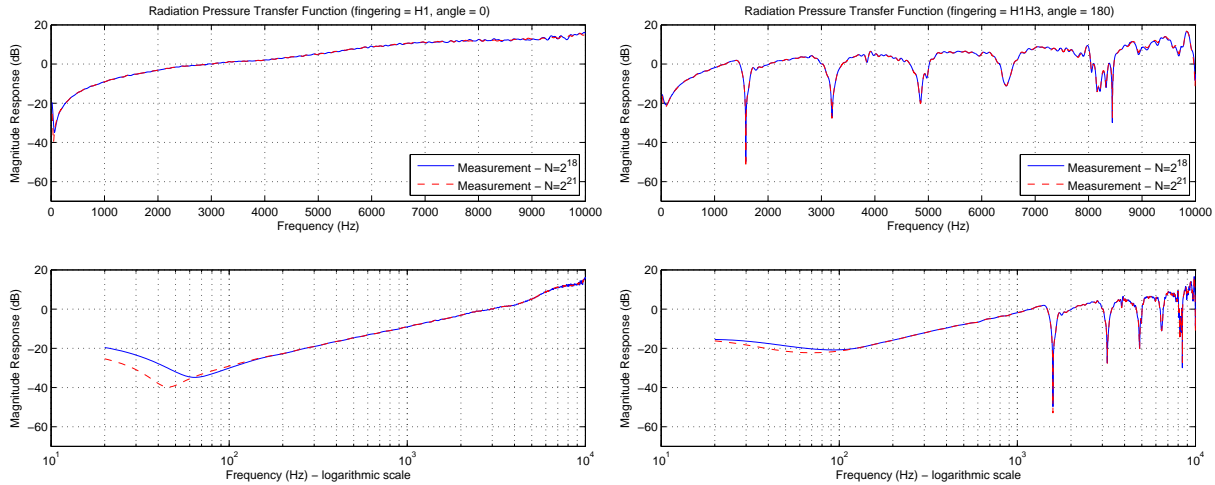


Figure 5.2 Comparison of the measurement results using source signals of different lengths: $N = 2^{18}$ and $N = 2^{21}$. Left: fingering H1 at 0 degrees. Right: fingering H1H3 at 180 degrees.

Preliminary measurements were carried out first to determine the best gain setting of the measurement system, to try different duration of the source signal, and to evaluate the influence of the background noise and room reflections.

Two source signals of different lengths, $N = 2^{18}$ and $N = 2^{21}$ samples, were tested. Theoretically, both source signals should produce the same result, albeit a better signal-to-noise-ratio was expected for the longer one. Figure 5.2 shows the measurement results for fingering H1 at 0 degrees (left) and H1H3 at 180 degrees (right). For frequencies above about 200 Hz, the results corresponding to the two source signals matched well. For frequencies lower than about 200 Hz, the empirical results were not reliable, due to the inability of the driver to produce these frequencies and the fact that the room wall insulation does not attenuate these frequencies as well. The fluctuations in high frequencies above 7000 Hz might be caused by sound reflections from the walls, the measurement devices, and some metal pipes and lighting system fixed to the ceiling. Small ripples appearing at almost all frequencies were probably caused by the noise emitted from the fan of the computer. Therefore, no matter which source signal was used, the measurement was only reliable in the frequency range from about 200-7000 Hz.

5.5 Model Refinements

For most measurement angles and fingerings, the model well matched the measurement to a first approximation. Discrepancies were found in some pickup points, especially for those underneath the main pipe. In order to find possible reasons for the discrepancies, several model refinements were attempted.

5.5.1 Outside Radius

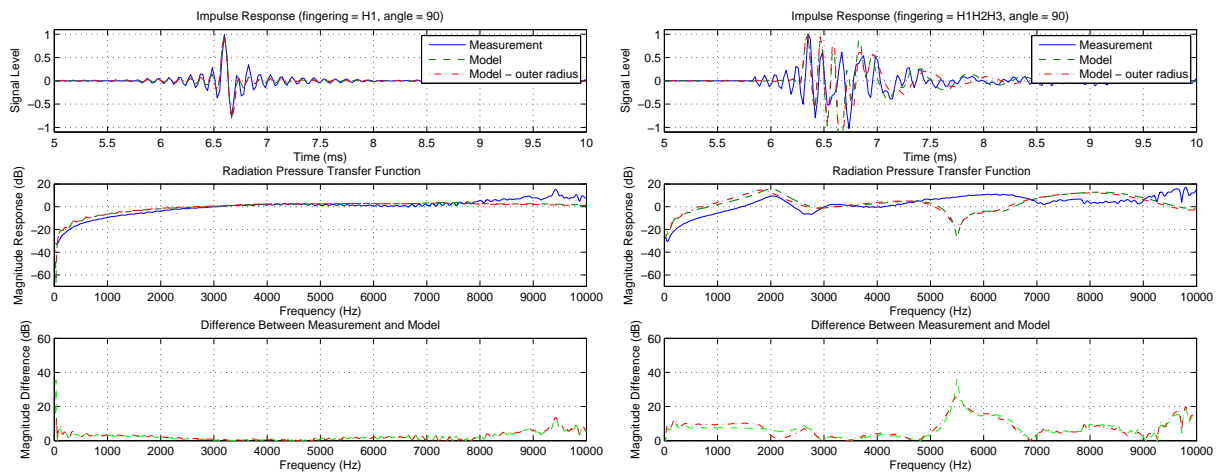


Figure 5.3 Model using inside radius vs. outside radius. Left: fingering H1 at 90 degrees. Right: fingering H1H2H3 at 90 degrees.

As mentioned in (Ando, 1968), it would be better to estimate the directivity characteristic by using the outside radius of the unflanged pipe in the Levine and Schwinger solution¹ rather than the inside radius. In this study, the results using both outside and inside radii were compared. Two examples are illustrated in Fig. 5.3. Both results were compared with the measurement result. Although some minor differences can be observed, there is no convincing evidence that the model using the outer radius is better than that using the inner radius.

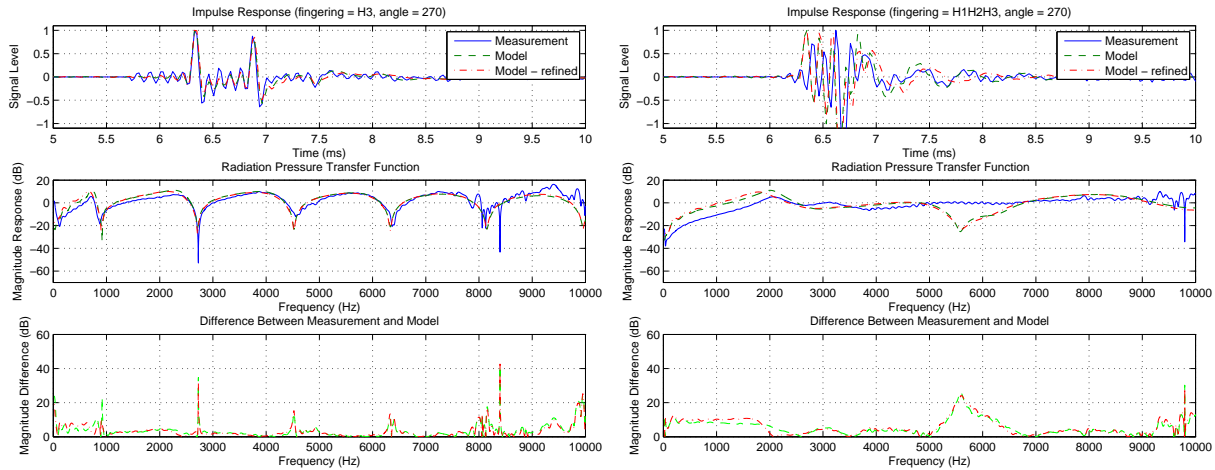


Figure 5.4 Keefe tonehole model vs. Dalmont tonehole model. Left: fingering H3 at 270 degrees. Right: fingering H1H2H3 at 270 degrees.

5.5.2 Refined Open Hole Model

Another model refinement was attempted by using various length corrections mentioned in Sec. 3.3, which include corrections for the pipe radius, the tonehole radius, and the tonehole height. The results corresponding to the pickup point right underneath the main pipe, for fingerings H3 and H1H2H3, were compared in Fig. 5.4. The discrepancies between the refined model and the measurements did not decrease significantly.

5.5.3 Near-field Correction

Initially, the model was computed based on a far-field assumption: the radiation distance between the pickup point and the reference point was long enough compared to the geometry dimension of the hole lattice and the radius of the main pipe. This model was re-calculated by using near-field formulas as given by Eq. (3.58) for pickup points above the pipe ($0 \leq \theta \leq 180$ degrees), and formulas given by Eq. (3.60) and Eq. (3.61) for pickup points underneath the pipe ($210 \leq \theta \leq 330$ degrees, refer to Fig. 3.16). Therefore, the propagation delay overestimated by the far-field model was compensated. The improvement can be observed in Fig. 5.5. The model results were calculated for two cases: fingering H1H2H3 (left) and H2H3 (right) at 270 degrees. The results using far-

¹Equation (3.50) in page 38.

Fingerings	Angles (degrees)
H1H2H3	90, 120, 270
H1H3	120,240, 270
H2H3	60, 90, 120,240, 270

Table 5.2 Improvements were found in these pickup points using near-field model

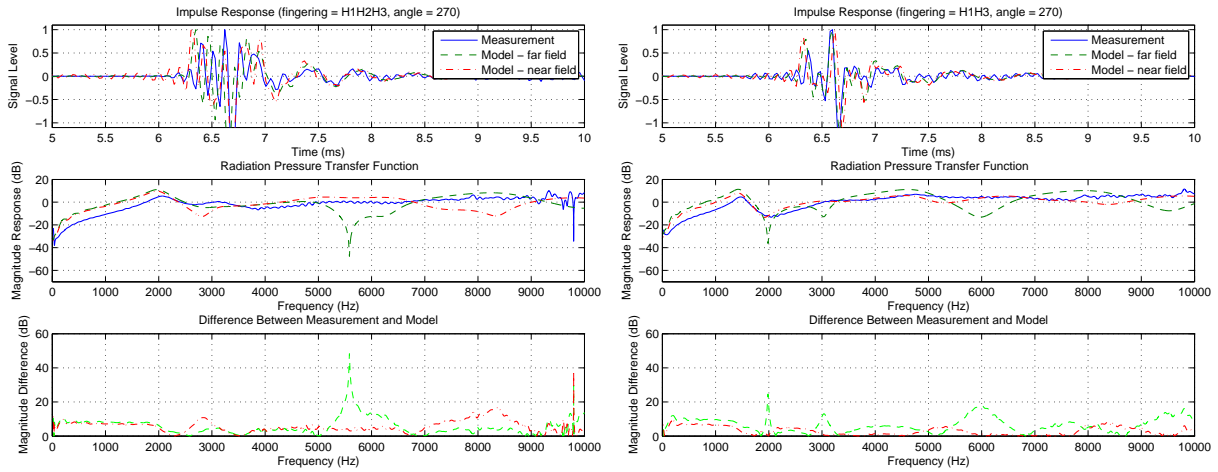


Figure 5.5 Far-field model vs. near-field model. Left: fingering H1H2H3 at 270 degrees. Right: fingering H1H3 at 270 degrees.

field formulas were compared to the results using near-field formulas, as well as the measurements. It turns out that the model results for the fingerings and angles listed in Table 5.2 were improved to some extent.

5.6 Final Measurements

The radiation pressure transfer function of the radiation system was measured by using the reflectometry technique discussed in Sec. 4.3. Measurements were performed at different pickup points for five fingerings. The source signal length was $N = 2^{21}$ samples at a sampling rate of 44100 Hz. The impulse responses was calculated from the inverse Fourier Transform of the transfer functions.

With respect to the model of the measured object, the inside radius of the main pipe was used; the tonehole model was refined by length corrections presented in Sec. 3.3 on the linear and small amplitude assumption; and the radiation distances and angles were

calculated using near-field formulas.

The comparisons between the measurements and the models of all fingerings are illustrated in overlay plots starting from sections A.1 to A.5 of the appendix.

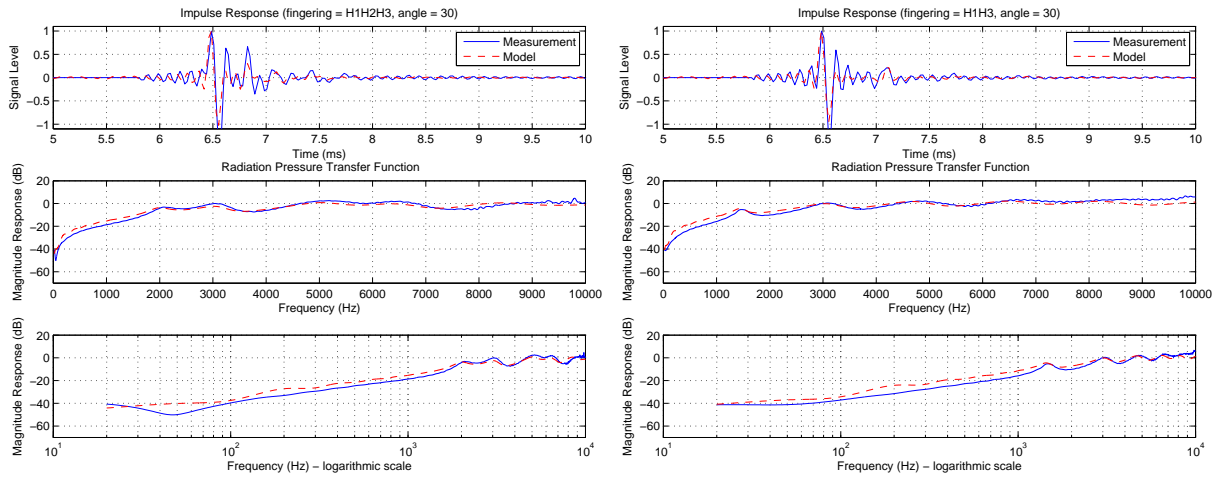


Figure 5.6 Model vs. measurement. Left: fingering H1H2H3, 30 degrees. Right: fingering H1H3, 30 degrees.

Within the reliable frequency range (from about 200 to about 7000 Hz), good first-order agreement was found between the measurements and models for all fingerings and pickup points, in terms of both impulse responses and frequency magnitude profiles.

For example, the responses of the system with fingering H1H2H3 and H1H3 measured at 30 degrees are shown in Fig. 5.6. In the time domain response, the radiated impulse component from the open end of the pipe is first recorded, followed by radiation from the tonehole(s).

For fingerings with a single open hole (H1 and H3), the model predictions of all evaluated pickup points are fairly good. Figure 5.7 shows the responses of the system with fingerings H1 and H3 measured at 150 degrees. In the time-domain response of fingering H3, the radiated impulse component from the hole is first recorded, followed by the pulse reflected from the closed end of the pipe.

The model predictions of fingerings with multiple open holes (H1H3, H2H3, and H1H2H3) are generally poorer than that of single open-hole fingerings. Discrepancies are visible for some pickup points.

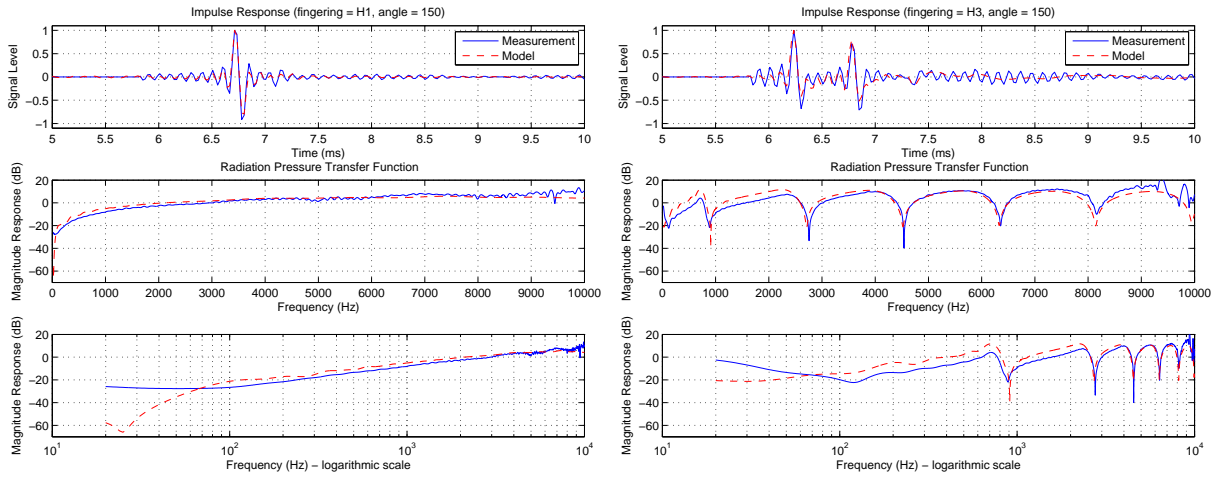


Figure 5.7 Model vs. measurement. Left: fingering H1, 150 degrees. Right: fingering H3, 150 degrees.

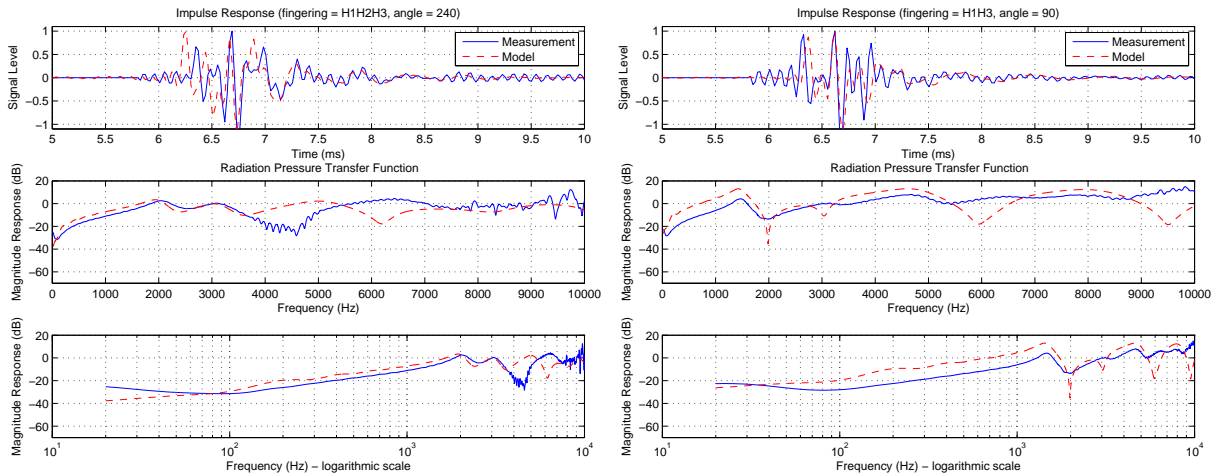


Figure 5.8 Model vs. measurement. Left: fingering H1H2H3, 240 degrees. Right: fingering H1H3, 90 degrees.

For example, the results of fingering H1H2H3 at 240 degrees and H1H3 at 90 degrees are shown in Fig. 5.8. In the time domain response of fingering H1H2H3 at 240 degrees, the first and second pulses (corresponding to side holes H2 and H3) of the model come earlier than that of the measurement. Meanwhile, the phase delays between the first two pulses and the third pulse (coming from the open end of the pipe) of the model are larger than that of the measurement. In the frequency domain, there is a dip around 4500 Hz in the measurement result, while this dip “moves” to about 6200 Hz in the

model. In the time domain response of fingering H1H3 at 90 degrees, the first pulse of the measurement result comes slightly earlier. In the frequency domain, the dips around 2000 Hz, 3000 Hz and 5900 Hz in the model are not found in the measurement.

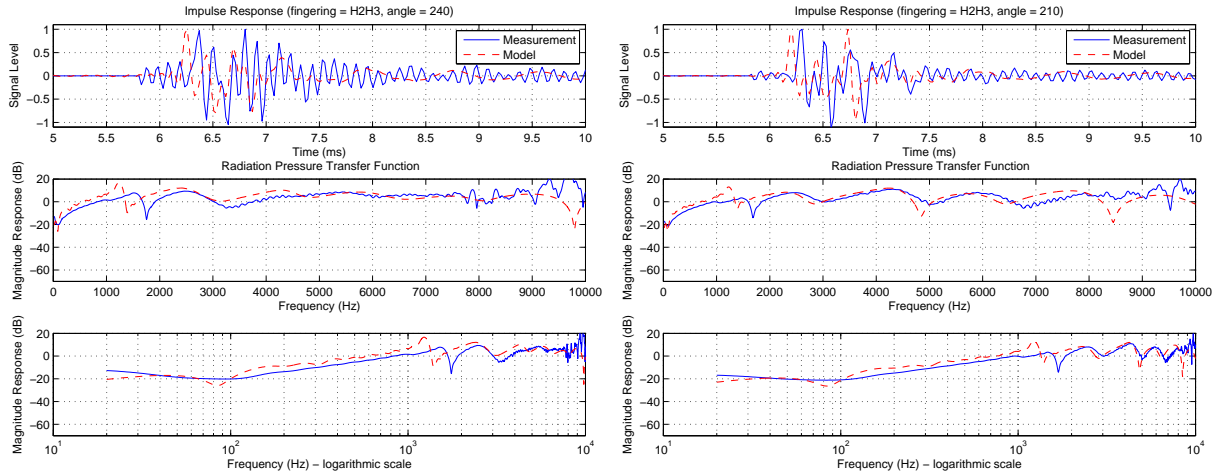


Figure 5.9 Model vs. measurement. Left: fingering H2H3, 240 degrees. Right: fingering H2H3, 210 degrees.

For the results of fingering H2H3, there are consistent discrepancies in the frequency range from 1000-2000 Hz in the frequency domain of all angles. Results at 210 degrees and 240 degrees are shown in Fig. 5.9. In the time domain, consistent ripples are found in the measurement of all angles for this fingering. Given the fact that there are only minor discrepancies of the phase delay between the model and the measurement, the ripples cannot be attributed to the possible inaccuracy of the calculation of radiation distances and angles using the near-field formulas. In fact, these ripples would appear to be the result of a calculation artifact.

By and large, the following results were found to have the most dissimilarity:

- in the time domain: H1H3 at 90, 210, 240, 270, 300 degrees; H2H3 at 210, 240 degrees; and H1H2H3 at 90, 210, 240, 270 degrees.
- in the frequency domain: H1H3 at 90, 210, 240 degrees, H2H3 at 300 degrees, and H1H2H3 at 90, 240, 300 degrees.

Similar discrepancies associated with pickup points underneath the pipe were reported in (Scavone and Karjalainen, 2002). Although the model in this study had been

refined by near-field formulas, these discrepancies still cannot be neglected. On the other hand, good model results were obtained for fingerings with single open holes. The discrepancies might be attributed to not only the near-field geometry issue, but also to other factors (e.g. the acoustic coupling effect between open holes, the cylindrical flange effect, and evanescent modes, etc.).

Chapter 6

Conclusions and Future Work

6.1 Conclusions

The presented work provides a review of a computational modeling technique for woodwindlike musical instruments with arbitrarily shaped bore and finger holes. The model of a simple acoustic structure implemented in Matlab was verified by experimental measurements in terms of radiation directivity.

The basic air column of woodwind instruments is approximated by concatenated piecewise cylindrical and conical segments and modeled by transmission line elements. Wall losses caused by thermoviscous effects are taken into account by using the complex characteristic impedance and propagation wave number, which are functions of the thermoviscous boundary layer thickness. The acoustic impedance at the input end of the entire instrument bore can be calculated from the load impedance at the output end via transmission matrices. The tonehole is modeled by Keefe's solution, which can be refined by length correction terms given in (Dalmont et al., 2002). The transmission line representation of the entire instrument can be constructed by incorporating the transmission elements of toneholes into the transmission network of the bore. The radiation impedances at the output end of the bore and the open holes are calculated based on the radiation model of unflanged cylindrical pipes according to (Levine and Schwinger, 1948). The radiation directivity is taken into account by multiplying the exit pressure at the output end of open holes by the pressure directivity factor given in Sec. 3.5.2.

An assembly of cylindrical ducts and toneholes was used to test the validity of the

model. The transfer function of the radiated pressure at an external pickup point to the wave pressure inside the bore was measured by a modified impulse reflectometry system. To test the validity of the measurement technique, the measurement and data processing were simulated using a digital waveguide system. The final measurements were performed at different pickup points for five fingerings of the measured object. Good first-order agreements were found between the measurements and models, while a few discrepancies were found for fingerings of multiple open holes.

6.2 Future Work

Additional refinements can be made for both the measurement technique and the model in future works.

The measurements of this study were conducted in a highly damped room. Although some steps had been taken, the measured results were inevitably contaminated by reflections from the walls, the ceiling, and the measurement devices. Also, the noise from the computer fan was a big source of contamination. Better results could be obtained by performing the measurement in an anechoic chamber and by placing the noisy computer outside the room.

The angles and distances from the pickup points to the reference point of the object were measured manually using a normal protractor and a ruler. The geometrical measurement accuracy would be greatly improved by using a 64-channel measurement system (see Fig. 6.1) which was due for delivery to the Computational Acoustic Modeling Laboratory at McGill University in September 2008.

The current bore model was based on the presumption of one-dimensional planar wave propagation. Better predictions for high frequencies might be achieved by incorporating evanescent modes in the current model.

The radiation model can be improved by taking the acoustical coupling between adjacent open holes into account. Also for the side hole drilled into a cylindrical main bore (without a chimney), the influence due to the cylindrical flange can be studied in more detail.

The presented work was limited to a cylindrical bore with a non-flaring end. The same comparison between measurement and model could be performed on more complicated objects, such as conical bores, a bore with a bell end, and an arbitrarily shaped

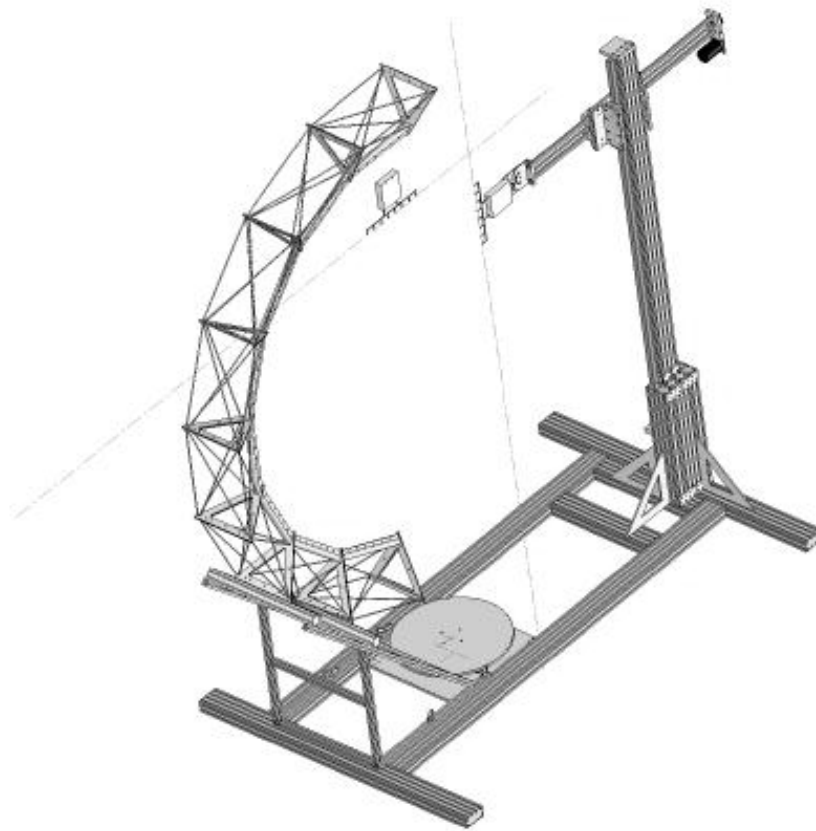


Figure 6.1 The 64-channel Radiation Directivity Measurement System.

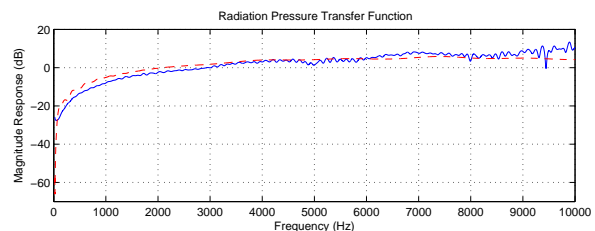
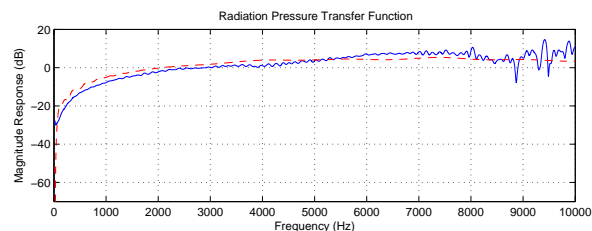
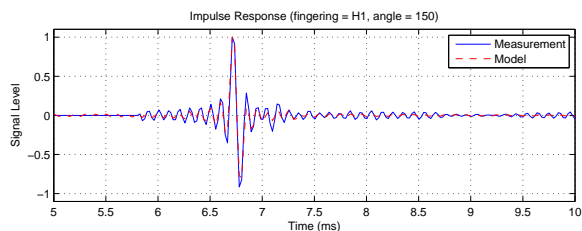
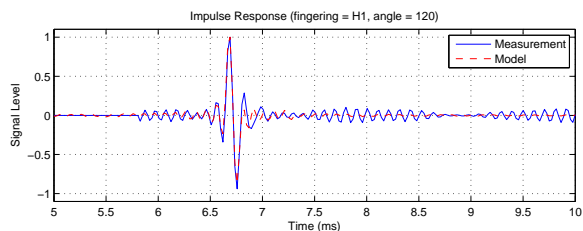
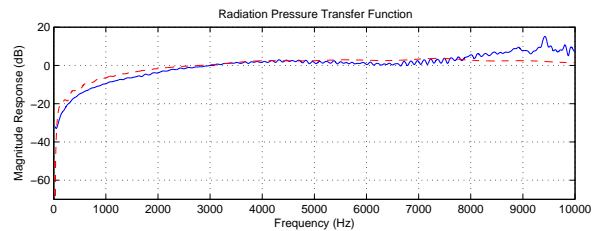
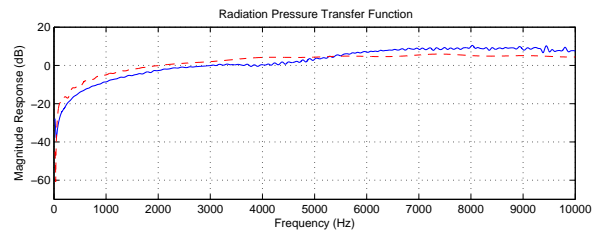
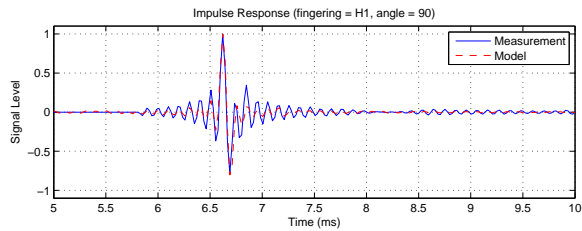
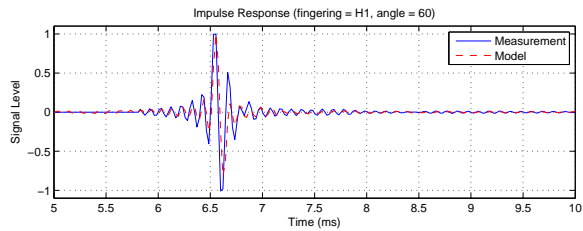
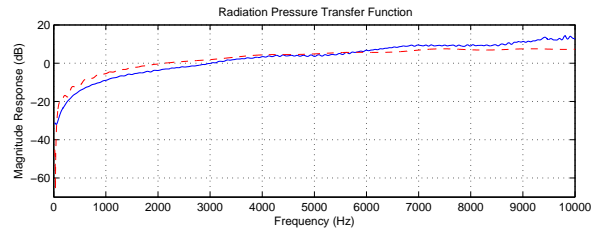
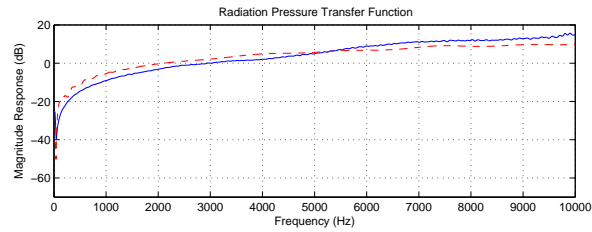
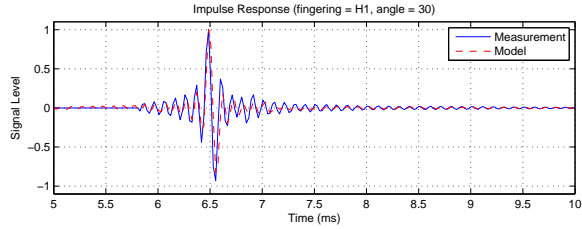
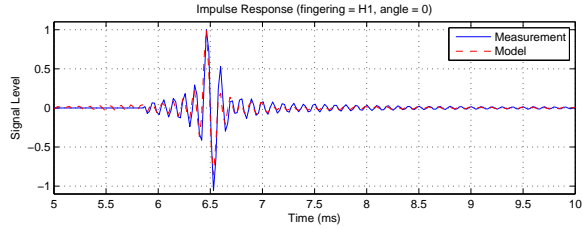
bore of a real woodwind instrument.

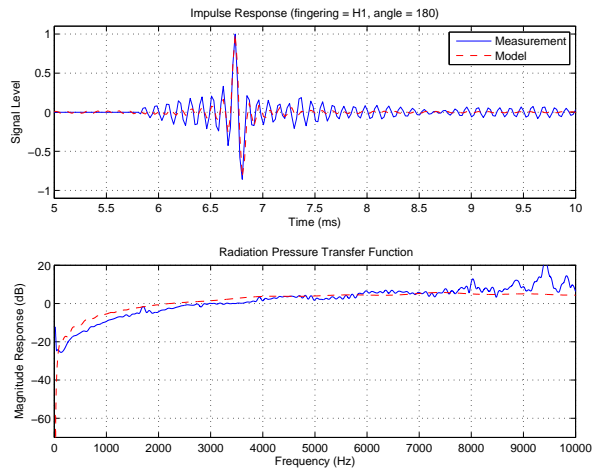
Appendix A

Results of Final Measurements

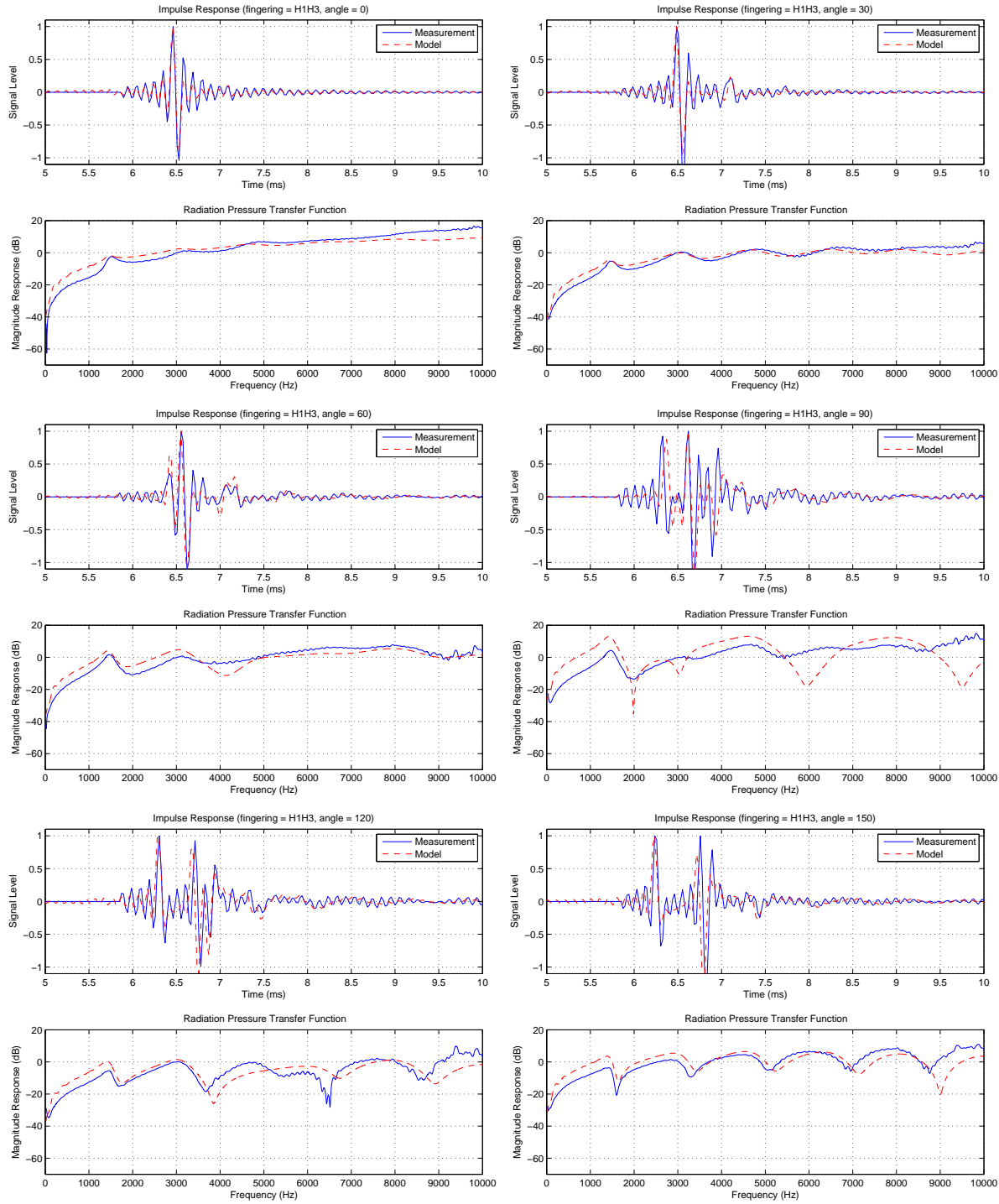
The final results of all fingerings are listed in the following pages. Because of symmetry, fingering H1 was only measured at angles from 0-180 degrees. Other fingerings were measured for full angles (0-330 degrees).

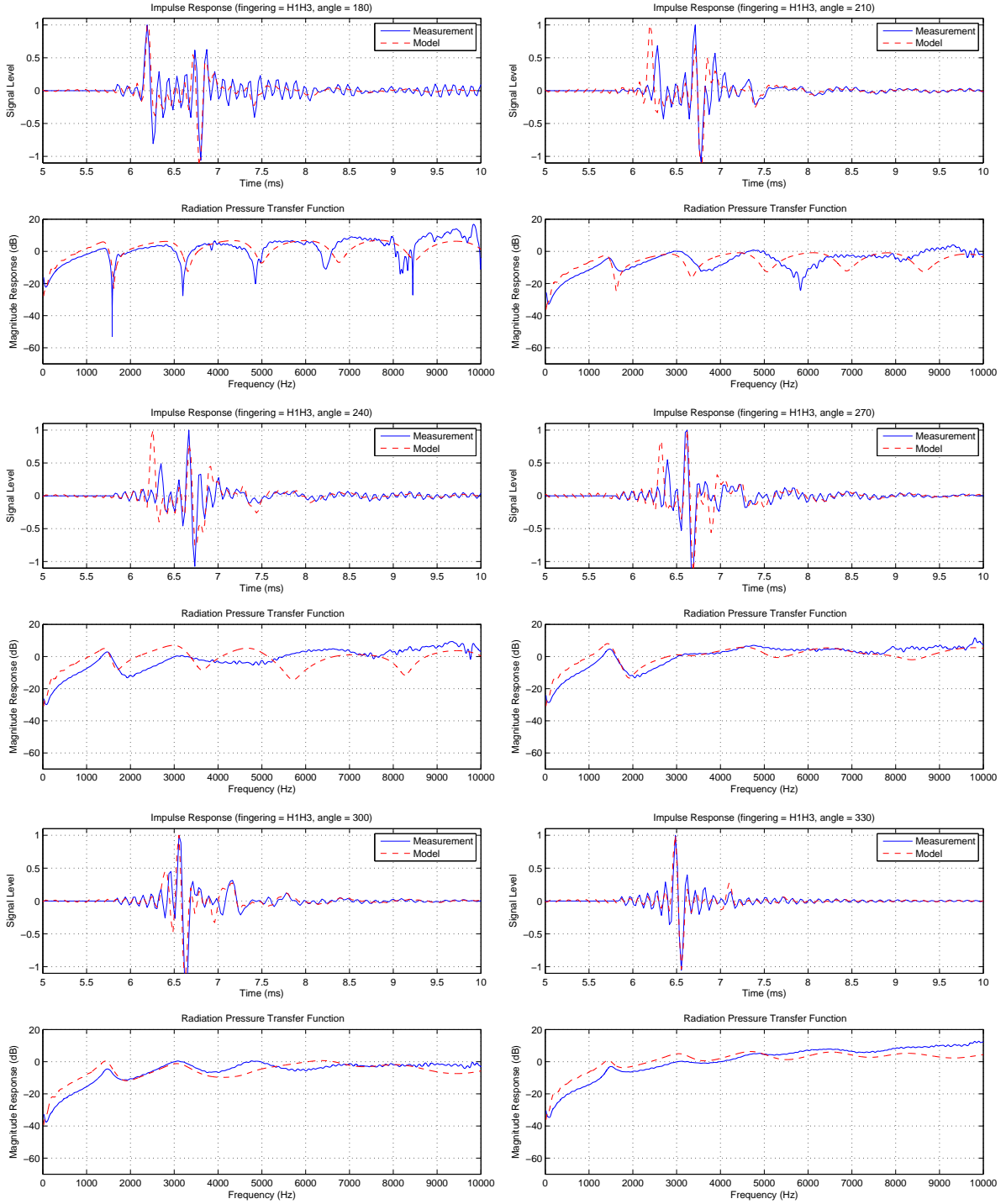
A.1 Fingering H1



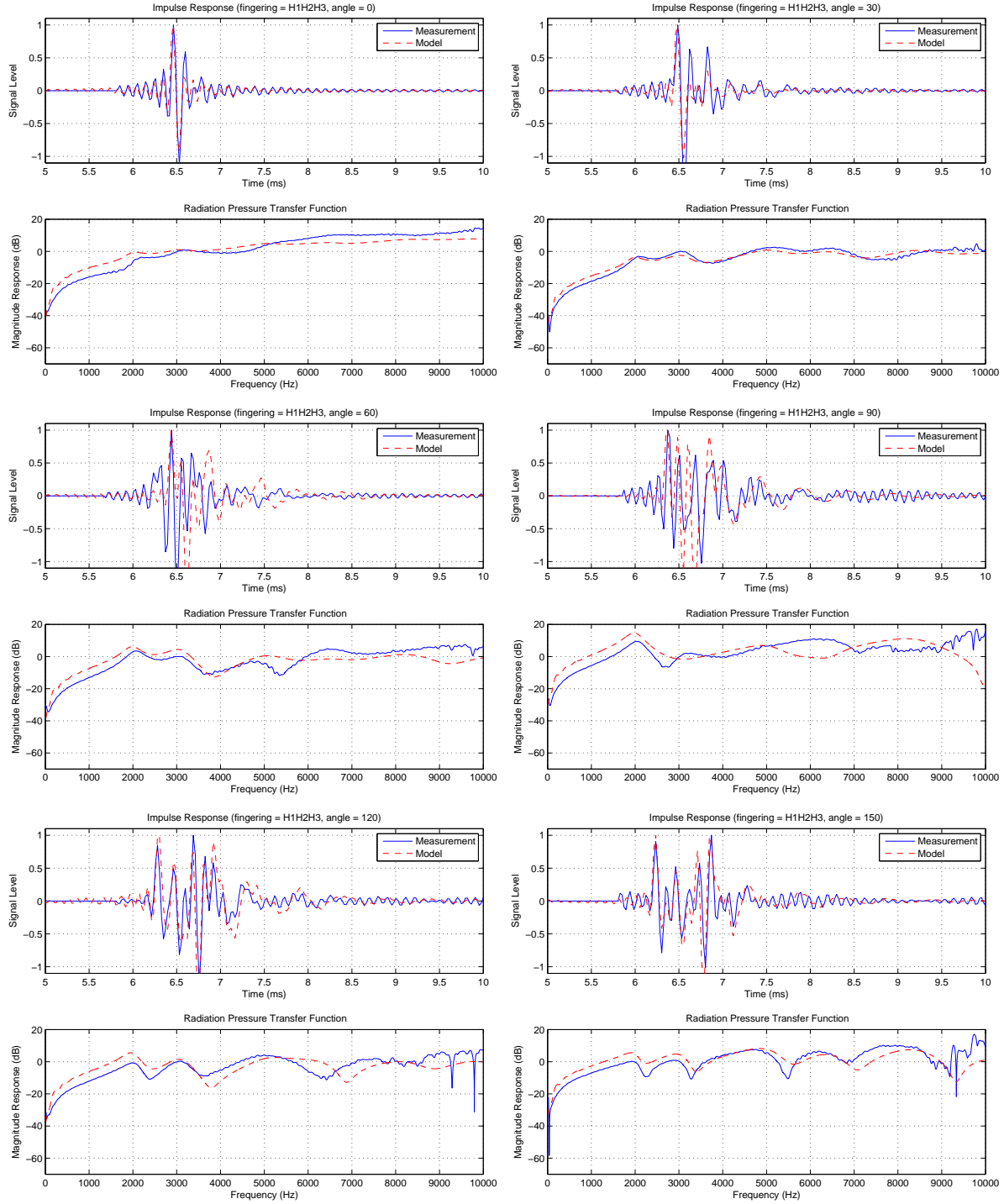


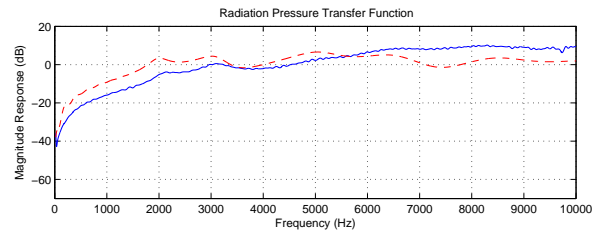
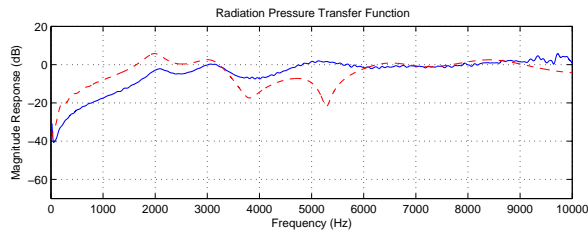
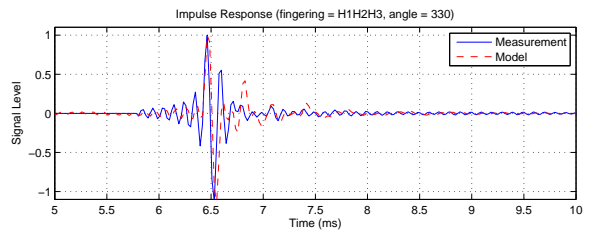
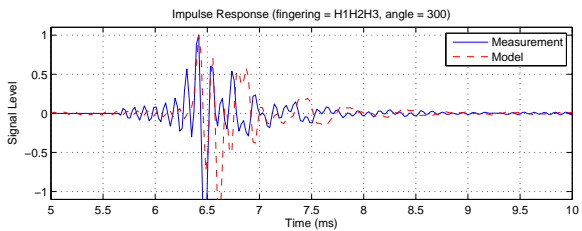
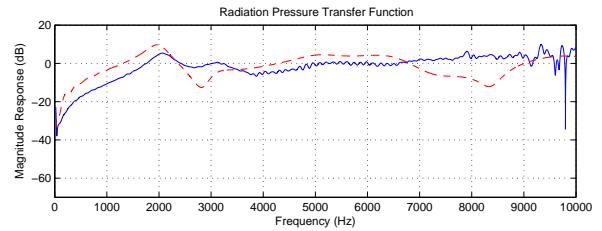
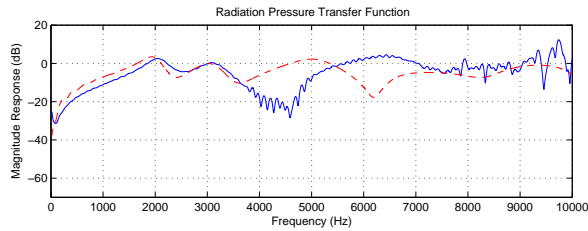
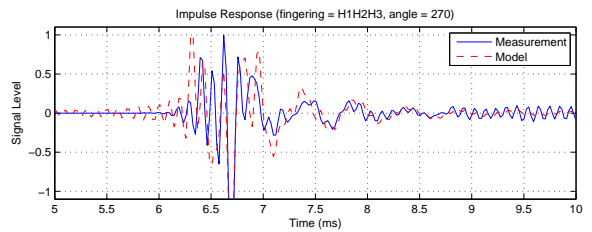
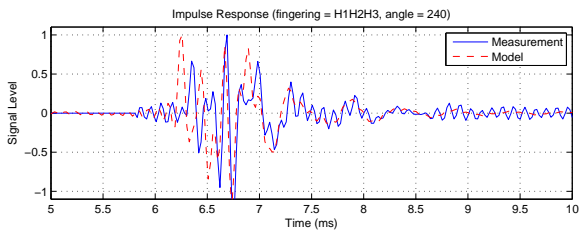
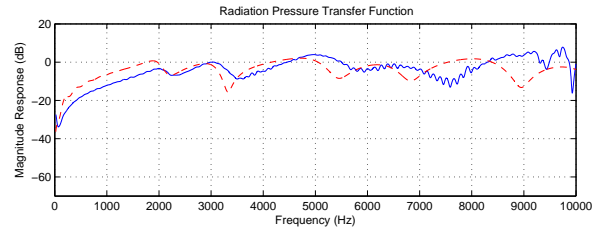
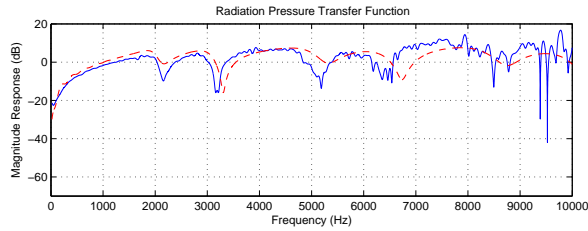
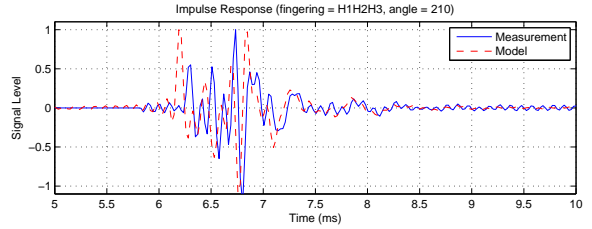
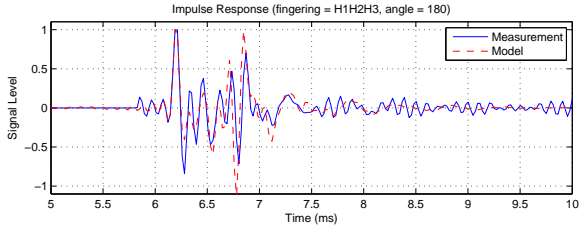
A.2 Fingering H1H3



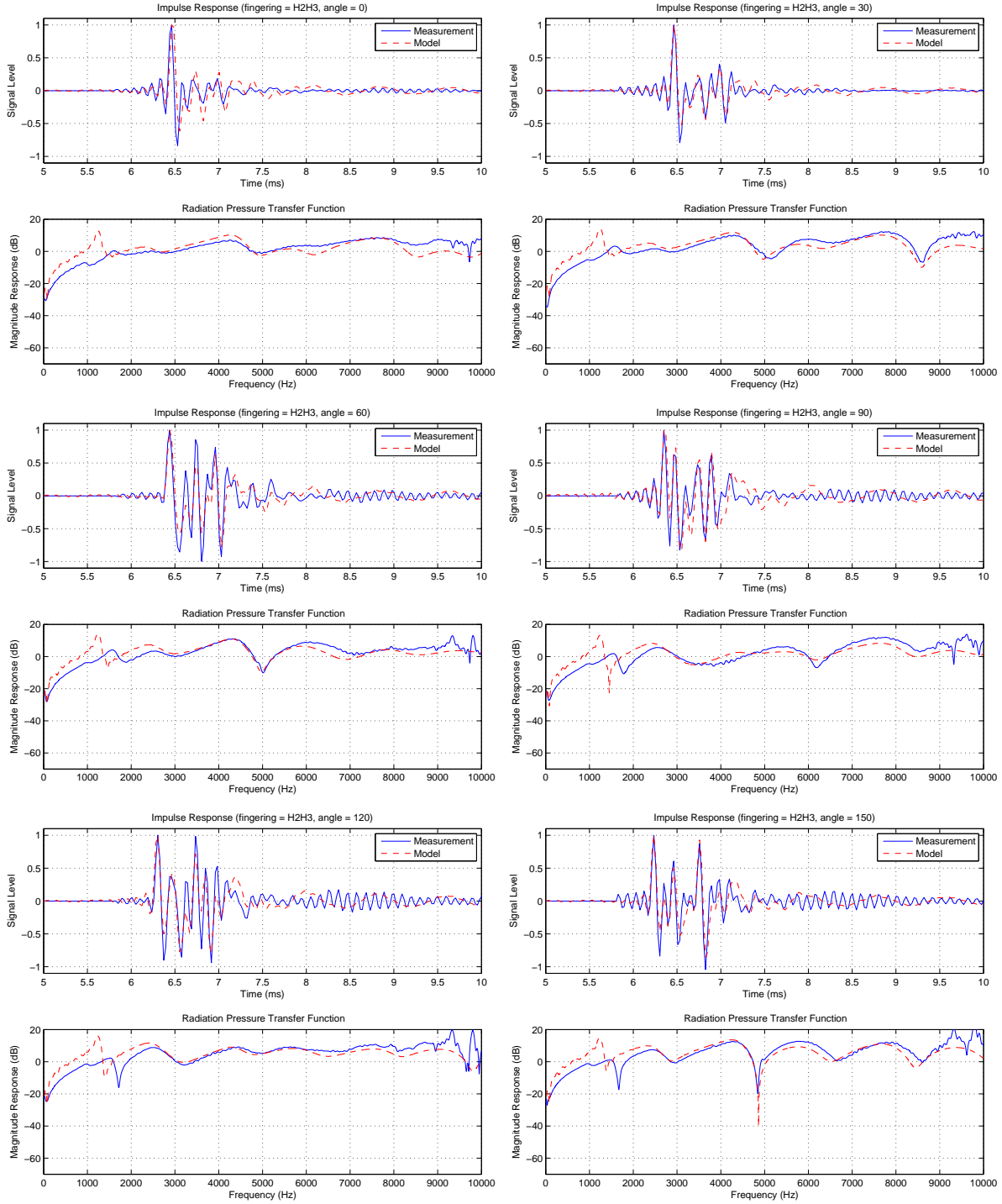


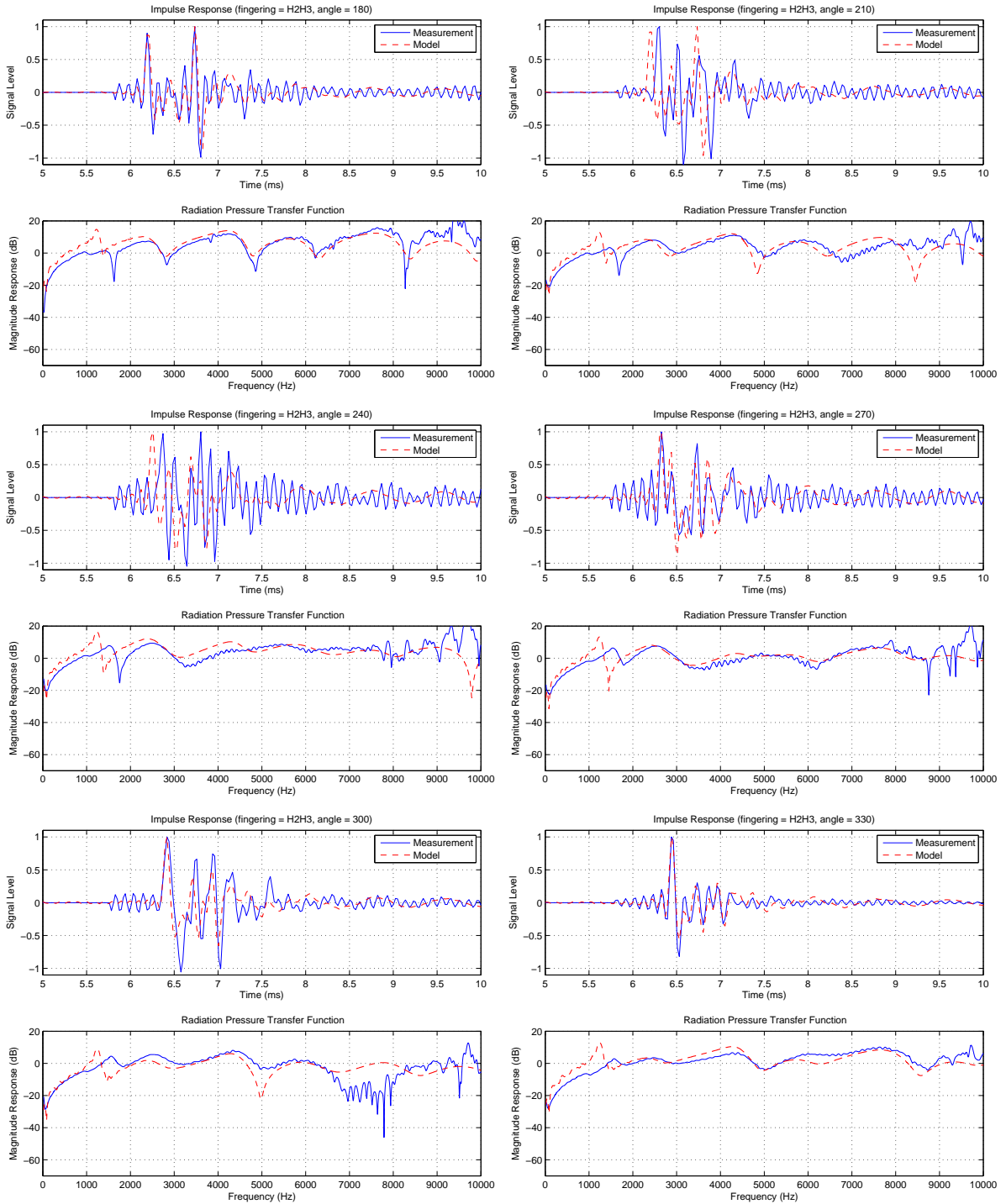
A.3 Fingering H1H2H3



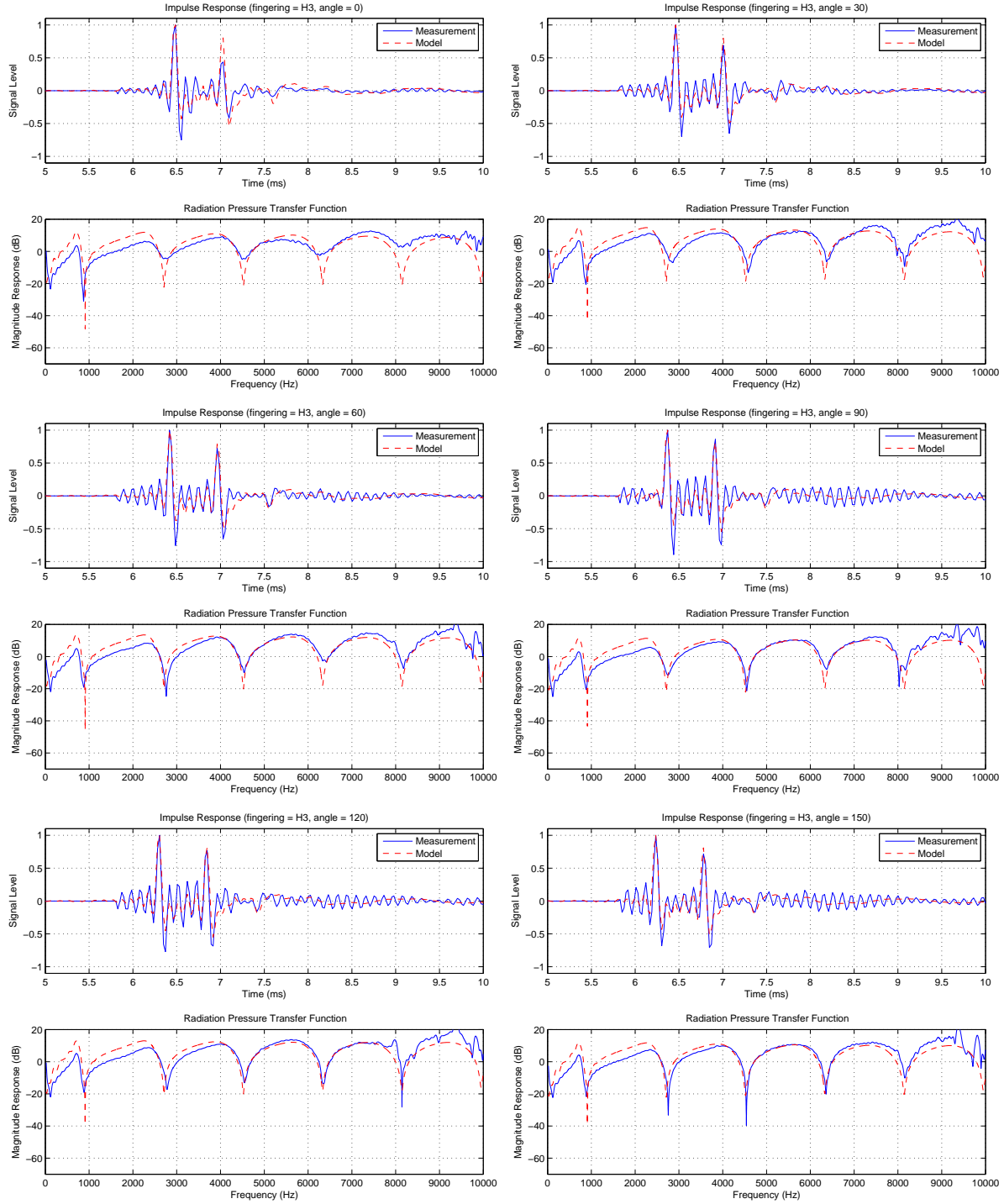


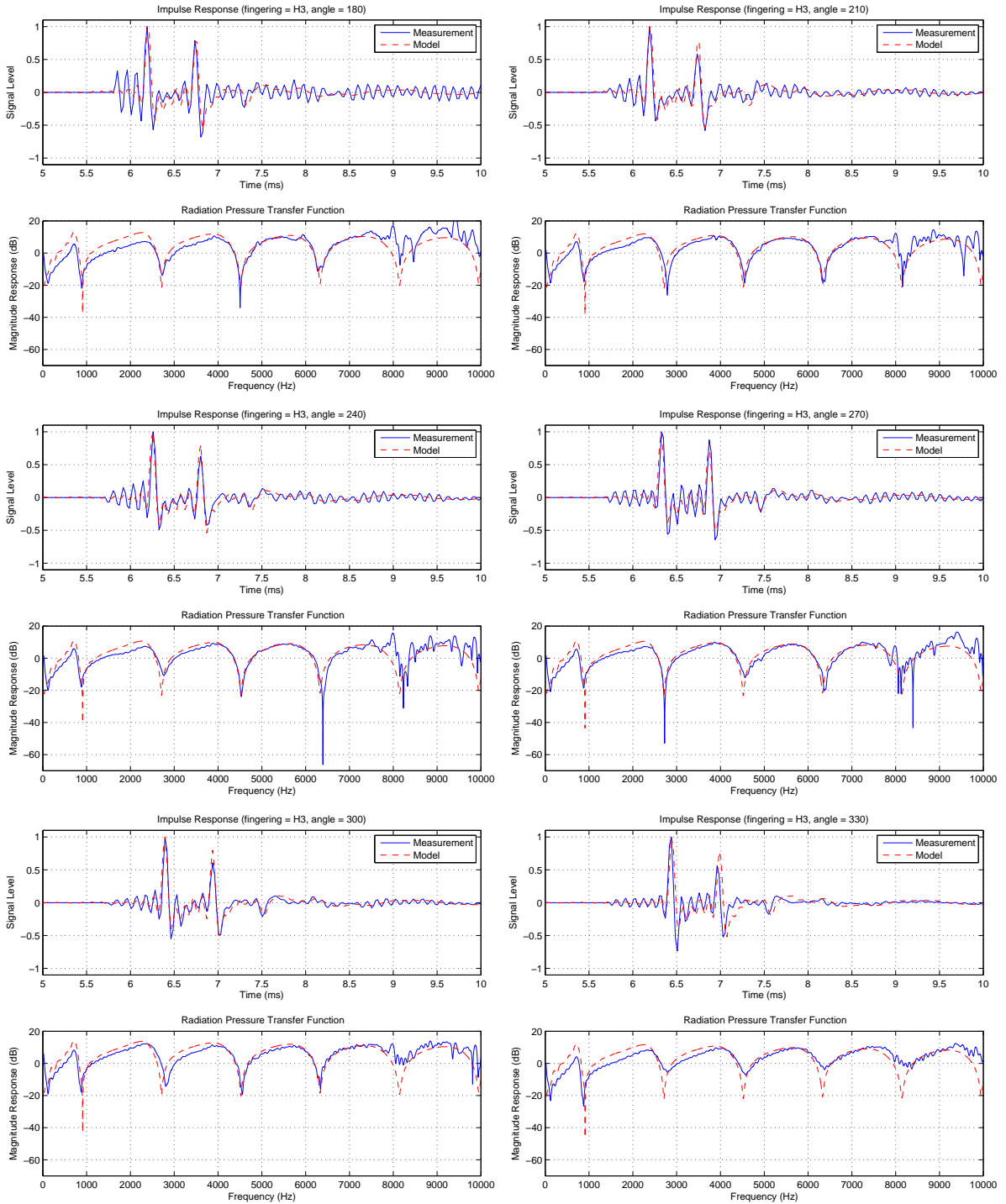
A.4 Fingering H2H3





A.5 Fingering H3





References

- Y. Ando. Experimental study of the pressure directivity and the acoustic centre of the circular pipe horn loud speaker. *Acoustica*, 20, 1968.
- Y. Ando. On the sound radiation from semi-infinite circular pipe of certain wall thickness. *Acoustica*, 22, 1969.
- A. H. Benade and J. H. Smith. Brass wind instrument impulse response measurements. *J. Acoust. Soc. Am*, 70(S22), 1981.
- Alexander Buckiewicz-Smith. Methods for measuring the acoustic response of wind instruments. Master's thesis, McGill University, 2008.
- Jean-Pierre Dalmont. Radiation impedance of tubes with different flanges: Numerical and experimental investigations. *J. Sound Vib.*, 244(3):505–534, 2001.
- Jean-Pierre Dalmont, Cornelis J. Nederveen, Véronique Dubos, Sebastien Ollivier, Vincent Meserette, and Edwin te Sligte. Experimental determination of the equivalent circuit of an open side hole: Linear and nonlinear behaviour. *ACTA Acustica*, 88:567–575, 2002.
- A. M. Deane. *Time domain work on brass instruments*. PhD thesis, University of Surrey, 1986.
- V. Dubos, J. Kergomard, A. Khettabi, J.-P. Dalmont, D. H. Keefe, and C. J. Nederveen. Theory of sound propagation in a duct with a branched tube using modal decomposition. *Acustica*, 85:153–169, 1999.

- Angelo Farina. Simultaneous measurement of impulse response and distortion with a swept-sine technique. *Audio Engineering Society. Presented at the 108th AES Convention, Paris, France., 2000.*
- Neville H. Fletcher and Thomas D. Rossing. *The Physics of Musical Instruments*. Springer-Verlag, 1991.
- Douglas H. Keefe. *Woodwind Tone-hole Acoustics and the Spectrum Transformation Function*. PhD thesis, Case Western Reserve University, 1981.
- Douglas H. Keefe. Acoustical wave propagation in cylindrical ducts: Transmission line parameter approximations for isothermal and nonisothermal boundary conditions. *J. Acoust. Soc. Am.*, 75(1):58–62, 1984.
- Douglas H. Keefe. Woodwind air column models. *J. Acoust. Soc. Am.*, 88(1):35–51, July 1990.
- Jonathan A Kemp. *Theoretical and experimental study of wave propagation in brass musical instruments*. PhD thesis, University of Edinburgh, 2002.
- Yakov Kulik. Transfer matrix of conical waveguides with any geometric parameters for increased precision in computer modeling. *J. Acoust. Soc. Am.*, 122(5), 2007.
- Antoine Lefebvre, Gary P. Scavone, Jonathan Abel, and Alexander Buckiewicz-Smith. A comparison of impedance measurements using one and two microphones. In *Proc. of the International Symposium on Musical Acoustics*, 2007.
- Harold Levine and Julian Schwinger. On the radiation of sound from an unflanged circular pipe. *Physical Review*, 73(4):383–406, February 1948.
- Aijun Li. *Improvements to the acoustic pulse reflectometry technique for measuring duct dimensions*. PhD thesis, The Open University, 2004.
- C. J. Nederveen, J. K. M. Jansen, and R. R. van Hassel. Corrections for woodwind tone-hole calculations. *Acustica*, 84:957–966, 1998.
- A. N. Norris and I. C. Sheng. Acoustic radiation from a circular pipe with an infinite flange. *J. Sound Vib.*, 135(1):85–93, 1989.

-
- H. F. Olson. *Acoustical Engineering*. Princeton, New Jersey: D. Van Nostrand Company, Inc., 1957.
- Lord Rayleigh and John William Strutt. *The Theory of Sound*. London: The Macmillan Company, 2nd edn. Reprinted 1945, New York: Dover Publications, 1896.
- Antoine Rousseau. Modélisation du rayonnement des instruments à vent à trous latéraux. Technical report, Compte rendu de l'étude menée à l'I.R.C.A.M., 1996.
- Gary Paul Scavone. *An acoustic analysis of single-reed woodwind instruments with an emphasis on design and performance issues and digital waveguide modeling techniques*. PhD thesis, Stanford University, 1997.
- Gary Paul Scavone and Matti Karjalainen. Tonehole radiation directivity: A comparison of theory to measurements. In *Proc. of the International Computer Music Conference*, Göteborg, Sweden, 2002.
- David Brian Sharp. *Acoustic pulse reflectometry for the measurement of musical wind instruments*. PhD thesis, University of Edinburgh, 1996.
- JA Ware and K. Aki. Continuous and discrete inverse scattering problems in a stratified elastic medium. I: planes at normal incidence. *J. Acoust. Soc. Am*, 45(4):911–921, 1969.